Chapter 5

Observations

5.1 Selection of observed fields

We have chosen ten fields observed with ASCA, as shown in table 5.1, for the CXB analyses in this thesis. Among them, Draco, NEP, and QSF3 are the PV-phase (Performance Verification phase) observations in the CXB category (ref. §3.1.4). There are two more observations in the CXB category, i.e. "Lynx Field" and "Lockman Hole". However, these observations were carried out when the GIS SP-discrimination was disabled (ref. §3.4.3), so that the RNXB counting rate is significantly higher. Therefore, we decided

Table 5.1: Summary of the observed fields to be employed in this thesis.

Name	Position*		Pts.⋆	Exp.†	Area‡	$N_{\rm H}^{\sharp}$	PI◇
Large Sky Survey (LSS)	198.6	31.5	76	515,392	7.22	1.1	Tsuru
SA57	197.2	29.4	6	461,343	0.68	1.0	Kii
Draco Field	257.0	71.0	3	57,002	0.71	4.1	PV
NEP	269.8	66.6	8	118,434	0.58	4.2	PV
QSF3	55.4	−44.1	4	60,157	0.43	1.7	PV
z-system (ZSYS)	40.0	−23.0	5	109,893	1.68	2.3	Yamasaki
Braccesi Field (BF)	195.3	35.6	4	114,738	1.47	1.2	Ishisaki
Jupiter	184.9	−0.6	1	20,389	0.40	2.1	PV
Arp 220	233.6	23.5	1	23,039	0.40	4.2	PV
3C368	271.2	10.9	1	19,934	0.40	9.8	PV

* Approximate field center (RA,DEC) in J2000.

⋆ Number of pointings.

† Total exposure time (s) after data screening.

‡ Covered area ($\deg^2$) on the sky.

♯ Galactic line of sight column density (10^{20} $\rm cm^{-2}$) from Einstein On-line Service (*EINLINE*).

◇ Principal Investigator. PV means observations in the PV-phase.

not to include them in our analyses. Large Sky Survey (LSS) and Deep Survey in SA57 are the team projects of ASCA, proposed by T. Tsuru (Kyoto Univ) and T. Kii (ISAS), respectively, with many co-PIs in various institutes in Japan. Survey areas of LSS and SA57 are partially overlapped. "z-system" (ZSYS) and "Braccesi Field" (BF) are the observations in GO-phase (Guest Observation phase) in the CXB category, proposed by N. Yamasaki (Tokyo Metro Univ) and Y. Ishisaki (Tokyo Univ), respectively. Jupiter, Arp 220, and 3C368 are the target observations in the PV-phase, but the targets turned out to be so faint that the data can be utilized for the present purpose. Positions of these fields are plotted in figure 5.1 in the Galactic coordinates.

Most of these observations (except Jupiter, Arp 220, and 3C368) have multiple pointings with different Euler angles, and are covering larger sky area than that available with a single ASCA pointing. We show the observation log and contour-map images of these fields in appendix A and B, respectively. The way these images have been synthesized is explained in §5.3. In §5.2, we briefly describe each field.

5.2 Description of Individual Fields

5.2.1 LSS

In the LSS project, we have systematicaly surveyed a continuous $\sim 1^\circ \times 5^\circ$ region at high Galactic-lattitides with ASCA, located around $(l, b) = (75.4^\circ, 83.4^\circ)$. The observa-

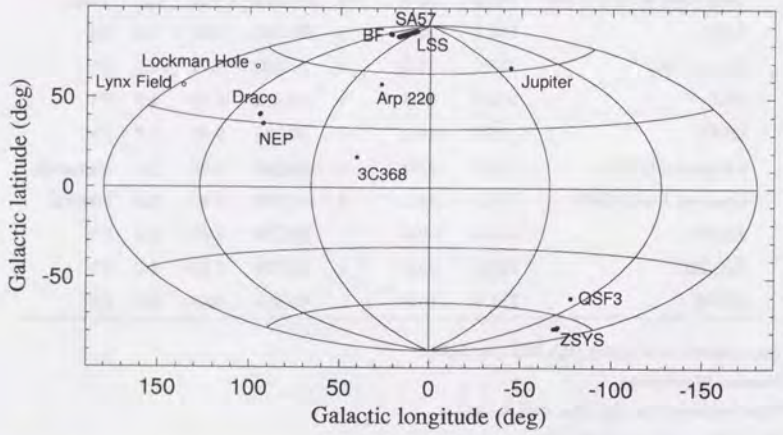

Figure 5.1: Galactic positions of the observed fields in table 5.1. "Lynx Field" and "Lockman Hole" are also included.

tion is splitted into many different epochs, and the total area observed so far in GO-1, GO-2 and GO-3 phases amounts to > 5 deg^2. Optical follow-up observations is undergoing to indentify the X-ray detected sources, using the mosaic CCDs in Kiso observatory and other instruments. The LSS survey field is partially overlapped with SA57 (left edge of figure B.1). The already covered area, more than 5 deg^2, is larger than any other surveys conducted with ASCA so far. This is the great advantage to study the average properties of the CXB. Furthermore, Ueda (1996) has searched point sources in the LSS field, and a list of point sources down to a 2–10 keV flux limit of several times 10^{-14} erg s^{-1} cm^{-2}, detected with the ASCA GIS and SIS, is available.

In LSS, 76 pointings have been made so far, which consist of 16 pointings in GO-1, 20 pointings in GO-2, and 40 pointings in GO-3. The sky mapping has been arranged so that the SIS f.o.v. ($22' \times 22'$) is aligned in mosaic. Each point has been observed twice with SIS with two different attitude, by shifting f.o.v. by its half size. Although mean exposure for each pointing is about 10 ks, which is shorter than typical exposure (~ 40 ks) for one target obtained with ASCA, at least 20 ks of exposure per sensor is guaranteed for each sky position by this multiple pointings. Because the GIS f.o.v. is about two times larger than that of the SIS, the total exposure achieved with the GIS multi pointings becomes much longer on the average.

In figure 5.2, we show the 76 pointing positions in LSS. For convinience, we split these pointings into four groups as shown in the figure, and call them a-LSS, b-LSS, c-LSS, and d-LSS, respectively. As shown in figure B.1, tens of sources are seen over the entire LSS fields. Among them, the brightest one, at $(\alpha_{2000}, \delta_{2000}) = (13^h20^m15^s, +33^\circ08'36'')$, is identified with the galaxy NGC 5098, which appears extended in the ROSAT image (Y.Tanaka, private communication).

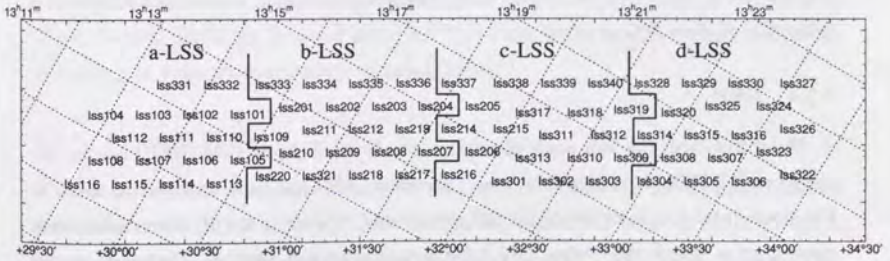

Figure 5.2: LSS pointing positions

5.2.2 SA57

Selected Areas are optically selected survey fields, and among them, Selected Area 57 (SA57) is one of the most deeply surveyed fields (Koo 1986; Koo and Kron 1988; Majewski et al. 1994). The limiting magnitude is $B \sim 24$, which is one of the deepest in the whole sky. In radio waveband, Windhorst el al. (1984) surveyed this field with Westorbork Synthesis Radio Telescope down to a flux limit of 0.6 mJy at 1.4 GHz.

SA57 is located near the north Galactic pole, thus has a low Galactic column and is suitable for X-ray surveys. However, there were no X-ray studies on this field prior to ASCA. ASCA has observed SA57 in GO-1 and GO-3. In GO-1, the scheduled 400 ks observation time was splitted into five pointings, intending to cancel the non-uniform sensitivity due to the XRT vignetting and the SIS gaps. In GO-3, all of the scheduled 400 ks observation time was devoted to a single pointing to extend the flux limit. SA57 has thus become the deepest field observed with ASCA. Ogasaka (1996) has searched faint sources in SA57 using the ASCA SIS.

There is a distant cluster of galaxies IIZw 1305.4+2941 in the central region of SA57 (the brightest source in figure B.2). The flux measured by Einstin is 3×10^{-13} erg s^{-1} cm^{-2} and not so bright for ASCA.

5.2.3 Draco Field

There is an unusual interstellar cloud in Draco (Draco cloud; Goerigk et al. 1983). The Draco cloud is located at $(l, b) \simeq (90°, +39°)$. It has a distinctive narrow 21 cm line centered at a local standard rest velocity of ~ -21 km s^{-1} with a width of ~ 2 km s^{-1}, which enables us to separate the forground and background emission. The distance of this cloud is uncertain by at least a factor of two, but a lower limit of 300 pc is presented. Burrows and Mendenhall (1991) observed Draco cloud with ROSAT PSPC, and found a shadowing of soft X-rays below 0.3 keV.

ASCA observed the Draco Field in PV-phase with three pointings. We can see several IPC sources in the GIS f.o.v. (figure B.3). The brightest ASCA source may in fact be a composite of three IPC sources.

5.2.4 NEP

Being free from the Sun angle constraint, the North Ecliptic Pole (NEP) can be observed with ASCA all through the year. Therefore, NEP has been observed 10 times in PV-phase, intending to calibrate the SIS background. Two from the 10 observations were carried out in March 1993, when GIS *SP*-discrimination was disabled. Therefore, we did not include these two observations in our analyses. There are two outstanding sources

in the GIS f.o.v. One is IPC source and the other is the Seyfert 2 galaxy NGC 6552 at a redshift of $z = 0.026$ (Fukazawa et al. 1994). NGC 6552 has a heavily absorbed ($N_{\rm H} \sim 6 \times 10^{23}$ cm^{-2}) hard continuum with prominent iron K line of neutral species of an equivalent width ~ 0.9 keV. Its 2–10 keV flux is $\sim 6 \times 10^{-13}$ erg s^{-1} cm^{-2}.

There are also deep ROSAT observations in the NEP region (Hasinger et al. 1991; Shanks et al. 1991), and a structure in the background with a $\sim 20'$ scale (NEP blotch) were reported.

5.2.5 QSF3

The QSF3 field is located in the Southern Sky at $(l, b) = (250.86°, -51.99°)$, and the Galactic absorption is low ($N_{\rm H} = 1.66 \times 10^{20}$ cm^{-2}; Heiles and Cleary 1979) because of a high Galactic latitude. QSF3 was observed to search for UV excess quasars, and later, ROSAT observations (Shanks et al 1991) resolved $\sim 30\%$ of the CXB into point sources at the flux limit of 10^{-14} erg s^{-1} cm^{-2}.

ASCA has observed the QSF3 field four times in PV-phase centered on almost the same position. There are two point sources clearly detected in the GIS f.o.v. The brighter one is a star with rather soft spectrum, and the other is a QSO at $z = 0.38$ (Chen et al. 1995).

5.2.6 z-system

There is a distant QSO ($z = 2.23$), PKS 0237−233, at the center of this field. PKS 0237−233 is known to have as many as 30 absorption lines of C IV at $z = 1.3$–2.2 (Hewitt and Burbidge 1989), and the existence of "Absorption Supercluster" in size of ~ 20 Mpc are suggested (Heisler 1989). Thus, detailed survey in the optical bands are carried out in this field, and it turned out that 32 QSOs of $z = 0.17$–2.63 are concentrating in the $2° \times 2°$ regions around PKS 0237−233. The Einsein IPC also observed this field with tree pointings of 12 ks in total, and detected four QSOs.

ASCA observed this field with two pointings in GO-2 and another three pointings in GO-3. Several QSOs are detected and PKS 0237−233 is the brightest (Yamasaki et al. in meeting of Astronomical Society of Japan 1995).

5.2.7 Braccesi Field

Braccesi Field is a region around $(l, b) = (108°, 81°)$, and the line-of-sight Galactic absorption is low ($N_{\rm H} \sim 1.2 \times 10^{20}$ cm^{-2}). This sky region has been surveyed for QSOs in the optical (Cristiani et al. 1984), radio (Fanti et al. 1977), and X-ray (Einstein IPC and HRI; Marshall et al. 1984) wavebands, and a complete catalogue of $B < 19.9$ QSOs

of $z = 0.2$–2.2 is available. There is also a concentration of 35 QSOs in 1.7 deg^2 area. Einstein made deep observations in this field (3 pointings with a total exposure of 114 ks with the IPC, and 7 pointings total 129 ks with the HRI), and found 34 IPC sources, which is about twice as much as expected from $\log N$–$\log S$ relation derived from the Einstein Extended Deep Survey.

ASCA observed this field with two pointings in GO-3 and another two pointings in GO-4. There are several point sources clearly detected in the GIS f.o.v. If we exclude sources seen at the detector rim, the brightest is the IPC 2961 at $(13^h04^m, 35°35')$, which is thought to be a QSO at $z = 0.327$. Its 2–10 keV flux is about 8×10^{-13} erg s^{-1} cm^{-2}.

5.2.8 Jupiter, Arp 220, and 3C368

These are the target observations in the PV-phase. However, the main targets turned out to be very faint, and we adopted them for the CXB analyses. Searching such observations are carried out as a part of the ASCA Medium Sensitivity Survey (MSS). ASCA MSS is a team project proposed by T. Takahashi (ISAS), which utilize the large GIS f.o.v. after removing the main targets. We have selected about 30 observations with exposure time > 30 ks at high latitude ($|b| > 10°$) in PV-phase. We particularly uses these three fields in this thesis, because of the particular faintness of the target sources in these fields.

The target positions are $(\alpha_{2000}, \delta_{2000}) = (12^h19^m53^s, -00°37'12'')$, $(15^h34^m57^s, +23°30'11'')$, and $(18^h05^m06^s, +11°01'30'')$, respectively. Arp 220 was faint but detected with ASCA ($kT = 0.4$ keV, $F_X = 4 \times 10^{-13}$ erg s^{-1} cm^{-2}; Kii et al. in "IRAS galaxies observed with ASCA"). Detections of Jupiter and 3C368 are marginal. The observation of Jupiter was conducted in June 1993, about 1 year before the collision with the SL9 commet.

5.3 Data processing

5.3.1 Basic event selection

In order to ensure the RNXB reproducibility, we have employed almost the same event selection criteria for the CXB observations as that of the night-earth observations (§4.4). In practice, we have set the following conditions:

- target elevation from the rim of the Earth $\geq 5°$
- target elevation from the rim of the sunlit Earth $\geq 25°$
- flare-cut conditions (table 4.6)
- attitude jittering $\leq 1'$ for the pointing center, and $\leq 1°$ for the roll angle.

Exposure times shown in table 5.1 are subjected to these screenings. Other data processings such as position linearlization, gain correction, and strict RT-mask are carried

out in a standard way on the ASCA_ANL. ASCA_ANL is the framework of the analysis software mainly utilized for the event by event processing of the ASCA data. It has been developed by the ASCA_ANL working group, which consists of M. Hirayama, H. Kubo, and Y. Ishisaki, as main members.

In creating images, we masked caribration sources and the detector rim with the standard masking images for GIS2 and GIS3 (figure 4.20). We usually utilized the events whose PI channels are within the 0.7–7.0 keV energy band, to avoid high RNXB rate in energy bands below and above the thresholds. Conversion of the detector coordinates into the sky coordinates (see next subsection) is conducted using the mean satellite attitude of each pointing. As described in §3.1.2, the accuracy of the attitude determination is $\sim 1'$, and the attitude is subjected to jittering to a similar level.

When discussing the CXB spectra, we use the events within 20 mm from the optical axis of each detector. The covered sky areas shown in table 5.1 refers to this detector region. In spectrum fitting, we usually restrict the PI channels to be fitted in the 0.6–10 keV energy band.

5.3.2 Handling of multiple pointings

As mentioned in §5.1, most of the sample fields are observed with multiple pointings, which makes the analyses quite complicated.

In creating the CXB spectra, we simply accumulated the events inside 20 mm from the optical axis, as described in the previous subsection. Therefore, the spectra are in fact biased to the regions where exposure is deep owing to the overlap of the multiple pointings. However, even a single pointing observation is biased to the central region considering the vignetting effect, and we did not make a correction for exposure to compensate the bias while creating the CXB spectra.

In the image analyses, it is desirable to construct a mosaic image by superposing multiple pointing images into a single large one, in order to reduce statistical errors. This procedure is usually carried out by converting the detector coordinates $(DETX, DETY)$ into the sky coordinates $(SKYX, SKYY)$, utilizing the knowledge of the satellite Euler angles. On the sky coordinate image, the coordinates are rectangular and each pixel corresponds to a particular sky position, which is calculated from the Euler angles and a fixed reference-sky-position (= SKYREF). As far as the SKYREF are the same, we can sum up the sky coordinate images of multiple observations which were carried out with different Euler angles. We define the operator $det2sky\left[B\right]$ which convert the detector coordinate image $B(DETX, DETY)$ into the sky coordinate image $M(SKYX, SKYY)$. Using this

operator, we can create the mosaic image $M^{OBS}(SKYX, SKYY)$ by calculating

$$M^{OBS}(SKYX, SKYY) = \sum_{GIS2,3} \sum_{j} det2sky\Big[B^{OBS}_{j,n}(DETX, DETY)\Big], \tag{5.1}$$

where j represents the pointing number in the observed field, and $B^{OBS}_{j,n}$ is the detector coordinate image taken by GISn ($n = 2$ or 3) in the j-th pointing. Each pixel of M^{OBS} contains the number of detected events, accumulated over the entire pointings.

Exposure of each pixel is calculated by:

$$M^{EXP}(SKYX, SKYY) = \sum_{GIS2,3} \sum_{j} T_j \; det2sky\Big[B^{MASK}_{n}(DETX, DETY)\Big], \tag{5.2}$$

where T_j is the exposure time of the j-th pointing, and $B^{MASK}_{n}(DETX, DETY)$ is the standard image masking for GISn (figure 4.20). By dividing M^{OBS} by M^{EXP}, we can obtain a sky coordinate image in which each pixel value corresponds to event counting rate. In figure 5.3a and 5.3b, we show M^{EXP} and M^{OBS} for the observations in the Braccesi Field.

5.3.3 Image smoothing

Since M^{OBS} is straightforward but not intuitive, we usually smooth the image with the position-dependent XRT+GIS point spread function $P^{PS}(\theta, \phi; DETX, DETY)$, and then correct each pixel for the exposure time. This $P^{PS}(\theta, \phi; DETX, DETY)$ represents the brightness profile on $DETX$-$DETY$ plane when a point source is located at offset angle θ and azimuth angle ϕ from the XRT optical axis. It is normalized so that the peak value is constant for any set of (θ, ϕ). Introducing the normalization factor $A^{PS}(\theta, \phi)$, $P^{PS}(\theta, \phi; DETX, DETY)$ is expressed by the response functions of the XRT and GIS in a formula:

$$\begin{aligned} A^{PS}(\theta,\phi)\, P^{PS}(\theta,\phi;DETX,DETY) &= \int dPI\; D(DETX, DETY, PI) \\ &= \int dPI \int dE\; R_{GIS}(E, PI) \int dx\, dy \\ &\times\; P_{GIS}(E, x, y; DETX, DETY)\; A_{GIS}(E, x, y) \\ &\times\; P_{XRT}(\theta, \phi, E; x, y)\; A_{XRT}(\theta, \phi, E) \\ &\times\; A_{T.S.}(E)\; S(E), \end{aligned} \tag{5.3}$$

where $S(E)$ stands for the energy spectrum of the point source, and other symbols are the same as in §4.2.1. The factor $A^{PS}(\theta, \phi)$ effectively takes charge of vignetting. We have calculated $P^{PS}(\theta, \phi; DETX, DETY)$ by interpolating the Cyg X-1 images, which were observed with various offset angles and azimuth angles within $\theta \leq 17'$. As seen in equation (5.3), both $A^{PS}(\theta, \phi)$ and $P^{PS}(\theta, \phi; DETX, DETY)$ depend on the source spectrum $S(E)$. However, it mainly affects only the normalization of $A^{PS}(\theta, \phi)$, and

changes of the function profiles are almost negligible in the range of $\Gamma \sim 1.4$–2.2 in terms of photon index. Therefore, we assumed $\Gamma = 1.7$ in calculating $A^{PS}(\theta, \phi)$ and $P^{PS}(\theta, \phi; DETX, DETY)$.

Here, we define the operator $ccf\Big[B\Big]$ which conduct the image smoothing as:

$$\begin{aligned} M(SKYX, SKYY) &= ccf\Big[B(DETX, DETY)\Big] \\ &\equiv det2sky\Big[\int dDETX\, dDETY\; P^{PS}(\theta, \phi; DETX, DETY)\; B(DETX, DETY)\Big], \end{aligned} \tag{5.4}$$

i.e. cross correlation of $B(DETX, DETY)$ with $P^{PS}(\theta, \phi; DETX, DETY)$. At the same time, this operator converts the image into the sky coordinates. Using this operator, we can create the smoothed and exposure-corrected mosaic image $M^{CCF}(SKYX, SKYY)$ by calculating

$$M^{CCF}(SKYX, SKYY) = \frac{\displaystyle\sum_{GIS2,3} \sum_{j} ccf\Big[B^{OBS}_{j,n}(DETX, DETY)\Big]}{\displaystyle\sum_{GIS2,3} \sum_{j} T_j\; ccf\Big[B^{MASK}_{n}(DETX, DETY)\Big]}. \tag{5.5}$$

In figure 5.3c, we show a contour-map image of M^{CCF} for the Braccesi Field. We also show M^{EXP} and M^{CCF} for all the sample fields in appendix B. Note that M^{CCF} has been corrected for exposure overlaps among different pointings, so that it is uniform in terms of counts/s. However it is not corrected for the XRT vignetting; as a result, it is not uniform in terms of counts/s/cm^2, and we can see a slight step-wise structure in figure 5.3c at the rims of the overlapping fields. More delved image processing will be discussed in §7.2.

We have conducted these image processings on DISPLAY45. DISPLAY45 is a command-driven interactive histogram browsing program based on CERN libraries; particularly HBOOK4 as the histogram management and HPLOT5 as the histogram plotting. DISPLAY45 has been developped by A. Shirahashi, A. Takahashi, and R. Itoh. A user can add his/her own external commands written in C or FORTRAN languages without re-compiling the main program, utilizing the method of dynamic linking. A number of useful commands and analysis tools for the ASCA data have been collected and compiled by Y. Ishisaki, and he released them as dis45userlib. The operators such as $det2sky\Big[B\Big]$ and $ccf\Big[B\Big]$ are realized as the external commands on DISPLAY45.

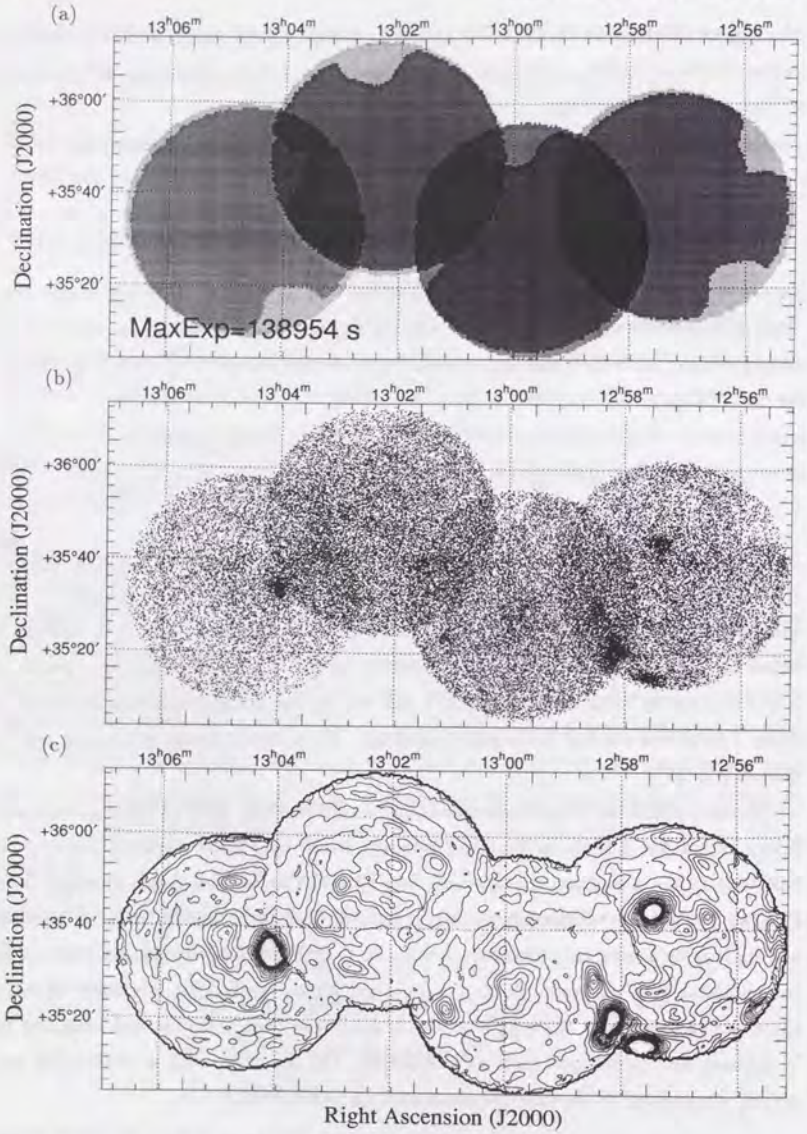

Figure 5.3: Images of (a) M^{EXP}, (b) M^{OBS}, and (c) M^{CCF} for the four pointing observations in the Braccesi Field. Coordinates superposed on the images are J2000. (a) Gray scale image of M^{EXP}. White and black pixels correspond to 0 s and 138,954 s exposure, respectively. (b) Dot-map image of M^{OBS} in the 0.7–7.0 keV energy band. (c) Contour-map image of M^{CCF} in the 0.7–7.0 keV energy band. Contour levels are (5, 10, ..., 95, 100) $\times 10^{-6}$ c s^{-1} pixel^{-1}.

Chapter 6

Average CXB spectrum in the LSS field

6.1 CXB data sampling and data analysis method

In order to study the average properties of the CXB, it is preferable to sum up data from as many different sky regions as possible, so as not to be affected by particular point sources which happen to be in the f.o.v. Even though total exposure time were long, observations which are biased in a particular small region would have a risk of contaminations with point sources and local structures. Therefore, we have chosen to utilize all the LSS observations to construct an average CXB spectrum. The LSS observations cover large sky area of 7.2 deg^2 by 76 pointings with exposure time of 5–10 ks for each (ref. §5.2.1), which matches the above conditions. Moreover, the LSS field is well surveyed by Ueda (1996), and a list of point sources detected with ASCA GIS and SIS is available. Therefore we can easily and reliablly take into account the effects of point sources. However, since the LSS fields are restricted to sky directions around $(l, b) = (75.4°, 83.4°)$, we might not be able to regard the LSS spectrum as the average CXB over the whole sky, if the CXB has a global structure, which will be discussed in the next chapter.

We adopt the data selection criteria described in §5.3, and the total exposure time of the LSS observations amounts to 515.4 ks. We evaluate the RNXB spectra by the H02-sorting method, with the normalization adjusted to correct the long-term RNXB trend, as described in §4.4.4. We include only the statistical errors for the RNXB spectra; we believe the systematic error of the RNXB spectrum for the entire LSS observations to be less than ±2.5% for the following two reasons. Firstly, the total exposure time of the LSS observations is very long. Secondly, the LSS observations are splitted into four periods from December 1993 to July 1995, with about half a year interval so that the long-term RNXB change is also averaged. The effects of the RNXB systematic error will be discussed in in §6.4.1. In the following spectral fitting, we used `gis2v4_0.rmf` and `gis3v4_0.rmf` as RMF, and we created ARF with SimARF described in §4.3.4.

6.2 Ring-sorted CXB spectra

Figure 6.1a shows the ring-sorted CXB spectra, i.e. spectra of the entire LSS data which are accumulated in annular regions in 5 mm step centered on the XRT optical axis on the GIS detector plane. Although the XRT effective area drops as the offset angle gets larger because of vignetting, integration area on the detector plane also gets larger; thus the fluxes of 10–15 mm, 15–20 mm, and 20–25 mm rings are roughly comparable. We can see the trend of spectral softening toward outer rings, which is caused by the following two effects. Firstly, the vignetting effect is stronger for harder X-rays, which makes the spectrum to appear softer toward the detector rim. Secondary, the stray CXB photons, which has a much softer spectrum than the normal CXB photons, become also dominant toward the detector rim. As described in §4.3, stray lights thus supress the offset angle dependence of the effective area, while enhance its energy dependence.

In order to show that these ring-sorted CXB spectra are originally flat on the sky, we compare them with the ring-sorted day-earth spectra which are shown in figure 6.1b. These day-earth spectra were obtained by integrating all the data when the XRT pointed to the sunlit Earth, for two years from June 1993 to June 1995, so that we can regard them to have a very uniform surface brightness. After subtracting RNXB spectra from these day-earth spectra in just the same way as the CXB spectra, flux above 4 keV becomes almost zero. Therefore we compare the day-earth and CXB spectra in the 0.6–4.0 keV energy band. This also means that the evaluation of RNXB spectra has been properly carried out.

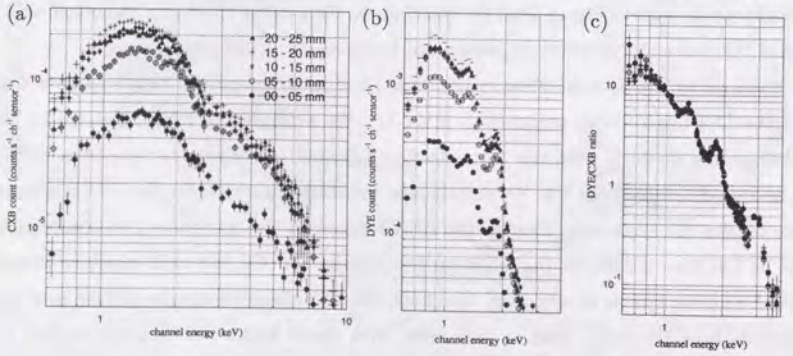

Figure 6.1: Ring-sorted spectra of (a) CXB and (b) day-earth, integrated in the radius of 0–5 mm (•), 5–10 mm (○), 10–15mm (◇), 15–20 mm (+), and 20–25 mm (△), centered on the optical axis on each detector plane. Panel (c) shows ratios of (b) to (a). GIS2 and GIS3 spectra are summed up.

Figure 6.1c shows ratios of the day-earth spectra to the CXB spectra in the same ring. All ratios have the same profiles and the same normalizations within error bars typically of 10% order, independently of the ring radii. Thus we confirm that the CXB data which we used here are uniform on the sky, in both spectral shape and surface brightness, at least below 4 keV. This justifies the assumption we made when we created the CXB ARF in §4.3.4. Furthermore, the day-earth spectra are brighter than the CXB spectra by about one order of magnitude at 1 keV, so that the day-earth spectra is much less affected by RNXB. The results shown in figure 6.1c also demonstrate the accuracy of the RNXB evaluation.

To quantify the CXB spectrum, it is of critical importance to verify that the CXB ARF (ref. §4.3.4) has been generated correctly. For this purpose, it is the most straightforward to examin whether all the ring-sorted CXB spectra can be reproduced by a single, common spectral model without introducing ring-to-ring adjustment of the model shape. For

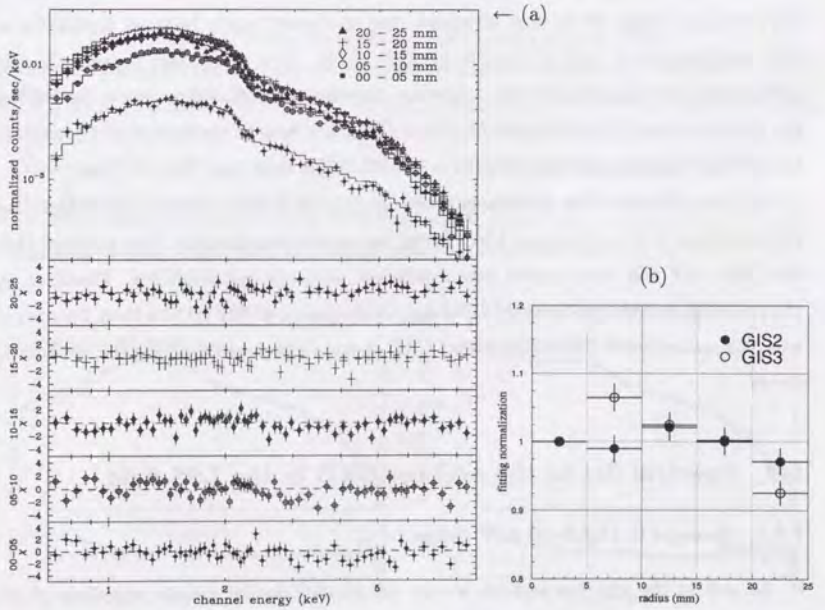

Figure 6.2: (a) The ring-sorted CXB spectra of figure 6.1a, fitted with a power-law plus *RS* model of one solar abundances. Top panel shows each spectrum (markers) and the best fit model (solid lines). Lower five panels show residuals from each spectrum. All the fit parameters except normalization are common to all the spectra. (b) The model normalization for each spectrum plotted versus radius of the rings. Normalization of the inmost ring is defined to be 1.0.

the fitting model, we employ the power-law + Raymond-Smith (here after *RS*) model, which is often chosen to fit a CXB spectrum; in the next section, we will check whether this model is appropreate for our CXB spectrum. The number of free parameters are eight in total: power-law photon index Γ, power-law normalization, *RS* temperature kT, *RS* normalization, and relative normalizations for the five ring-sorted spectra with normalization for the innermost region fixed to 1.0. That is, the model spectrum has an identical shape for all the rings, but allowed to have different normalizations for different rings. Element abundances for the *RS* model are fixed to one solar. To examine the consistency between the two detectors, for the moment we analyze the GIS2 and GIS3 data separately.

The results of this joint fitting have been acceptable at 95% confidence level, as presented in figure 6.1a, with χ^2/d.o.f = 363/325 = 1.14. We plotted the derived normalizations for the five rings in figure 6.1b. Thus, the normalizations are consistent with 1.0 within ±5% level. If all the relative normalizations are fixed to 1.0, χ^2/d.o.f becomes 448/325 = 1.40 and the model is rejected at 99% confidence level. However, if we remove the spectrum of the 20–25 mm outermost ring, the model again becomes acceptable at 95% confidence level, with χ^2/d.o.f = 292/260 = 1.14. This is probably because the GIS performance, such as gain, energy resolution, and detection efficiency, gets worse beyond the 20 mm radius. If we compare GIS2 and GIS3, the best fit parameters are consistent except that the normalization of GIS3 is $\sim$ 3.5% larger than than that of GIS2.

Thus, we conclude that differences of the detector ID (GIS2 / GIS3) or the integration region (except > 20 mm) do not affect fitting parameters significantly. This confirms that the CXB ARF has been created with a safficient accuracy and reliability. Therefore, in the following analyses, we sum up GIS2 and GIS3 spectra within 20 mm from the optical axis. We come back to these ring-sorted CXB specra in §6.4.4 to evaluate the systematic errors.

6.3 Spectral fits to the average CXB in the LSS field

6.3.1 Results in the 2–10 keV range

As seen in the previous section, we can get roughly similar results regardless of the detector ID almost all over the whole GIS f.o.v. We therefore conduct a spectral fitting using the CXB spectrum of the all LSS observations integrated within the radius of 20 mm, in order to get higher statistics. The total exposure time is 515.4 ks, and the number of signal photons we obtained with the two GIS detectors is 187,726 counts in the 0.6–10 keV energy band. We estimate that about 32% of these events are due to RNXB. The data

also contain 23 point sources of $F_X^{2-10keV} > 2 \times 10^{-13}$ erg s^{-1} cm^{-2}, with their total flux $\sim 5.2 \times 10^{-12}$ erg s^{-1} cm^{-2}, in the 7.2 deg^2 area of the LSS sky (Ueda 1996). Therefore, this spectrum is not an unresolved CXB spectrum for ASCA. However, we quantify this spectrum including point sources for the moment.

First of all, we fit the spectrum in the 2–10 keV energy band. As the fitting model, we choose power-law and thermal bremsstrahlung models, both modified with absorption due to the Galactic column density of $N_H = 1.1 \times 10^{20}$ cm^{-2} which is appropriate for the LSS sky. They are generally accepted models to explain the CXB spectrum in the 2–10 keV energy band. Fitting results are shown in figure 6.3 and table 6.1. The fit with the power-law model is acceptable, and the derived photon index is $\Gamma = 1.496 \pm 0.026$. This is a little steepr than the generally accepted value of 1.4, but probably consistent within various systematic uncertainties. Thermal bremsstrahlung model is rejected at 99% confidence level, and shows rather high temperature of $kT = 19.8 \pm 2.3$ keV, which is practically meaningless value considering the energy range of ASCA (up to $\sim$ 10 keV). Since we

Table 6.1: Model fits to the 2–10 keV spectrum of the CXB

Model	absorbed power-law*	absorbed thermal bremsstrahlung*
χ^2/d.o.f	89 / 74	114 / 74
Parameter	$\Gamma = 1.496 \pm 0.026$	$kT = 19.8 \pm 2.3$ keV
Flux (2–10 keV)	6.12×10^{-8} (erg s^{-1} cm^{-2} str^{-1})	5.99×10^{-8} (erg s^{-1} cm^{-2} str^{-1})

* Absorption is fixed to the Galactic line-of-sight value ($N_H = 1.1 \times 10^{20}$ cm^{-2}).

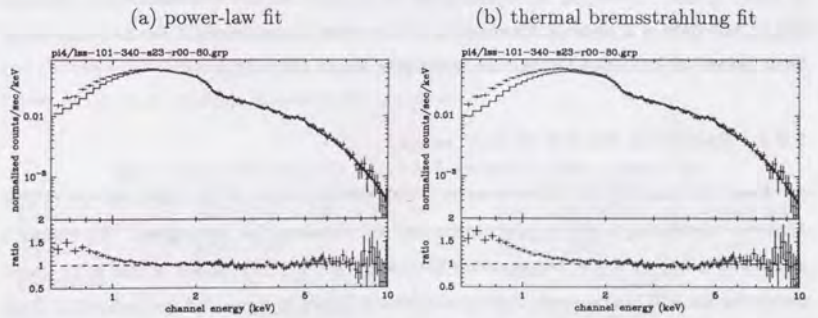

Figure 6.3: The average CXB spectrum fitted with (a) power-law and (b) thermal bremsstrahlung model, both with galactic absorption, in the 2–10 keV band. Upper panel of each figure shows GIS2+3 spectrum (crosses) and the best fit models (solid lines). Although the fitting ignored the energy range below 2 keV, the best-fit model is extended to < 2 keV to illustrate the soft-excess.

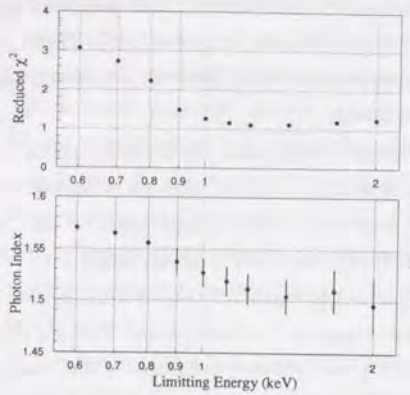

Figure 6.4: Changes of χ^2/d.o.f (upper panel) and the CXB photon index (lower panel) when the lower limit of the fitting energy range is shifted down from 2.0 keV to 0.6 keV, with upper limit fixed to 10 keV. Error bars of photon indices at 0.6–0.8 keV are not plotted becase χ^2 is too big to evaluate the errors.

can get an acceptable fit with the absorbed power-law model, we hereafter evaluate the 2–10 keV energy band spectrum with the power-law model, and call this component "hard power-law component" ($PL^{\rm hard}$). Comparison of the observed $PL^{\rm hard}$ with the previous measurements will be performed in chapter 8.

If we extrapolate the fitted model below 2 keV, we can see a significant excess of data above the model (soft-excess). This soft-excess becomes significant at ~ 1.2 keV, and the ratio of data to model increases to about 1.5 at 0.7 keV (lower panel of figure 6.3). Thus, the GIS data have comfirmed the existence of the soft-excess in the CXB spectrum, which has already been known with previous observations of the CXB (ref. §2). In order to show the soft-excess more clearly, we plot the change of reduced χ^2 and photon index of $PL^{\rm hard}$ in figure 6.4, as a function of lower-bound energy used for the spectral fitting. Because of the soft-excess, a single power-law model becomes unacceptable if we move the lower limit below 0.9 keV, and the photon index gets larger accordingly.

6.3.2 Results in the 0.6–10 keV range

Then, we quantify the soft-excess by fitting the spectrum in the whole energy of 0.6–10 keV, introducing a soft model component to represent the soft-excess. We choose a steep power-law or a low temperature Raymond-Smith (RS) model of one solar abundances as the soft component. Fitting results are shown in figure 6.5 and table 6.2. Both these models have given acceptable fits in the 0.6–10 keV energy band. If we choose a steep power-law as the soft component, its photon index shows very steep value of $\Gamma = 6.42 \pm 0.76$. Similarly, if we choose a low temperature RS model, its temperature shows a very low value of $kT = 0.31^{+0.15}_{-0.08}$ considering the GIS energy range (down to ~ 0.6 keV). Flux of the soft component in the 0.5–2 keV energy band is also shown in

table 6.2. The two soft-excess models cannot be distinguished from each other in view of the fit χ^2. However, the calculated soft component flux depends significantly on the choice between these two.

Because the power-law model is easier to evaluate errors than the RS moldel, we first use the steep power-law as the soft component in evaluating the fitting errors. Hereafter we call this component "soft power-law component" ($PL^{\rm soft}$). Figure 6.6 shows error contours between various pairs of the $PL^{\rm hard}$ and $PL^{\rm soft}$ parameters. There are correlations between the photon index Γ and the flux $F_{\rm X}$ for both $PL^{\rm hard}$ and $PL^{\rm soft}$, but the directions of the correlations are different from each other. With respect to the $PL^{\rm hard}$, $F_{\rm X}^{\rm hard}$ increases as $\Gamma^{\rm hard}$ gets flatter, while $F_{\rm X}^{\rm soft}$ increases as $\Gamma^{\rm soft}$ gets steeper. We note that these confidence contours does not include the effect of systematic errors, which we disscuss in detail in

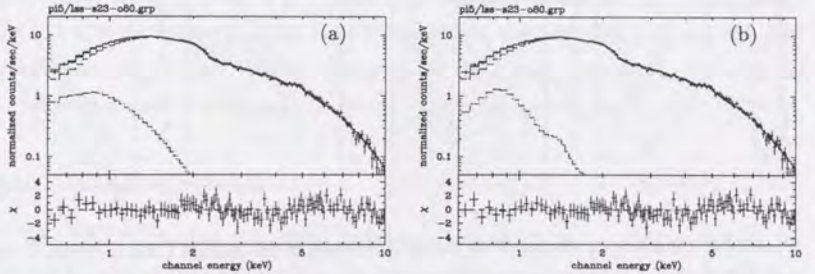

Figure 6.5: The average CXB spectrum in the LSS field, fitted in the entire 0.6–10 keV energy band with an absorbed power-law models plus a soft component. The soft component is represented by (a) a steep power-law or (b) a low temperature RS model of 1 solar abundances. Upper panel of each figure shows GIS2+3 spectrum (crosses), the best fit models (solid lines), the absorbed power-law component (dashed lines) and the soft component (dot-dashed lines). Lower panels show residuals plotted in the unit of σ.

Table 6.2: Model fits to the 0.6–10 keV spectrum of the average CXB

Model	power-law + abs. power-law*	Raymond-Smith + abs. power-law*
χ^2/d.o.f	105.7 / 100	103.7 / 100
Parameter	$\Gamma^{\rm hard} = 1.486 \pm 0.021$	$\Gamma^{\rm hard} = 1.502 \pm 0.017$
	$\Gamma^{\rm soft} = 6.41 \pm 0.76$	$kT = 0.31^{+0.15}_{-0.08}$ keV
$F_{\rm X}^{\rm hard}$ (2–10 keV)‡	6.14×10^{-8} (erg s^{-1} cm^{-2} str^{-1})	6.11×10^{-8} (erg s^{-1} cm^{-2} str^{-1})
$F_{\rm X}^{\rm soft}$ (0.5–2 keV)†	1.40×10^{-8} (erg s^{-1} cm^{-2} str^{-1})	0.48×10^{-8} (erg s^{-1} cm^{-2} str^{-1})

* Absorption is fixed to the Galactic line-of-sight value ($N_{\rm H} = 1.1 \times 10^{20}$ cm^{-2}).

‡ Flux of the hard power-law component in the 2–10 keV band.

† Flux of the soft component in the 0.5–2 keV band.

the next section.

Similarly, figure 6.7 shows error contours for $PL^{\rm hard}$ + RS model. If we take RS normalization as $F_{\rm X}^{\rm soft}$ and take $(kT)^{-1}$ as $\Gamma^{\rm soft}$, these correlations resemble those of figure 6.6. It appears that the fit with the low temperature RS wants lower element abundances, as seen in figure 6.5b. If we free the abundances of the RS model with their ratio fixed to the solar value, we get abundances A = 0.09 solar, and kT = 0.28 keV at χ^2/d.o.f = 102.1/104. However, these parameters are very poorly determined as shown in the confidence contour of kT vs. abundances (figure 6.8).

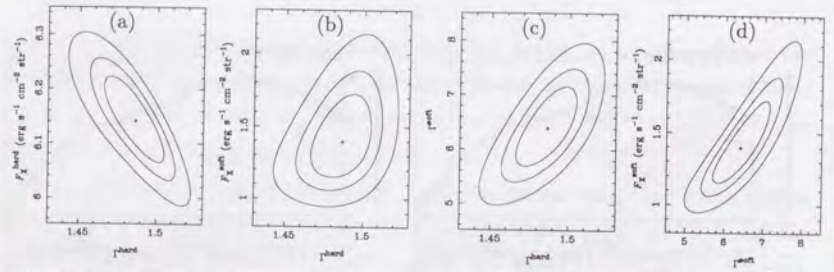

Figure 6.6: Confidence contours of the fitting parameters to the average CXB spectrum in the LSS field with the absorbed power-law ($PL^{\rm hard}$) + steep power-law ($PL^{\rm soft}$) model shown in figure 6.5a. Contours (from inner to outer) represent 68, 90 and 99% confidence levels. Crosses show the best fit position. (a) Photon index of $PL^{\rm hard}$ ($\Gamma^{\rm hard}$) vs. 2–10 keV band flux of $PL^{\rm hard}$ ($F_{\rm X}^{\rm hard}$). (b) $\Gamma^{\rm hard}$ vs. 0.5–2 keV band flux of $PL^{\rm soft}$ ($F_{\rm X}^{\rm soft}$). (c) $\Gamma^{\rm hard}$ vs. Photon index of $PL^{\rm soft}$ ($\Gamma^{\rm soft}$). (d) $\Gamma^{\rm soft}$ vs. $F_{\rm X}^{\rm soft}$.

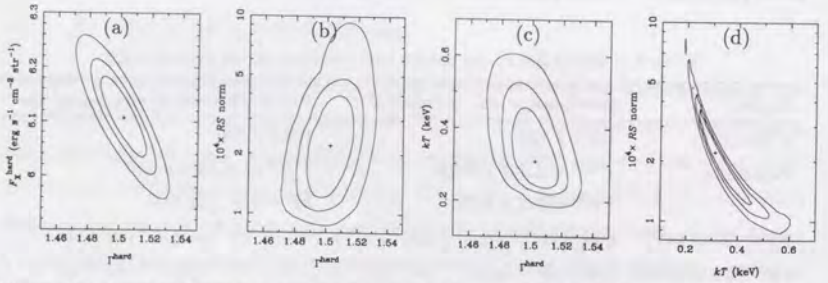

Figure 6.7: Same as figure 6.7, but for the absorbed power-law ($PL^{\rm hard}$) + Raymond-Smith (RS) model shown in figure 6.5b. (a) $\Gamma^{\rm hard}$ vs. $F_{\rm X}^{\rm hard}$. (b) $\Gamma^{\rm hard}$ vs. RS normalization. (c) $\Gamma^{\rm hard}$ vs. RS temperature. (d) RS temperature vs. RS normalization.

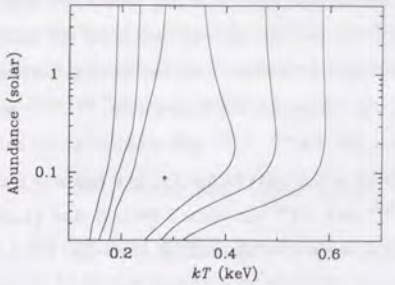

Figure 6.8: Confidence contour of RS temperature vs. RS abundance, when fitting the average CXB spectrum in the LSS field with $PL^{\rm hard}$ + RS model. Contours (from inner to outer) represent 68, 90 and 99% confidence levels. Cross shows the best fit position.

6.4 Systematic error of the CXB spectrum

In this section, we examine the effects of the systematic errors on the fitting parameters, mainly about $\Gamma^{\rm hard}$ and $F_{\rm X}^{\rm soft}$. Considered systematic errors are RNXB subtraction (§6.4.1), GIS low energy response (§6.4.2), stray light evaluation (§6.4.3), and the XRT effective area uncertainty (§6.4.4). Although we check these systematic error with the LSS spectrum, error regions must be true of other CXB spectra, too.

6.4.1 RNXB uncertainty

The RNXB (residual non X-ray background) spectrum to be subtracted from the raw CXB spectrum was created from the night-earth data utilizing the $H02$ distribution (for the H02-sorting method), considering the mean observation epoch (for the long-term RNXB trend correction), as described in §4.4.4. The prediction is subject to about 3.5% systematic error (table 4.7). However, we adopt the ±2.5% systematic error in this section, because of the reasons mentioned in §6.1.

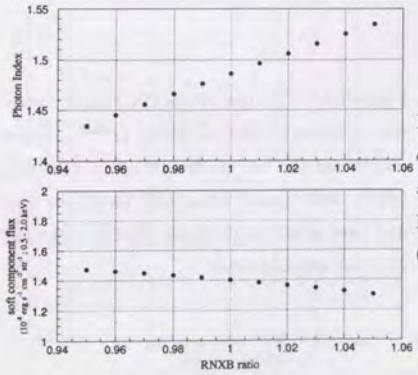

Figure 6.9: Changes of the CXB hard power-law component photon index ($\Gamma^{\rm hard}$; upper panel) and the soft power-law component flux ($F_{\rm X}^{\rm soft}$; lower panel) when the RNXB level is scaled to 0.95–1.05 from the nominal value.

In order to evaluate how the RNXB uncertainty affects the fitting results, we scaled the RNXB spectrum by -5% to $+5\%$ from the prediction, and examined the corresponding change of the best fit parameters. Figure 6.9 shows the results of this study. Since the RNXB spectrum has a flatter profile than the CXB spectrum, $PL^{\rm hard}$ gets steeper as we substract RNXB more. As for the $PL^{\rm soft}$, $F_{\rm X}^{\rm soft}$ gets smaller as we substract RNXB more, because the RNXB spectrum is extending straight below 1 keV where the CXB counts drop. Therefore, $\Gamma^{\rm hard}$ and $F_{\rm X}^{\rm soft}$ can vary 1.46–1.51 and (1.36–1.44) $\times 10^{-8}$ erg s^{-1} cm^{-2} str^{-1}, respectively, in respect to the $\pm 2.5\%$ systemaic error of the RNXB subtraction.

6.4.2 GIS low energy response uncertainty

In order to quantify the soft component of the CXB, we must know the accurate response of the GIS in the lower energy bands. In this subsection, we evaluate the systematic error caused by the uncertainty of the GIS low energy response. It is the Be entrance window that dominates the low energy response of the GIS (figure 4.3). The thickness of the Be foil was measured in the pre-launch calibration with an accuracy of ~ 0.1 μm (Ueda 1992), and the results showed variations over 10.7–11.1 μm and 10.45–10.55 μm for GIS2 and GIS3, respectively, depending on the foil positions. Variations in the absorption column density by about $\pm 2 \times 10^{20}$ cm^{-2} was also seen in the Crab spectra obtained at different positions (figure 4.10c). This variation by $N_{\rm H} \sim 2 \times 10^{20}$ cm^{-2} corresponds to 0.5 μm in berylium thickness.

We examined the change of the best fit CXB parameters, by artificially changing the Be window thickness. Figure 6.10 shows the best fit value of $\Gamma^{\rm hard}$ and $F_{\rm X}^{\rm soft}$ plotted versus adittional Be window thickness. Although $\Gamma^{\rm hard}$ is little affected by the Be

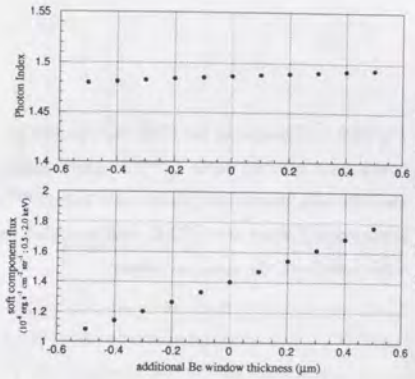

Figure 6.10: Changes of the CXB hard power-law component photon index ($\Gamma^{\rm hard}$; upper panel) and the soft power-law component flux ($F_{\rm X}^{\rm soft}$; lower panel) when GIS beryllium window have adittional thickness of -0.5 – $+0.5$ μm from the nominal value.

thickness, $F_{\rm X}^{\rm soft}$ are significantly affected. $F_{\rm X}^{\rm soft}$ gets larger as Be window gets thicker, because the detection efficiency of the GIS drops in low energy bands. If we assume the uncertainty of the Be window thickness by about ± 0.3 μm, $F_{\rm X}^{\rm soft}$ can vary by (1.20–1.61) $\times 10^{-8}$ erg s^{-1} cm^{-2} str^{-1}.

6.4.3 XRT stray light uncertainty

As described in §4.3, we cannot neglect the stray light effects in creating the CXB ARF. In this subsection, we evaluate the systematic errors caused by the uncertainty in the stray light fraction to the normal reflection component. The stray light effects have been calibrated by the large offset observations of the Crab nebula (ref. §4.3.3). As far as $\theta \lesssim 80'$, in which most of the CXB photons come from, the ray-tracing program can reproduce the stray lights from the Crab nebula pretty well, within the range of -30–$+10\%$. We also note that the stray lights mainly consist of the secondary only reflection and the multiple reflection components (figure 4.15).

We examined the change of the best fit CXB parameters, by changing the fraction of the secondary only reflection or the multiple reflection component, in the range of -30–$+10\%$ from the nominal value obtained with the ray-tracing program. Figure 6.11 shows the results of this study. Since multiple reflection component significantly increases in

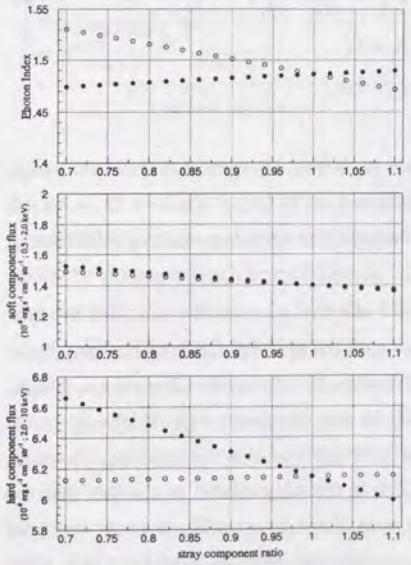

Figure 6.11: Changes of the CXB hard power-law component photon index ($\Gamma^{\rm hard}$; upper panel), the soft power-law component flux ($F_{\rm X}^{\rm soft}$; middle panel), and the hard power-law component flux ($F_{\rm X}^{\rm hard}$; lower panel), when stray light (filled circles for secondary only reflection, open circles for multiple reflection) level is scaled to 0.7–1.1 from the nominal value derived in §4.3.

the lower energy bands, $PL^{\rm hard}$ gets flatter due to the increase of the soft band effective area, when we increase the multiple reflection component. $F_{\rm X}^{\rm soft}$ does not show particular changes, because the reflectivity of the XRT foils are almost constant below $\sim$ 2 keV. Since the secondary only reflection component has similar energy dependence with that of the normal reflection, changing the fraction of the secondary only component does not significantly affect $\Gamma^{\rm hard}$ or $F_{\rm X}^{\rm soft}$. However, it affects $F_{\rm X}^{\rm hard}$ by $\sim$ 10% level. From these considerations, we estimate the systematic error of $\Gamma^{\rm hard}$ due to the stray light uncertainty to be 1.47–1.53.

6.4.4 XRT effective area uncertainty

If we fit the ring-sorted spectra shown in §6.2 one by one, $PL^{\rm hard}$ of outer rings appear to be flatter than those of inner rings, as shown in figure 6.12b by filled circles. Also the $F_{\rm X}^{\rm hard}$ values of the inner rings appear to be smaller by $\sim$ 5% compared with those of outer rings. These trends are also seen in the Crab pointings which has been carried out at various detector positions (figure 4.10). It is possibly because the ray-tracing program cannot perfectly reproduce the position- and energy-dependence of the XRT effective area. In order to compensate these incompleteness of the XRT effective area, we try introducing an artificial correction factor for the XRT effective area represented by an analytic formula:

$$f(\theta,E) = 1 - p\cdot\exp\left(-\frac{\theta^2}{2a^2}\right) + q\cdot\exp\left(-\frac{(\theta-\theta_b)^2}{2b^2}\right) \qquad (6.1)$$

$$\begin{cases} a = 5, \quad b = 2.5, \quad \theta_b = 14 \\ p = 0.2\ (1-\exp(-E/3.0)) \\ q = 0.05 - 0.002E \end{cases}$$

where θ (arcmin) and E (keV) means the offset angle from the optical axis and the energy of the incident X-ray, respectively, as previously defined in §4.2.1. Figure 6.13 shows this function, superposed on to the ratio of the observed flux to the ray-tracing prediction at each point of the Crab observations.

We re-created the CXB ARF using the XRT effective area which is modified by equation (6.1), and again fit the ring-sorted spectra with the modified CXB ARF. Open circles in figure 6.12 show the results. Since this modification have little effect beyond $r \sim 20$ mm, fitting results are almost unchanged in the 20–25 mm outermost ring. If we neglect the outer most ring, photon indices become nearly constant by this modification. However, $F_{\rm X}^{\rm hard}$ of the inner rings gets large in turn. This is probably related to the fact that the ray-tracing program seems to over-estimate stray lights by $\sim$ 10%. If we fit the total spectrum integrated inside 20 mm from the optical axis with the modified CXB ARF,

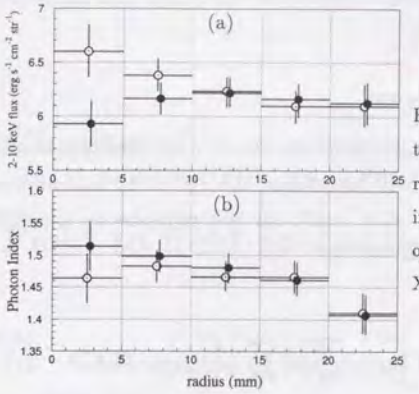

Figure 6.12: (a) Flux and (b) photon index of the ring-sorted CXB spectra plotted versus the radius of each ring. Filled circles show the fitting results with the nominal XRT response, and open circles show the results with the modified XRT response.

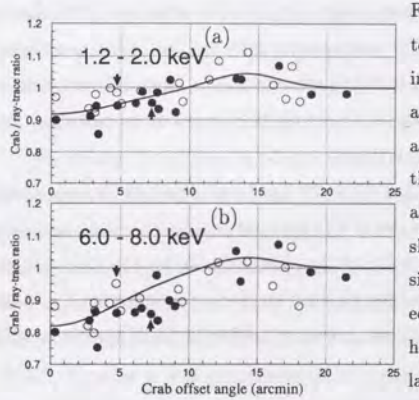

Figure 6.13: Ratio of the observed Crab counts to that predicted by the ray-tracing calculation in (a) 1.2–2.0 keV and (b) 6.0–8.0 keV plotted against the offset angle from the XRT optical axis. Integration radius is 6 mm centered on the Crab nebula. Filled circles represent GIS2 and open circles GIS3. The point with an arrow show the observation at the 1CCD nominal position. Smooth solid lines show the function of equation (6.1). We assume that the Crab nebula has a constant spectrum of an absorbed power-law, i.e. $\Gamma = 2.1$, $norm = 9.7$ c s^{-1} cm^{-2} keV^{-1}, and $N_{\rm H} = 3.0 \times 10^{21}$ cm^{-2}.

we get $\Gamma^{\rm hard} = 1.468$ and $F_{\rm X}^{\rm soft} = 1.46 \times 10^{-8}$ erg s^{-1} cm^{-2} str^{-1}. Since these values agree with those derived with the nominal CXB ARF (table 6.2), we do not find the necessity of introducing the modification. Therefore, we do not apply the XRT effective area correction by equation (6.1) in the following analyses.

The accuracy of the XRT effective area directly affects the ARF normalization, hence absolute flux of the CXB. The normalization of the CXB ARF which we have used in fitting the CXB spectra is determined from the deep Crab observation at 1CCD nominal position (ref. §4.2.5). However, the Crab flux measured with the GIS itself varies by $\sim$ 10%, depending on the pointing position of the Crab nebula (figure 6.13). This is probably due to the shadowing of the support grids on the GIS entrance window. Since there exists $\sim$ 10% error on the reference flux, the absolute flux of the CXB also have at

least $\sim 10\%$ uncertainty. This uncertainty is comparable or rather large than that caused by the stray light uncertainty (ref. §6.4.3).

6.4.5 Summary of the systematic errors

In table 6.3, we summarize the systematic errors considered in the preceding subsections. $\Gamma^{\rm hard}$ is the most affected by the RNXB uncertainty, and $F_{\rm X}^{\rm soft}$ is the most affected by the Be window thickness uncertainty. As a result, our best estimates for the CXB parameters for the LSS field can be summarized as:

$$\begin{aligned} \Gamma^{\rm hard} &= 1.486 \quad \pm 0.021 \quad \pm 0.040 \\ F_{\rm X}^{\rm hard} &= 6.14 \quad \pm 0.08 \quad \pm 0.92 \quad (10^{-8}\ {\rm erg\ s^{-1}\ cm^{-2}\ str^{-1}}) \\ F_{\rm X}^{\rm soft} &= 1.40 \quad \pm 0.27 \quad \pm 0.22 \quad (10^{-8}\ {\rm erg\ s^{-1}\ cm^{-2}\ str^{-1}}), \end{aligned} \tag{6.2}$$

where the former error represents the 90% confidence level statistic erorr and the latter represents the systematical errors. The systematic error for the absolute CXB flux is $\sim 15\%$ (10% by the stray light uncertainty and another 10% by the absolute effective area uncertainty). However, relative errors in fluxes measurements, from different field to field, should be much smaller. We estimate the relative flux errors to be less than 3%, taking into account the $\sim 3.5\%$ RNXB uncertainty.

Furthermore, it must be noted that the XRT+GIS has been adjusted in such a way that the Crab nebula spectrum observed at the 1CCD nominal position becomes as shown in table 4.4. Whereas, generally accepted value of the photon index for the Crab nebula is $\Gamma \sim 2.1$. We emphasize that our response gives a little steep photon index by $\Gamma \sim 0.06$. Therefore, $\Gamma^{\rm hard}$ can be ~ 1.4, if we modify our response to fit the Crab spectrum with $\Gamma = 2.10$.

Table 6.3: Summary of the systematic errors for the CXB spectrum in the LSS field

Origin	uncertainty	Error region of Photon Index	Error region of soft component flux (10^{-8} erg s^{-1} cm^{-2} str^{-1})	ref.
RNXB to be subtracted	$\pm$ 2.5%	1.461 – 1.511	1.36 – 1.44	§ 6.4.1
Be window thickness	$\pm$ 0.3 μm	1.482 – 1.490	1.20 – 1.61	§ 6.4.2
stray light strength	-30% – $+10\%$	1.472 – 1.531	1.37 – 1.49	§ 6.4.3
XRT effective area	$\lesssim 20\%$	1.468 – 1.486	1.40 – 1.46	§ 6.4.4
Total*	—	1.486 ± 0.040	1.40 ± 0.22	—

* Quadratic sum of all errors.

Chapter 7

Field to field properties of the CXB

7.1 CXB spectra of individual fields including point sources

We have studied the average CXB spectrum in the LSS field in chapter 6, and have established the method of quantifying the CXB spectrum using the GIS data. Then, as a next step, we examin the CXB properties in the other fields described in chapter 5. We also split the overall LSS observations into four groups, a-LSS, b-LSS, c-LSS, and d-LSS, as described in §5.2.1, and analyze them individually.

We created the spectrum of each field just in the same way as the average LSS spectrum was created. All events inside 20 mm from the optical axis were utilized, even though point sources are clearly present in most of the f.o.v. Each RNXB spectrum to be subtracted was generated by the H02-sorting method with the normalization adjusted to correct the long-term RNXB trend. We fitted each spectrum thus created with the $PL^{\rm hard} + PL^{\rm soft}$ model, using the same RMF and ARF as were used to fit the LSS spectrum. We fixed $\Gamma^{\rm soft}$ to 6.0, because it was practically unconstrained in several fields, due to low statistics or poor fits to the data (e.g. NEP). Absorption column for $PL^{\rm hard}$ was also fixed, according to the information from *EINLINE*, as given in table 7.1. The fitting results are summarized in table 7.1. We also show all the spectra in appendix D.

The errors shown in table 7.1 are the 90% confidence level statistical errors, and do not include the systematic errors. However, systematic errors due to uncertainty of the XRT+GIS response are common to all the fields, so that the RNXB uncertainty of $\sim$ 3.5% is the dominant systematic error when we compare different fields. If we ignore the NEP about which we cannot get an appropriate fit, the values for $\Gamma^{\rm hard}$ are distributed in the range of 1.39–1.55, and the $F_{\rm X}^{\rm hard}$ values in the range of (5.5–6.7)$\times 10^{-8}$ erg s^{-1} cm^{-2} str^{-1}. Mean values and standard deviations are 1.461 ± 0.047, and $(6.10 \pm 0.30) \times 10^{-8}$ erg s^{-1} cm^{-2} str^{-1}, respectively. Thus the relative 1σ variation of $F_{\rm X}^{\rm hard}$ is 5.0%, which is a little larger than both statistical and systematic errors. Variation of $\Gamma^{\rm hard}$ is marginal, considering the systematic errors. The Arp 220 and 3C368

fields show apparently larger F_X^{soft}.

Among these fields, particularly the NEP spectrum could not be fitted with the $PL^{hard} + PL^{soft}$ model, as shown in figure 7.1. The NEP spectrum shows clear excess around 6 keV, which is undoubtedly due to the Seyfert 2 galaxy NGC 6552 (Fukazawa et al. 1994) which happen to be in the f.o.v. This exemplifies that the CXB observations which are restricted in a small region have a risk of being influenced by particular point sources. However, ASCA has an imaging capability, so that we can remove point sources brighter than some levels depending on the deepness of the exposure. In the next section, we consider removing point sources in the observed fields in order to study the remaining CXB spectra.

Table 7.1: (PL^{hard}+PL^{soft}) fits to the 0.6–10 keV spectrum of each field including point sources. All errors are 90% confidence level. Γ^{soft} is fixed to 6.0.

ID	Name	Exp.†	Area‡	$N_H^\sharp$	χ^2/d.o.f	Γ^{hard}	$F_X^{hard\triangleleft}$	F_X^{soft*}
1	SA57	461,343	0.68	1.0	69.0/67	1.414 ± 0.017	6.00 ± 0.09	1.31 ± 0.14
2	a-LSS	119,221	2.09	1.1	101.0/67	1.446 ± 0.032	5.85 ± 0.16	0.75 ± 0.26
3	b-LSS	130,206	2.32	1.1	84.0/67	1.444 ± 0.031	6.07 ± 0.15	1.28 ± 0.26
4	c-LSS	138,641	2.27	1.1	52.6/67	1.461 ± 0.030	5.93 ± 0.15	1.32 ± 0.26
5	d-LSS	127,324	2.19	1.1	57.6/67	1.552 ± 0.028	6.73 ± 0.16	1.64 ± 0.30
6	Draco	57,002	0.71	4.1	94.7/67	1.494 ± 0.048	5.47 ± 0.22	1.42 ± 0.38
7	NEP	118,434	0.58	4.2	217.4/67	$1.257 \pm 0.000^*$	$6.70 \pm 0.00^*$	$2.41 \pm 0.00^*$
8	QSF3	60,157	0.43	1.7	60.2/67	1.429 ± 0.044	6.15 ± 0.22	1.42 ± 0.38
9	ZSYS	109,893	1.68	2.3	28.7/67	1.474 ± 0.032	6.41 ± 0.17	0.93 ± 0.29
10	BF	114,738	1.47	1.2	117.5/67	1.524 ± 0.030	6.46 ± 0.16	0.57 ± 0.30
11	Jupiter	20,389	0.40	2.1	64.6/67	1.521 ± 0.076	5.99 ± 0.37	1.01 ± 0.67
12	Arp 220	23,039	0.40	4.2	78.7/67	1.393 ± 0.077	5.64 ± 0.35	4.77 ± 0.66
13	3C368	19,934	0.40	9.8	104.5/67	1.480 ± 0.078	6.10 ± 0.38	4.64 ± 0.70

† Total exposure time (s).

‡ Integration area (deg^2) on the sky.

♯ Absorption for PL^{hard} (10^{20} cm^{-2}) from Einstein On-line Service (*EINLINE*). Fixed while fitting.

◁ Flux of PL^{hard} (10^{-8} erg s^{-1} cm^{-2} str^{-1}) in the 2–10 keV energy band.

* Flux of PL^{soft} (10^{-8} erg s^{-1} cm^{-2} str^{-1}) in the 0.5–2 keV energy band.

* χ^2 is too big to evaluate errors.

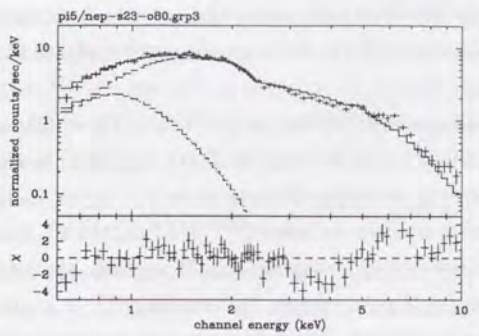

Figure 7.1: The NEP spectrum fitted with the $PL^{hard} + PL^{soft}$ model in the 0.6–10 keV energy band. PL^{hard} is modified with Galactic absorption of $N_H = 4.2 \times 10^{20}$ cm^{-2}. Upper panel shows GIS2+3 spectrum (corosses), the best fit models (solid lines), the absorbed PL^{hard} component (dashed lines), and the PL^{soft} component (dot-dashed lines). Lower panel shows residuals plotted in the scale of σ.

7.2 How to eliminate point sources

7.2.1 Outline of the source-finding

We consider eliminating point sources brighter than a certain fixed level, in order to better quantify the CXB properties. To do this, we have to detect point sources and evaluate their fluxes (source-finding). We carried out the source-finding on the GIS image taken in the 0.7–7.0 keV energy band in the following way.

We first rebinned the image by 2×2 pixels into 0.5×0.5 mm resolution, in order to speed up the image analyses. Since the XRT+GIS response is not so sharp ($\sim 3'$ in half power diameter) and has severe offset-angle-dependence (ref. §4.2), subsequent procedure of the source-finding is somewhat complicated. The image $B^{OBS}(DETX, DETY)$ observed with the XRT+GIS system can be decomposed into:

$$B^{OBS}(DETX, DETY) = B^{RNXB}(DETX, DETY) \quad (7.1)$$

$$+ B^{UCXB}(DETX, DETY) \quad (7.2)$$

$$+ \sum_i B_i^{PS}(DETX, DETY), \quad (7.3)$$

where B^{RNXB} is the RNXB image, B^{UCXB} is the image of the CXB that cannot be resolved into point sources (unresolved CXB), and B_i^{PS} are the images due to point sources in the f.o.v. Here, B^{UCXB} also includes the image created by the stray lights. Although the boundary between B^{UCXB} and B_i^{PS} is not necessarily well defined, the ambiguity does not matter as far as we deal with point sources that are bright enough ($\gtrsim 10^{-13}$ erg s^{-1} cm^{-2}).

In order to single out $\sum_i B^{PS}$, we try estimating B^{RNXB} and B^{UCXB}. As for B^{RNXB}, we can estimate it just in the same way as was done in §4.4.4. Therefore, we generated it

by the H02-sorting method with correction for the long-term RNXB trend. On the other hand, it is a difficult issue to estimate B^{UCXB}. Among several choices, we have decided to utilize the entire LSS data in combination with the day-earth image B^{DYE} (figure 3.15) in the following way.

As described in §6.1, the LSS data provide the best sample of the CXB, so that we basically utilized the entire LSS data to construct the template CXB image when observed with the XRT+GIS. We first summed up the entire LSS data in the 0.7–7.0 keV energy band on $DETX$-$DETY$ coordinates to generate the image $B^{LSS}(DETX, DETY)$. Even though they have been averaged to some extent by summing up 76 pointings, the result is still subjected to local clumpiness due to point sources. Furthermore, B^{LSS} is at most 5 c pixel^{-1}, and are not satisfactory in statistics, either. Therefore, we smoothed B^{LSS} with a Gaussian of $\sigma = 2$ pixel, and azimuthly averaged B^{LSS} centered on the optical axis to create an azimuthly-averaged radial-profile $R^{LSS}(r)$ as:

$$R^{LSS}(r) = \frac{\int d\phi \; smo\left[B^{LSS} - B^{RNXB}\right]}{\int d\phi \; smo\left[B^{MASK}\right]}, \tag{7.4}$$

where B^{MASK} is the standard image masking (figure 4.20), and $smo\left[B\right]$ represents the operation of the Gaussian smoothing. Applying these procedures, the local clumpiness was smeared out and the statistics were much improved. However, this procedure has also smeared out local instrumental structures such as shadows cast by the window support grids of the GIS (figure 3.15). Although such local instrumental structures imprinted on the CXB image are difficult to model analytically, we can reproduce the patterns utilizing the day-earth image B^{DYE}, which has very high statistics (40–80 c pixel^{-1}) and is created by a reasonably uniform source. We therefore created $B^{\overline{CXB}}$ as:

$$B^{\overline{CXB}}(DETX, DETY) = \frac{R^{LSS}(r)}{R^{DYE}(r)} \times (B^{DYE} - B^{RNXB}), \tag{7.5}$$

where R^{DYE} is the radial-profile of B^{DYE}. This $B^{\overline{CXB}}$ can be regarded as the template image of the CXB, in which contributions of the point sources in the LSS field (up to $F_X^{2-10\,\mathrm{keV}} \sim 2 \times 10^{-12}$ erg s^{-1} cm^{-2}) have been flattened out (but not subtracted).

In creating $B^{\overline{CXB}}$ via equation 7.5, we integrated the day-earth data in the 1.0–3.0 keV energy band to reduce the RNXB fraction. GIS2 and GIS3 were treated separately, and two $B^{\overline{CXB}}$ were created for GIS2 and GIS3, respectively. We have examined the azimuth-angle-dependence of B^{DYE}, and did not find significant structure over ±5%. This justifies the procedure of azimuthly-averaging to create $B^{\overline{CXB}}$. We think this approximation of equation (7.5) gives a sufficient quality for the template CXB image. Then, we assume that B^{UCXB} can be approximated as:

$$B^{UCXB}(DETX, DETY) = \alpha \times B^{\overline{CXB}}(DETX, DETY), \tag{7.6}$$

where α is a positive constant value less than 1.0, which gives the fraction of the CXB unresolved with the XRT+GIS. This factor α is expected to be mainly determined by the imaging performance of the XRT+GIS system, and not to vary significantly field to field. We will evaluate the value of α in the next subsection.

Supposing that B^{RNXB} and B^{UCXB} have been known, we can extract the contribution of point sources as:

$$\sum_i B_i^{PS}(DETX, DETY) = B^{OBS} - B^{RNXB} - B^{UCXB}. \tag{7.7}$$

Although the image produced with equation (7.7) contains full information on point sources, it is difficult to be utilized without smoothing. We therefore smooth it, just taking its cross correlation with the XRT+GIS point spread function, as described in §5.3.2. At the same time, using the knowledge of satellite Euler angles, we convert the image into the sky coordinates, for the purpose of creating a mosaic image. The operator $ccf\left[B\right]$ denotes this procedure, as defined by equation (5.4).

Finally, we can realized a nearly flat-field mosaic image for point sources, in which exposure, vignetting, and backgrounds (both RNXB and unresolved CXB) are cancelled, as:

$$M^{FLAT}(SKYX, SKYY) = \frac{\sum_j T_j \; ccf\left[B_j^{OBS} - B_j^{UCXB} - B_j^{RNXB}\right]}{\sum_j T_j \; det2sky\left[A^{PS}\right]}, \tag{7.8}$$

where j represents the pointing number in the field, and T_j represents the exposure time for the j-th pointing. The term of $A^{PS}(\theta, \phi)$ takes charge of the XRT vignetting, as defined in §5.3.2. On $M^{FLAT}(SKYX, SKYY)$, image peaks are expected to be seen at the positions where point sources are likely to exist. The peak value is expected to be precisely in proportion to its flux, because M^{FLAT} has been corrected for both exposure and vignetting. Therefore, we apply a fixed threshold on $M^{FLAT}(SKYX, SKYY)$, and consider that a point source exists where the pixel values exceed the threshold.

7.2.2 Determination of the CXB base level

Before actually performing the source-finding and subsequent source-elimination, we must fix the value of α in equation (7.6), which determins the base level of the unresolved CXB. To do this, we again utilized the LSS data. For this purpose, we created a mosaic image of the LSS observations as:

$$M^{RATIO}(SKYX, SKYY) = \frac{M^{RAW}}{M^{\overline{CXB}}} = \frac{\sum_j T_j \; ccf\left[B_j^{OBS} - B_j^{RNXB}\right]}{\sum_j T_j \; ccf\left[B_j^{\overline{CXB}}\right]}. \tag{7.9}$$

The numerator (M^{RAW}) and the denominator ($M^{\overline{CXB}}$) of M^{RATIO} are basically created from the same data set, i.e. entire LSS. However, the former is the raw event map with RNXB subtracted and then smoothed with the PSF, while the latter is our best estimate of the CXB, in which fluxes from resident point sources have been re-distributed almost uniformly over the entire survey area via equation (7.5). Therefore, $M^{RAW}/M^{\overline{CXB}}$ has a ratio less than 1.0 in most pixels where resolved point sources do not exist, although the mean values of M^{RAW} and $M^{\overline{CXB}}$ are equal.

Since the image excesses due to point sources are localized around the positions where individual sources are present, the pixel values of $M^{RATIO}(SKYX, SKYY)$ should have values close to α in off-source regions within statistical errors which vary from pixel to pixel. We show the mosaic images of M^{RAW}, $M^{\overline{CXB}}$ and M^{RATIO} in figure 7.2, 7.3, and 7.4, respectively.

Figure 7.2: Gray scale image of $M^{RAW} = \sum_j T_j \; ccf\left[B_j^{OBS} - B_j^{RNXB}\right]$ for the entire LSS observations. White and black pixel corresponds to 0.0 and 10.0 c pixel^{-1}, respectively.

Figure 7.3: Gray scale image of $M^{\overline{CXB}} = \sum_j T_j \; ccf\left[B_j^{\overline{CXB}}\right]$ for the entire LSS observations. White and black pixels correspond to 0.0 and 10.0 c pixel^{-1}, respectively.

To determine the most frequent pixel values on the M^{RATIO} map, we created histogram of the pixel values on M^{RATIO} as shown in figure 7.5. In order not to be affected by statistical errors, we discarded the pixels where $M^{\overline{CXB}} < 1.0$ c pixel^{-1}. This histogram consists of mainly three components. Firstly, it is contributed by the Poisson error due

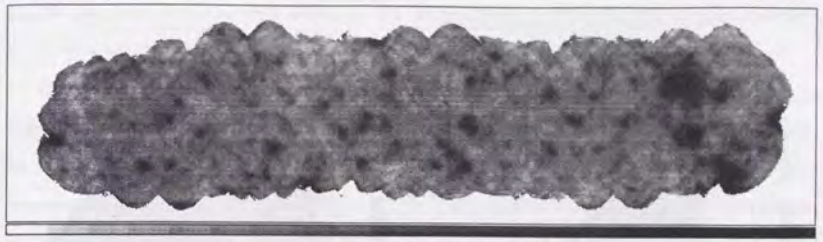

Figure 7.4: Gray scale image of $M^{RATIO}(SKYX, SKYY)$ for the entire LSS observations. White pixel corresponds to 0.0 and black pixel corresponds to 3.0. Values of pixels where $M^{\overline{CXB}} < 1.0$ c pixel^{-1} are set to 0.0.

to photon counting statistics. This effect is not easy to evaluate, because of the multi-exposure nature and the $ccf\left[B\right]$ operation. Considering that the pixel values of M^{RAW} range over $\sim$ 1–5 c pixel^{-1}, and $ccf\left[B\right]$ operation reduces statistical errors typically by $\sim$ 17%, we estimate the contribution of the Poisson error to the peak width to be 0.16–0.07. Secondly, the CXB fluctuation due to unresolved sources further broaden the peak. Lastly, the component trailing a tail to the positive direction is created by the resolved point sources. Our present purpose is to determin the peak position created by the first and the second components, eliminating the third component.

Therefore, we fitted the histogram in the range of 0.55–2.0 with a function:

$$f(x) = N_1 \exp\Big(-\frac{(x-\mu)^2}{2\sigma_1^2}\Big) + N_2 \exp\Big(-\frac{(1-\mu/x)^2}{2\sigma_2^2}\Big). \tag{7.10}$$

This function is chosen for practical reasons that it successfully reproduces the shape of the distribution and that the peak position μ is clearly defined. Although pixels are not independent with each other due to the $ccf\left[B\right]$ operation, we tentatively put square root errors in each bin. From the fitting, we get $\mu = 0.882 \pm 0.001$, $\sigma_1 = 0.150 \pm 0.001$, and $\sigma_2 = 0.201 \pm 0.001$. Thus, we decided to fix $\alpha = 0.88$ to estimate B^{UCXB} in equation (7.6). This means that the 0.7–7.0 keV GIS flux from the entire LSS field is contributed by $\sim$ 12% by point sources which can be resolved with ASCA.

7.2.3 Point-source images

Now that α in equation (7.6) has been determined, we can substitute equation (7.6) into equation (7.8) and obtain $M^{FLAT}(SKYX, SKYY)$. We show M^{FLAT} of the LSS observations thus obtained with $\alpha = 0.88$ in figure 7.6, and its pixel-value distribution in figure 7.7. Just to remember, M^{FLAT} is our best estimate for the 0.7–7.0 keV point-source image for the LSS sky, after subtracting RNXB and UCXB. It is expressed in rather arbitrary scale, but pixel values are expected to be in proportion with the source

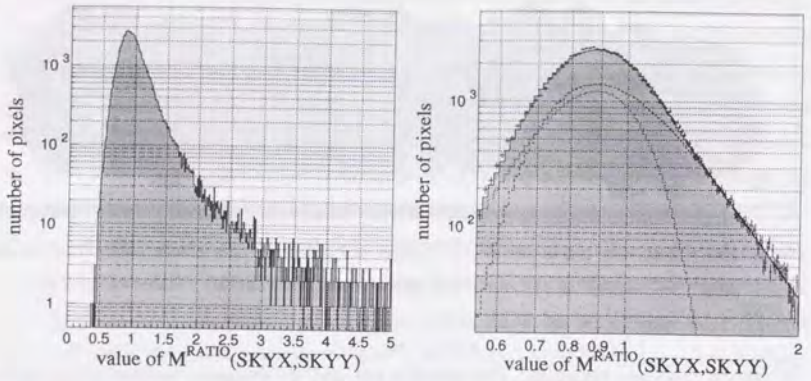

Figure 7.5: Distribution of pixel values in figure 7.4. Left panel shows the distribution in the range of 0–5, and right panel shows in the range of 0.55–2.0. In right panel, the distribution (crosses) is fitted with the function of equation (7.10) and the best fit line (solid line) and each component (two dashed lines) are overlaied.

flux. The distribution has a sharp peak at 0.0, which demonstrates the correctness of the RNXB and UCXB subtraction. Similar to the case of figure 7.5, the width of distribution in figure 7.7 represents the superposition of the statistical errors which depend on the deepness of the exposure, and the fluctuation of the CXB brightness due to confusion of faint sources. The long tail extending toward the positive direction is created by the point sources in the LSS fields.

We set a rather loose threshold of 0.1 to define point sources to be removed, in order to ensure the completeness of source detection even at the edge of the GIS f.o.v. This threshold roughly correspond to a few $\times 10^{-13}$ erg s^{-1} cm^{-2}, which we will discuss in the next section. Since the number of pixels below -0.1 and 0.0 is 486 and 49,925, respectively, we can estimate the probability of mistaking chance fluctuations for point sources is $\sim 1\%$, assuming that the distribution blow 0.0 is completely determined by the statistics and the CXB base level fluctuations, and that these effects are symmetric below and above 0.0. Moreover, if we fit the distribution with a Gaussian in the range of -0.04–0.0 fixing the peak position to 0.0, the fit gives $\sigma = 0.018$, which is $\sim 1/5$ of the proposed threshold. Therefore, in most regions where exposure is much deeper than the image edge (typically ~ 20 ks), the probability of chance detection of false sources is expected to be much less.

We remark here again that the point-source map M^{FLAT} has been smoothed with the $ccf[B]$ operation according to equation (7.8), so that the map has a typical coherence

length comparable to the PSF width ($\sim 3'$). Accordingly, a point source detection cannot occur in a single pixel, unless it is very close to the threshold by chance.

Here, we explain how M^{RATIO} and M^{FLAT} are different, and whey we have to take this dual step, i.e. M^{RATIO} and M^{FLAT}, to produce the point-source-masks. As can be seen from equation (7.9), M^{RATIO} is optimized in such a way that the image of a uniform-brightness source (specifically, B^{UCXB}) appears flat; dividing by $B^{\overline{CXB}}$ is meant to normalize $B^{OBS} - B^{RNXB}$ to the effective XRT+GIS response (including vignetting and stray lights) for a uniform X-ray source. On the other hand, M^{FLAT}, as given in equation (7.8), is constructed in such a way that the pixel intensity for each point source is directly proportional (except for spectral differences) to the incident source flux. This has been achieved by dividing $B^{OBS} - B^{RNXB} - B^{UCXB}$ by the factor A^{PS}, which gives the effective area of the XRT. Since this normalization factor does not make the CXB image appear flat, B^{UCXB} must be evaluated in advance using M^{RATIO}, and subtracted from B^{OBS} when calculating M^{FLAT}.

Figure 7.6: Gray scale image of $M^{FLAT}(SKYX, SKYY)$ for the entire LSS observations. White pixel corresponds to -0.1 and black pixel corresponds to 0.4.

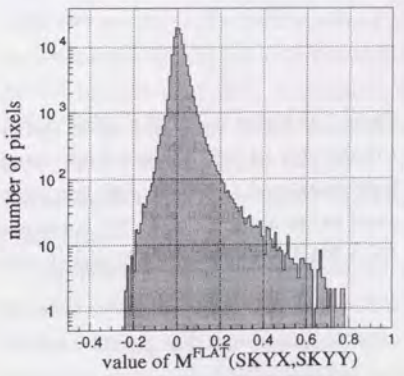

Figure 7.7:
Distribution of pixel values in figure 7.6.

7.2.4 Source-masking

In order to remove the point sources thus detected, we decided to mask the regions centered on the point sources within an *appropreate* radius depending on the source flux, because a brighter source affects a wider region around it than a fainter source. To do this, we have created the sky coordinate images called source-mask which is utilized to mask out the point sources. In the source-mask, the pixels to be removed is set to 1.0, whereas other pixels are set to 0.0. We then generate the CXB spectra and responses without point sources, in reference to the source-masks.

It is an important issue how to set the *appropreate* radius for each point source. Since our aim is to study the properties of the CXB without point sources brighter than a certain level, we have chosen the mask radius to be r_{mask} where surface brightness B_i^{PS} created by the i-th point source gets less than 3% of the unresolved CXB (B^{UCXB}). figure 7.8 shows an example of the azimuthally averaged XRT+GIS PSF. Although the XRT+GIS PSF has slight energy- and offset-angle-dependences (figure 4.2), they matter little for the present purpose. The observed radial profile of the PSF can be roughly expressed by a double exponential, as seen in figure 7.8. Therefore, we have calculated the masking radius r_{mask} by a formula:

$$0.03 \times 116.5 \times \frac{N^{RAW}}{\alpha\, N^{\overline{CXB}}} = 528.5\ \exp(-0.96\, r_{mask}) + 4.95\ \exp(-0.16\, r_{mask}), \quad (7.11)$$

where N^{RAW} and $N^{\overline{CXB}}$ are the pixel values of M^{RAW} and $M^{\overline{CXB}}$ in equation (7.9), respectively, at $(SKYX, SKYY)$ where the point source was detected. We also set the minimum value of r_{mask} as 3 mm.

We have applied this masking for every pixel of M^{FLAT} that exceeds the threshold level of 0.1. As mentioned in the previous section, a point source detection usually occurs

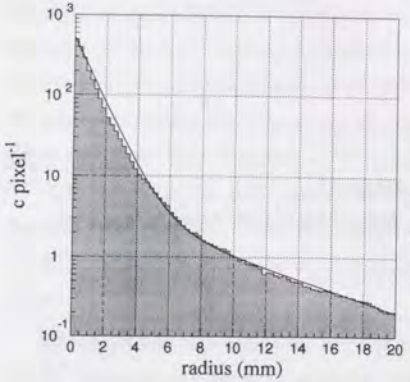

Figure 7.8: Radial profile of 8′ offset Cyg X-1 image taken by GIS2 in the 5–6 keV energy band (histogram). Smooth solid line superposed on the histogram shows the function of $f(x) = 528.5\ \exp(-0.96\, x) + 4.95\ \exp(-0.16\, x)$.

in a cluster of pixels, especially for the bright sources. Therefore, multiple masks are usually applied for a single image peak on M^{FLAT}, which is in most cases caused by a single point source. However, since the function for the PSF radial profile gets flatter as the radius gets larger, r_{mask} is expected to be the largest at the peak position among the single cluster of pixels that exceed the threshold level.

We show the source-mask for the LSS observations in figure 7.9. There are many masked regions near the edge of the image, which probably result partially from insufficient statistics. However, we utilize only the events inside 20 mm from the optical axis, so that most of these pixels are originally discarded from the spectral analyses.

Figure 7.9: The source-mask for the entire LSS observations. White and black pixels correspond to 0.0 and 1.0, respectively.

7.3 Threshold flux of the source-masks

We have set the threshold value at 0.1 on the M^{FLAT} map. However, the actual source flux corresponding to this level has remained uncertain. We therefore discuss the threshold flux level in this section.

We carried out the source-finding with the GIS image only in the 0.7–7.0 keV energy band, and as a result, the spectral information has been lost. Therefore, some assumptions on the spectral parameters are required when we attempt to convert the peak value on M^{FLAT} into the source flux. Fortunately, there is a point source-list available by Ueda (1996) in the LSS field. This LSS source-list contains all the point sources which have been detected with the ASCA GIS above 4σ significance, and detailed studies have been carried out in Ueda (1996). Source fluxes and errors in the list have been determined by image fitting.

The primary reason why we have not utilized the LSS source-list itself is that we also deal with fields other than LSS, so that we have to construct ourselves the method of source-finding and source-elimination in all the fields analyzed here. We, however, conducted our analyses in cooperation with Ueda and our source-finding method is a

modified version of his method. The major difference is that he searched point sources by the threshold significance, while we searched sources by the threshold flux and masked them out regardless of their significances. His method is optimized to study detected point sources, whereas our method is optimized to study the remaining CXB. We believe our method to eliminate point sources is one of the best choices for the purpose of studying the remaining CXB, over the different fields with different exposures. There is also a merit of utilizing the by-product images like M^{FLAT} and $M^{\overline{CXB}}$, which also provide us important information on the CXB. However, we have not determined the actual source fluxes nor source positions while creating the source-mask, as described in §7.2.4. We only masked out the pixels where the contribution of the bright point sources is likely to be large. On the other hand, Ueda has determined the source fluxes and source positions by the method of image fitting, after finding a point source candidate. In the image fitting, he left the CXB base level free, so that there was some risk of the base level being affected by the point sources in the f.o.v. He also determined the photon index of the detected point source through spectral fitting in five energy bands, although it has a large error. Therefore, below we compare our source-finding results with the Ueda's source-list.

In figure 7.10, we plot the pixel value of our $M^{FLAT}(SKYX, SKYY)$ at each source position against the source flux in the 2–10 keV energy band, for all 72 sources in the LSS source-list. The source position and the 2–10 keV flux have both been taken from Ueda (1996). In left panel where all sources are assumed to have a spectrum of $\Gamma = 1.7$, we

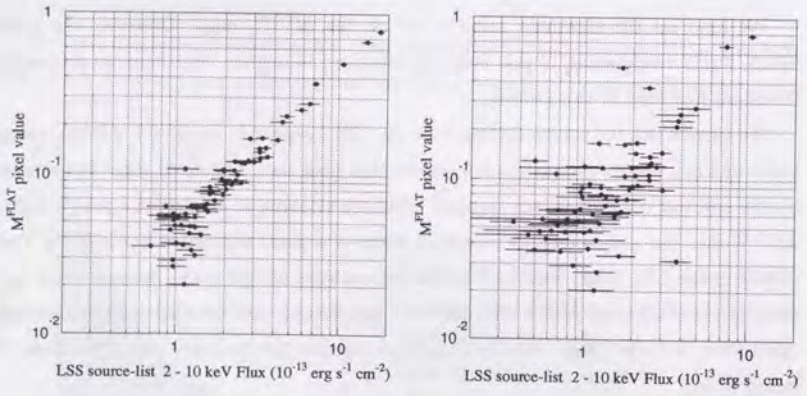

Figure 7.10: Correlation between the source flux in the 2–10 keV energy band listed by Ueda (1996) vs. the pixel value of $M^{FLAT}(SKYX, SKYY)$ from our analysis at each source position. The source-list flux plotted on left panel assumes $\Gamma = 1.7$. On right panel, photon index is derived from the five-energy-band spectrum fitting by Ueda (1996).

can see M^{FLAT} to be in good proportion with the source flux. The threshold level of 0.1 thus corresponds to 2–2.5 $\times$ 10^{-13} erg s^{-1} cm^{-2}. If we assume $\Gamma = 1.4$, the source flux should be multiplied by 1.27, so that the threshold flux increases. However, in right panel where photon index of each source is derived from the five energy band spectrum fitting by Ueda (1996), the correlation becomes rather scattered. This means that it is not easy to clearly state the threshold flux. In the following, we quote $\sim 2 \times 10^{-13}$ erg s^{-1} cm^{-2} as a typical threshold. As for the properties of the detected point sources in the LSS field, Ueda (1996) may be referred to.

7.4 CXB properties of individual fields

7.4.1 Strategy to study individual fields

In §7.2, we have developed a method of eliminating point sources using the whole LSS field as an example, and conformed in §7.3 that this method gives a reasonably well-defined flux threshold in comparison with the more direct flux determination by Ueda (1996). We are now ready to apply the same method to all our sample fields, to carry out field-to-field comparisons of the CXB properties.

This can in practice be done in dual ways. On one hand, we can determine the value of α in equation (7.6) for each field in the same way as has been done for the LSS field in §7.2.2. This will give us information as to how the "CXB base level" varies from field to field. On the other hand, we can derive the spectrum of the unresolved CXB, after applying the source-maskings, for each field. This allows us to evaluate the CXB normalization and slope of each field, and to perform comparison among the sample fields. These two methods should lead to the same conclusion, since they are not independent from each other, but we think it is important to confirm the consistensy between them. Therefore, in §7.4.2, we study the CXB base level as indicated by α, while we take the other direction in §7.4.3. We compare, and further examine, these results in §7.4.5.

7.4.2 Field-to-field variation of the CXB base level

We derived α for each sample field, just in the same way as we evaluate α for the whole LSS field. In calculating M^{RATIO} with equation (7.9) for each field, we used the same B^{UCXB} as derived from the LSS data, because it provides the best-quality CXB template. We summarize the fitting results in table 7.2. The reason why σ_1 shows a smaller value in QSF3 than other fields is that the distribution was expressed almost only by the second term of equation (7.11), so that the value of σ_1 was effectively unconstrained. As mentioned in §7.2.2, the width of the distribution is determined mainly by the Poisson

Table 7.2: Fitting results of M^{RATIO} pixel values distribution for each sample field

ID	Name	$\alpha^\dagger$	$\sigma_1^\dagger$	$\sigma_2^\dagger$
1	SA57	0.910 ± 0.006	0.121 ± 0.006	0.156 ± 0.008
2	a-LSS	0.875 ± 0.005	0.149 ± 0.004	0.174 ± 0.008
3	b-LSS	0.855 ± 0.004	0.090 ± 0.010	0.173 ± 0.003
4	c-LSS	0.871 ± 0.006	0.164 ± 0.011	0.186 ± 0.005
5	d-LSS	0.917 ± 0.008	0.163 ± 0.014	0.220 ± 0.007
6	Draco	0.837 ± 0.010	0.153 ± 0.007	0.171 ± 0.014
7	NEP	0.889 ± 0.006	0.099 ± 0.011	0.170 ± 0.006
8	QSF3	0.876 ± 0.004	0.029 ± 0.030	0.130 ± 0.003
9	ZSYS	0.890 ± 0.005	0.136 ± 0.006	0.178 ± 0.005
10	BF	0.908 ± 0.005	0.090 ± 0.016	0.184 ± 0.003
11	Jupitar	0.862 ± 0.010	0.097 ± 0.008	0.165 ± 0.004
12	Arp 220	0.865 ± 0.010	0.183 ± 0.055	0.160 ± 0.004
13	3C368	0.990 ± 0.011	0.087 ± 0.006	0.126 ± 0.003

† The best fit value and 90% confidence level fitting error.

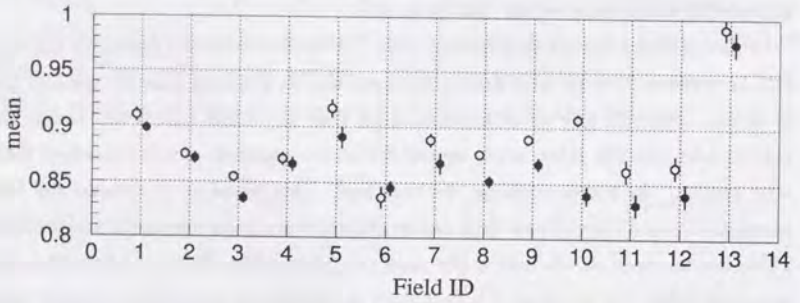

Figure 7.11: CXB base levels (= α) in the 0.7–7.0 keV energy band (open circles), plotted against the field ID. Error bars represent 90% confidence levels. Filed circles represent the results after the point sources have once been excluded at the threshold of 0.1 on M^{FLAT}, and M^{RATIO} was calculated again on the remaining region.

error and the CXB fluctuation due to the unresolved sources. Since σ_1 and σ_2 in each sample field show similar values with those in LSS, we can say that the statistics of these sample fields are comparable or better than that in the LSS field.

In figure 7.11, we plot the value of α in each field againt the field ID. For reference, we once again calculated M^{RATIO} of equation (7.9) and re-determined α, using images in which the point sources have been masked out at the threshold of 0.1 on M^{FLAT}. The

values of α thus derived from this "second iteration" are shown in figure 7.11 as filled circles. Except the Braccesi Field (ID = 10) where bright sources appear to be abundant, these values of α is not very much different from the original values of α (table 7.2; open circles in figure 7.11) determined by the "first iteration"; the rms difference between two sets of α is only 0.0011. This demonstrates that α is a well defined quantity for each ASCA field analyzed here, and can be confidently identified with the brightness of the unresolved CXB (i.e. CXB "base level"). At the same time, we confirm that our process of the source-finding and source-elimination converges in a single iteration.

In the 3C368 field, α shows apparently a larger value of ~ 1.0. This is probably due to the large soft-excess of the CXB spectrum in this particular field, combined with our method using the single-band brightness. In fact, if we use the 2.0–7.0 keV energy band image instead of the 0.7–7.0 keV image, α in the 3C368 field decreases to 0.90, although statistics gets much worse. Although the Arp 220 field have shown comparable soft-excess with the 3C368 field in §7.1, α in the Arp 220 field is not so large. This suggests that the soft-excess seen in the Arp 220 field is partly due to the Arp 220 itself.

The mean value and standard deviation of α is 0.883 ± 0.025 for the data which have not been processed through the source-maskings (table 7.2). If we remove the data ID = 11–13, α gets 0.881 ± 0.020. Applying the source-maskings and making the second iteration, α becomes 0.864 ± 0.021. This fact implies that the CXB intensity is isotropic by $\sim 2\%$ rms at the 1–2 deg^2 scale, if $\sim 12\%$ of the CXB is resolved by ASCA. Then, could the field-to-field differences of the CXB base level α cause the wrong estimation of the point source fluxes on M^{FLAT}? The 5% difference of the CXB base level α affects the pixel value of M^{FLAT} by ~ 0.002 at the optical axis and by ~ 0.004 at the radius of 20 mm. These are much less compared with the threshold level of 0.1. Therefore, we conclude that the field-to-field variation of the CXB base level does not affect the source-maskings.

As the end of this subsection, we mention whether field-to-field variation of α is significant or not. If we adopt the 1σ error given in table 7.2, χ^2/d.o.f = 144/9 for ID = 1–10, and the variation appears significant. However, as described in §6.4.5, there is the $\sim 3\%$ systematic error for the relative CXB intensity due mainly to the RNXB subtraction. Considering this issue, $\sim 2\%$ variation of α is not significant.

7.4.3 CXB spectra of individual fields excluding point sources

We next examine the second way of comparing the field-to-field CXB properties, i.e. deriving the spectrum of the unresolved CXB after applying the source-maskings. We again made the CXB spectrum of each field, this time masking point sources out by pro-

cessing the data through the source-masking. We show all the source-masks in appendix C together with the flat-field images M^{FLAT}. The ARFs are also re-created considering the decrease of the integration area on the detector due to the source-maskings. Then we fitted each spectrum individually as we have done in §7.1. The fitting results are summarized in table 7.3. We also show all the spectra in appendix D, together with the best-fit models.

Table 7.3: ($PL^{\rm hard}$+$PL^{\rm soft}$) fits to the 0.6–10 keV spectrum of each field masking point sources at the threshold of 0.1 on M^{FLAT}. All errors are 90% confidence level. $\Gamma^{\rm soft}$ is fixed to 6.0.

ID	Name	Exp.†	Area‡	$N_{\rm H}^{\sharp}$	χ^2/d.o.f	$\Gamma^{\rm hard}$	$F_{\rm X}^{\rm hard\triangleleft}$	$F_{\rm X}^{\rm soft\star}$
1	SA57	461,343	0.59	1.0	70.5/67	1.378 ± 0.019	5.83 ± 0.09	1.33 ± 0.15
2	a-LSS	119,221	1.73	1.1	96.2/67	1.459 ± 0.036	5.61 ± 0.17	0.76 ± 0.29
3	b-LSS	130,206	1.78	1.1	71.7/67	1.441 ± 0.035	5.83 ± 0.17	1.19 ± 0.30
4	c-LSS	138,641	1.88	1.1	66.8/67	1.458 ± 0.035	5.57 ± 0.16	1.26 ± 0.28
5	d-LSS	127,324	1.29	1.1	55.1/67	1.485 ± 0.045	5.64 ± 0.21	0.96 ± 0.37
6	Draco	57,002	0.63	4.1	86.4/67	1.473 ± 0.052	5.32 ± 0.23	1.53 ± 0.40
7	NEP	118,434	0.41	4.2	73.1/67	1.393 ± 0.042	5.50 ± 0.19	1.78 ± 0.30
8	QSF3	60,157	0.33	1.7	46.4/67	1.393 ± 0.050	6.31 ± 0.26	1.25 ± 0.42
9	ZSYS	109,893	1.16	2.3	26.8/67	1.500 ± 0.043	5.56 ± 0.20	0.68 ± 0.35
10	BF	114,738	0.82	1.2	102.5/67	1.546 ± 0.041	5.60 ± 0.20	0.13 ± 0.25
11	Jupiter	20,389	0.28	2.1	70.9/67	1.576 ± 0.097	4.98 ± 0.39	1.06 ± 0.77
12	Arp 220	23,039	0.37	4.2	72.0/67	1.377 ± 0.078	5.75 ± 0.36	5.00 ± 0.68
13	3C368	19,934	0.33	9.8	92.2/67	1.480 ± 0.082	6.14 ± 0.40	4.92 ± 0.76

† Total exposure time (s).

‡ Integration area (deg^2) on the sky after applying the source-maskings (threshold 0.1).

♯ Absorption for $PL^{\rm hard}$ (10^{20} cm^{-2}) from Einstein On-line Service (*EINLINE*). Fixed while fitting.

◁ Flux of $PL^{\rm hard}$ (10^{-8} erg s^{-1} cm^{-2} str^{-1}) in the 2–10 keV energy band.

⋆ Flux of $PL^{\rm soft}$ (10^{-8} erg s^{-1} cm^{-2} str^{-1}) in the 0.5–2 keV energy band.

Except the Braccesi Field, the $PL^{\rm hard} + PL^{\rm soft}$ models are accepted at the 99% confidence level. Particularly the fit to the NEP spectrum has been improved. To clearly show the difference of each parameter, we plot $\Gamma^{\rm hard}$, $F_{\rm X}^{\rm hard}$, and $F_{\rm X}^{\rm soft}$ against the field ID in figure 7.12 in comparison with the results obtained in §7.1 without eliminating point sources. We also plot these parameters when very strict source-maskings at the threshold of 0.06 (appendix E) were applied. In most fields except the d-LSS and NEP field, $\Gamma^{\rm hard}$ did not change significantly by applying the source-maskings. $F_{\rm X}^{\rm hard}$ decreased according to the masked sources, and the variation has become smaller. We will discuss in detail this field-to-field variation of the CXB parameters in the following subsections.

When the source-maskings are applied, the systematic error of the XRT effective area mentioned in §6.4.4 become more influencial, because the ARF response utilized for the spectrum fitting was generated individually for each field. Therefore, we tried fitting each spectrum with the modified XRT response as described in §6.4.4. However, fitting results did not change significantly, and we thus concluded that the systematic error of the XRT effective area was not severe at the threshold of 0.1.

7.4.4 Field-to-field variation of $\Gamma^{\rm hard}$

Firstly, we examine the variation of $\Gamma^{\rm hard}$. As seen in figure 7.12, $\Gamma^{\rm hard}$ of each field does not change significantly by applying the source-mask except NEP. This means that

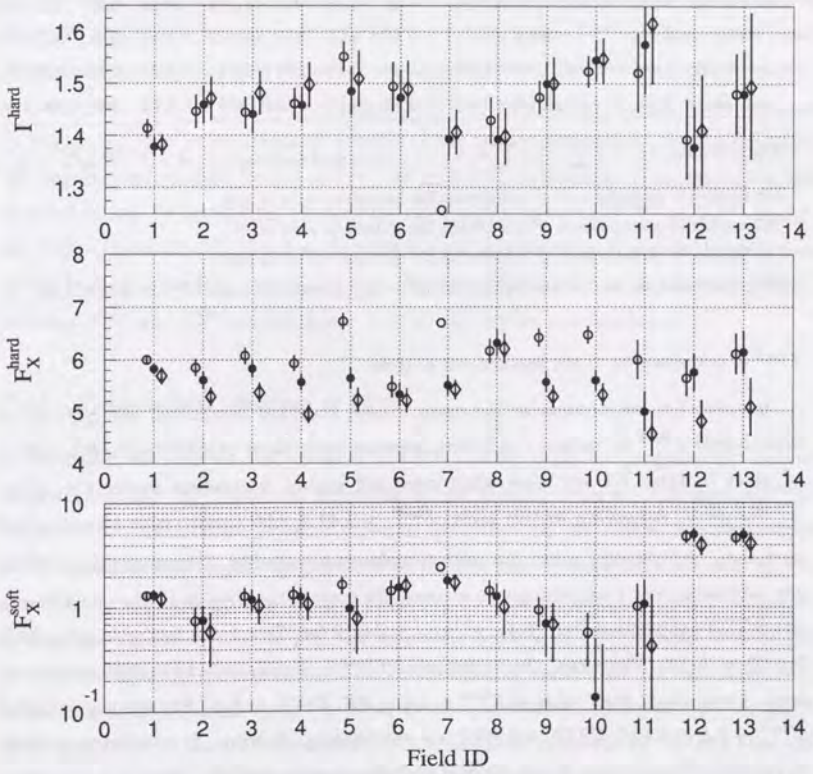

Figure 7.12: $\Gamma^{\rm hard}$, $F_{\rm X}^{\rm hard}$ (2–10 keV), and $F_{\rm X}^{\rm soft}$ (0.5–2 keV) of table 7.1 (no source-masking; open circles), table 7.1 (threshold 0.1; filled circles), and table E.1 (threshold 0.06; diamonds), plotted against the field ID. Error bars represent 90% confidence level.

Table 7.4: Mean values and standard deviations of $\Gamma^{\rm hard}$, $F_{\rm X}^{\rm hard}$, and $F_{\rm X}^{\rm soft}$.

Source Mask	ID	$\Gamma^{\rm hard}$ $\mu^\dagger$	$\sigma^\ddagger$	χ^2/d.o.f$^\triangleleft$	$F_{\rm X}^{\rm hard}$ $\mu^\dagger$	$\sigma^\ddagger$	χ^2/d.o.f*	$F_{\rm X}^{\rm soft}$ $\mu^\dagger$	$\sigma^\ddagger$	χ^2/d.o.f*
None$^\sharp$	1–13	1.461	0.047	185 (21)/11	6.10	0.30	291 (34)/11	1.30	0.66	473 (440)/11
		1.44	—— fixed ——		6.10	0.42	1924 (57)/10	1.42	0.69	777 (658)/10
	1–10	1.461	0.047	175 (16)/8	6.11	0.30	277 (29)/8	1.20	0.29	88 (71)/8
		1.44	—— fixed ——		6.11	0.42	1821 (42)/7	1.32	0.40	246 (176)/7
0.10	1–13	1.435	0.055	188 (34)/12	5.69	0.22	132 (31)/12	1.20	0.78	611 (553)/12
		1.44	—— fixed ——		5.67	0.21	436 (29)/12	1.24	0.67	685 (621)/12
	1–10	1.434	0.053	166 (23)/9	5.70	0.19	98 (16)/9	1.10	0.45	197 (154)/9
		1.44	—— fixed ——		5.67	0.19	367 (17)/9	1.12	0.25	91 (70)/9
0.06	1–13	1.443	0.060	185 (33)/12	5.41	0.31	241 (48)/12	0.98	0.65	399 (339)/12
		1.44	—— fixed ——		5.43	0.20	358 (40)/12	1.12	0.51	355 (314)/12
	1–10	1.442	0.058	168 (24)/9	5.44	0.29	191 (28)/9	0.94	0.50	228 (172)/9
		1.44	—— fixed ——		5.45	0.17	258 (17)/9	1.06	0.31	124 (97)/9

† Weighted mean, i.e., $\mu = \sum_i \frac{y_i}{\sigma_i^2} / \sum_i \sigma_i^{-2}$. ‡ Standard deviation, i.e., $\sigma^2 = \sum_i \frac{(y_i-\mu)^2}{\sigma_i^2} / \sum_i \sigma_i^{-2}$.

$^\triangleleft$ The number in parentheses is χ^2 considering the systematic error of 0.03.

* The number in parentheses is χ^2 considering the systematic error of 3%.

* The number in parentheses is χ^2 considering the systematic error of 0.05.

$^\sharp$ NEP is excluded due to the inappropriate fit. BF is further excluded when $\Gamma^{\rm hard}$ is fixed to 1.44.

$\Gamma^{\rm hard}$ is not sensitive to the masked-out sources.

In table 7.4, we summarize the mean values, standard deviations, and χ^2/d.o.f of field-to-field $\Gamma^{\rm hard}$ in various conditions, together with those of $F_{\rm X}^{\rm hard}$ and $F_{\rm X}^{\rm soft}$. These χ^2 given in table 7.4 are those when examined against a constant model, i.e., $\chi^2 = \sum_i \frac{(y_i-\mu)^2}{\sigma_i^2}$. According to this table, $\Gamma^{\rm hard} \sim 1.44 \pm 0.06$ (mean value and standard deviation, respectively), when the source-maskings are applied. The nominal χ^2 values are very large, and even taking into account the systematic error of $\Gamma^{\rm hard} \sim 0.03$ due to the RNXB subtraction (ref. §6.4), χ^2/d.o.f = 34/12 for ID = 1–13, and χ^2/d.o.f = 23/9 for ID = 1–10. Therefore, the variation of $\Gamma^{\rm hard}$ is significant at the 99% confidence level. Particularly, high value of $\Gamma^{\rm hard} \sim 1.5$ in BF, ZSYS, and d-LSS, and low values of $\Gamma^{\rm hard} \sim 1.4$ in SA57, QSF3, and NEP are outstanding. However, it is a little too hasty to conclude that we have found the field-to-field variation of $\Gamma^{\rm hard}$. There is a possibility that other systematic errors, such as that of the XRT effective area, are causing the $\Gamma^{\rm hard}$ variation, although χ^2 decrease only by ~ 1.0 with the modified XRT response (ref. §6.4.4). It is also possible that the source-eliminations are imperfect, even though

we have strictly masked out point sources by 3% level (ref. §7.2.4), and $\Gamma^{\rm hard}$ is rather insensitive to the process of source-masking, as mentioned above. One particular concern is that in BF, ZSYS, and d-LSS, where $\Gamma^{\rm hard}$ are high and the decreases in $F_{\rm X}^{\rm hard}$ by applying the source-maskings are large, most of masked-out bright sources are softer than the average CXB (ref. appendix F), whereas in NEP, where $\Gamma^{\rm hard}$ is low and the decrease in $F_{\rm X}^{\rm hard}$ is large, there exists NGC 6552 which has a very hard spectrum. Considering these issues, we conservatively state that the field-to-field variation of $\Gamma^{\rm hard}$ by ± 0.06 is marginal.

We next investigate the correlation between $\Gamma^{\rm hard}$ and $F_{\rm X}^{\rm hard}$. In figure 7.13, we plot $F_{\rm X}^{\rm hard}$ against $\Gamma^{\rm hard}$, for three levels of the source-maskings. There appears to exist a positive correlation for (a), while there appear to exist negative correlations for (b) and (c), although all three are at the marginal levels. The possible positive correlation seen in figure 7.13 (a) is due mainly to BF, ZSYS, and d-LSS, where $\Gamma^{\rm hard}$ are high (steep) and there exist very bright, softer sources as mentioned above. Therefore the positive correlation suggested in (a) is a natural consequence of the field selection, and its disappearance in (b) and (c) can be explained as a result of the source-elimination. On the contrary, the negative correlations for (b) and (c) are explained to originate as an artifact of the spectral fitting. In figure 7.14, we show the confidence contours of $\Gamma^{\rm hard}$ vs. $F_{\rm X}^{\rm hard}$ for figure 7.13b (threshold 0.1). The best fit value of each field is scattered in a similar direction as the individual confidence contours are elongated. Therefore, the possible correlations between $\Gamma^{\rm hard}$ and $F_{\rm X}^{\rm hard}$ seen in figure 7.13 (b) and (c) are not significant.

7.4.5 Field-to-field variation of $F_{\rm X}^{\rm hard}$

Secondly, we examine the variation of $F_{\rm X}^{\rm hard}$. As we apply the progressively severer source-maskings. $F_{\rm X}^{\rm hard}$ decrease according to the masked sources. Although $F^{\rm hard}$ is corrected for the decrease in the integration area through the ARFs, the decrease of $F_{\rm X}^{\rm hard}$ should be still roughly proportional to the decrease of the integration area on the sky, because the masked area contains point sources and the area is larger if the source is brighter. In figure 7.15, we plot the remaining fraction of $F_{\rm X}^{\rm hard}$ against that of the integration area. As we expected, there is an apparent correlation between these two, which indicates that point sources have surely been eliminated. Although $F_{\rm X}^{\rm hard}$ in QSF3 is little affected by the source-maskings, this is probably explained by the fact that the masked-out sources in QSF3 (the brightest one is identified as a star with $kT \sim 0.9$ keV in Chen et al. 1995; ref. §5.2.5) have considerably soft spectra, so that elimination of those sources have reduced only $F_{\rm X}^{\rm soft}$.

By applying the source-maskings at the threshold of 0.1 on M^{FLAT}, the mean value

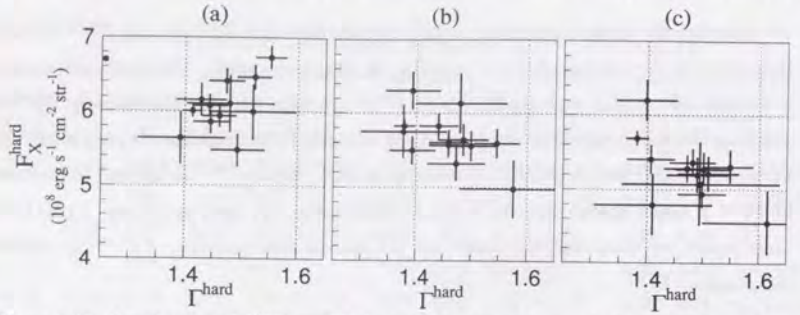

Figure 7.13: Correlations of $\Gamma^{\rm hard}$ vs. $F_{\rm X}^{\rm hard}$ (2–10 keV) in each sample field for (a) no source-masking, (b) after processed through the source-maskings at the threshold of 0.1, and (c) after processed through the source-maskings at the threshold of 0.06. Error bars represent the 90% confidence levels independently derived for $\Gamma^{\rm hard}$ and $F_{\rm X}^{\rm hard}$.

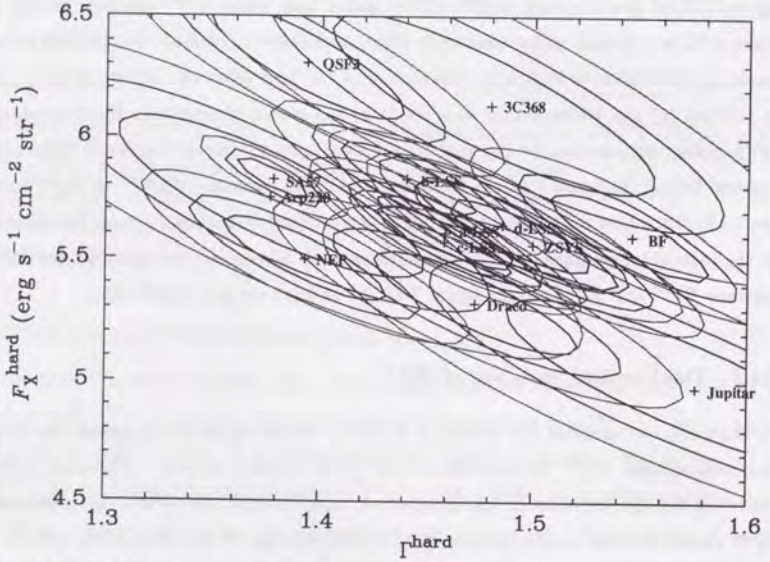

Figure 7.14: Confidence contours of $\Gamma^{\rm hard}$ vs. $F_{\rm X}^{\rm hard}$, in each sample field after processed through the source-masking at the threshold of 0.1. Contours (from inner to outer) represent 68, 90 and 99% confidence levels. Crosses show the best fit position in the labeled fields.

and standard deviation of $F_{\rm X}^{\rm hard}$ have become $(5.69 \pm 0.22) \times 10^{-8}$ erg s^{-1} cm^{-2} str^{-1}, as given in table 7.4. If we remove the data ID = 11–13, $F_{\rm X}^{\rm hard}$ gets $(5.70 \pm 0.19) \times 10^{-8}$ erg s^{-1} cm^{-2} str^{-1}. Thus the field-to-field relative 1σ variation of $F_{\rm X}^{\rm hard}$ is reduced to 3.4%, at the level where ~ 7% of the CXB is resolved into discrete sources. If we further reduce the threshold down to 0.06, the standard deviation of $F_{\rm X}^{\rm hard}$ again increased to

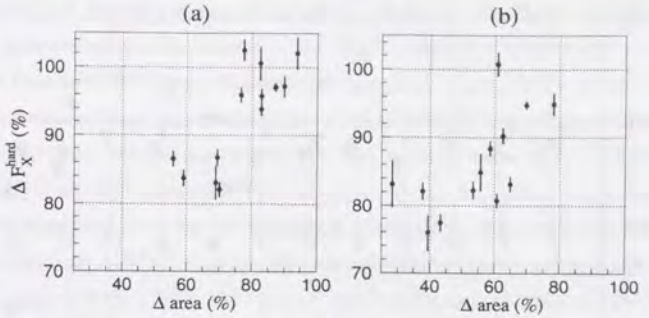

Figure 7.15: The remaining fraction (%) of $F_{\rm X}^{\rm hard}$ plotted against the remaining fraction (%) of the integration area on the sky in each sample field, for (a) after processed through the source-maskings at the threshold of 0.1 and (b) at the threshold of 0.06. Both (a) and (b) are relative ratios to those with no source-masking.

0.29×10^{-8} erg s^{-1} cm^{-2} str^{-1}. However, this is due partly to the increase of the systematic and statistical errors, which makes it difficult to determine accurate value of $\Gamma^{\rm hard}$. The threshold level of 0.06 is rather too strict especially in low exposure fields, and more than half the integration areas are lost in such fields. As a result, the effect of the systematic error in the XRT effective area, as well as the statistical errors, have become severer. Since the field-to-field variation of $\Gamma^{\rm hard}$ is marginal as described in the previous section, we fixed $\Gamma^{\rm hard}$ to 1.44 in order to reduce the effect of the systematic and statistical errors. We show the fitting results in figure 7.16. By fixing $\Gamma^{\rm hard}$, the field-to-field variation is reduced to 0.17×10^{-8} erg s^{-1} cm^{-2} str^{-1} at the threshold of 0.06, which supports our considerations above.

Taking into account the systematic error of 3% (ref. §6.4.5), we obtain χ^2/d.o.f = 31/12 for ID = 1–13, and χ^2/d.o.f = 16/9 for ID = 1–10. Therefore, the assumption of constant $F_{\rm X}^{\rm hard}$ is acceptable at the 95% confidence level for the latter case. However, there must exist the field-to-field variation of $F_{\rm X}^{\rm hard}$ due to statistical fluctuations of the number of faint unresolved sources in the f.o.v. (§2.2), as far as the CXB is significantly contributed by a superposition of faint point sources. We will discuss this fluctuation level in chapter 8.

On the other hand, we may utilize the observed ± 3.4% rms relative variation in $F_{\rm X}^{\rm hard}$ to evaluate the maximum allowed fluctuation in the CXB brightness. Let I_0 be the average 0.7–10 keV CXB brightness, and δI be its intrinsic rms fluctuation on the angular scale of $\sim 1°$. Then, at the 90% confidence level, we can reject the possibility that our 10 sample fields are derived from population with $\delta I / I_0 > 0.092$. In other words, the intrinsic rms fluctuation of the 0.7–10 keV CXB brightness should be less than 9.2% of I_0 on the $\sim 1°$

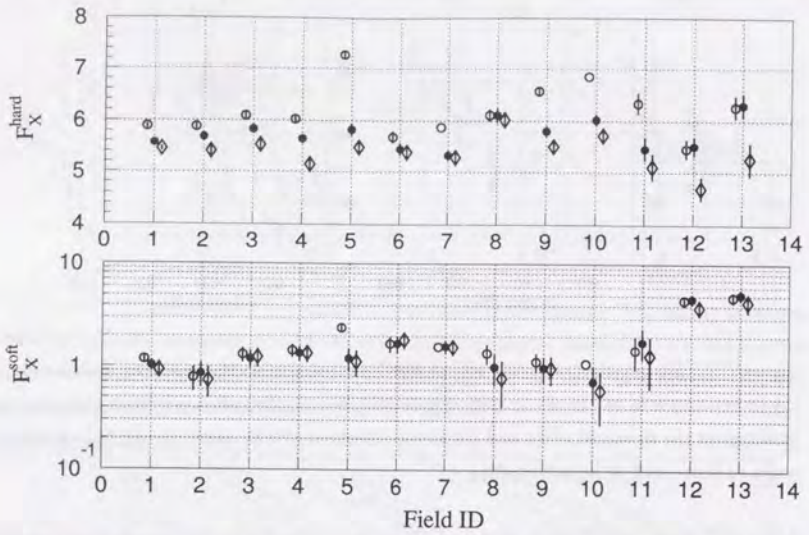

Figure 7.16: Same as middle and lower panels in figure 7.12, but $\Gamma^{\rm hard}$ are fixed to 1.44.

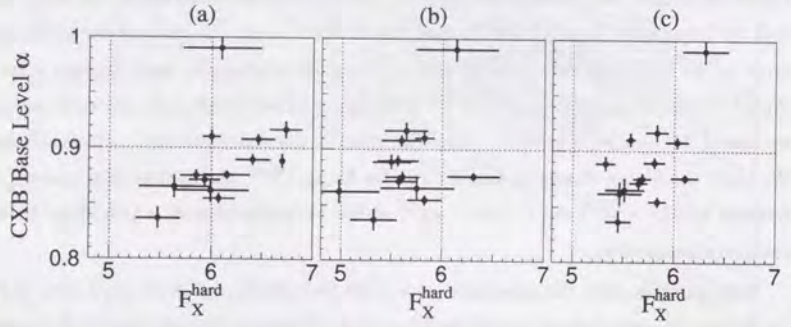

Figure 7.17: The CXB base level α without the source-maskings, plotted against $F_{\rm X}^{\rm hard}$ for (a) no source-masking with $\Gamma^{\rm hard}$ left free, (b) after processed through the source-maskings at the threshold of 0.1 with $\Gamma^{\rm hard}$ left free, and (c) after processed through the source-maskings at the threshold of 0.1 with $\Gamma^{\rm hard}$ fixed to 1.44. Error bars represent the 90% confidence levels independently derived for α and $F_{\rm X}^{\rm hard}$.

angular scale, when we remove discrete X-ray sources with 2–10 keV fluxes exceeding $\sim 2 \times 10^{-13}$ erg s^{-1} cm^{-2}.

As described in §7.4.1, it is also important to confirm the consistensy between $F_{\rm X}^{\rm hard}$ and α in equation (7.6) as the CXB base level. We therefore plotted α of each sample

field against $F_{\rm X}^{\rm hard}$ derived under several conditions in figure 7.17. There certainly appears to exist a positive correlation between α and $F_{\rm X}^{\rm hard}$, although it is not definite since the variations themselves of these parameters are marginal. Again, QSF3 occupies a little peculiar positions in these correlations; it has a large $F_{\rm X}^{\rm hard}$ of $\sim 6 \times 10^{-8}$ erg s^{-1} cm^{-2} str^{-1} even after processed through the source-maskings, while its value of $\alpha = 0.88$ is not so high. This is probably because $F^{\rm hard}$ put more weights on the regions where exposure is deep due to vignetting or overlap of the multiple observations, whereas α essentially deals with every pixel on M^{RATIO} equally. We point out that there appear to exist three or four point sources with $\sim 0.5 \times 10^{-13}$ erg s^{-1} cm^{-2} in the central region of QSF3, which have not been masked out by the source-maskings.

7.4.6 Effects of the soft component

Lastly, we examin the variation of $F_{\rm X}^{soft}$ and its possible effect on the hard component. The field-to-field variation of $F_{\rm X}^{\rm soft}$ is quite significant, even though considering the systematic errors. Particularly, the soft-excess in the Arp 220 and 3C368 fields is evident. As described in §7.4.2, the soft-excess in the Arp 220 field can be partly due to the Arp 220 itself, but the soft-excess still remains after processed through the source-masking at the threshold of 0.06, where Arp 220 is masked out. Even excluding ID = 11–13 (Jupiter, Arp 220, and 3C368), χ^2/d.o.f shows huge value and the field-to-field variation of $F_{\rm X}^{\rm soft}$ is still significant, which suggests that the soft component of the CXB is in large part of the Galactic origin. There also appear to exist a positive correlation between $F_{\rm X}^{\rm soft}$ and the absorption column $N_{\rm H}$. Including this, we will discuss the soft component in chapter 8. There is a possibility that the absorption to the hard component ($PL^{\rm hard}$) has artificially created the soft-excess. As described in §6.4.2, $F_{\rm X}^{\rm soft}$ is affected by a factor of ~ 1.6, if we change $N_{\rm H}$ by 4×10^{20} cm^{-2}. Therefore, we cannot reject the possibility that the mis-estimations of $N_{\rm H}$ have caused the field-to-field variability of $F_{\rm X}^{soft}$ for ID = 1–10, but at least the large soft-excesses in the Arp 220 and 3C368 fields are real.

As we apply the source-maskings, significant decreases of $F_{\rm X}^{\rm soft}$ were seen in d-LSS, QSF3, and BF. This is because there are bright soft sources in these fields, e.g. NGC 5098 in d-LSS and a star in QSF3, as already mentioned in preceding subsections. In the Braccesi Field, $F_{\rm X}^{\rm soft}$ is low, and consistent with 0.0 when source-maskings are applied. However, this is due partly to the large $\Gamma^{\rm hard} \sim 1.55$ in BF when $\Gamma^{\rm hard}$ is left free. As seen in figure 7.16, $F_{\rm X}^{\rm soft}$ is not so small if $\Gamma^{\rm hard}$ is fixed to 1.44, compared with that in figure 7.12. Therefore, $F_{\rm X}^{soft}$ is affected by the hard component to some considerable degree. Then, how about the opposite direction? Does mis-modeling of the soft component affects the fitting parameters of $PL^{\rm hard}$? This is probably negligible, we believe. As described

in §6.3, $\Gamma^{\rm hard}$ is affected only by ~ 0.015 whether we choose the power-law model or Raymond-Smith model as the soft component. The absorption column difference of $N_{\rm H} = 4 \times 10^{20}$ cm^{-2} affects $\Gamma^{\rm hard}$ by similar level, although it affects $F_{\rm X}^{\rm soft}$ by a factor 1.6. In figure 7.18, we plotted $F_{\rm X}^{\rm hard}$ against the parameters of $PL^{\rm hard}$. These distributions are scattered and particular correlations are not seen.

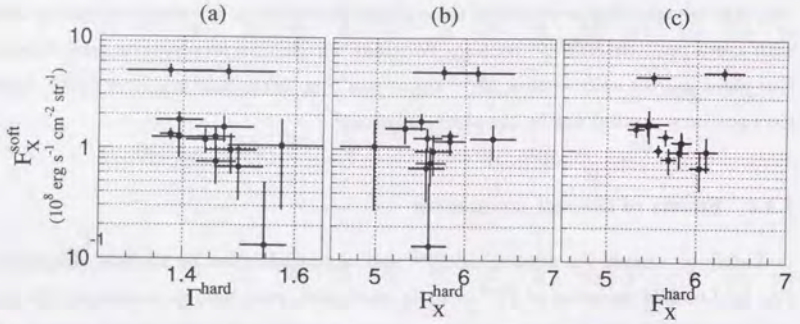

Figure 7.18: $F_{\rm X}^{\rm hard}$ of each sample field plotted against (a) $\Gamma^{\rm hard}$, (b) $F_{\rm X}^{\rm hard}$ with $\Gamma^{\rm hard}$ left free, and (c) $F_{\rm X}^{\rm hard}$ with $\Gamma^{\rm hard}$ fixed to 1.44. All of them are processed through the source-maskings at the threshold of 0.1. Error bars represent the 90% confidence levels independently derived for $F_{\rm X}^{\rm hard}$, $\Gamma^{\rm hard}$, and $F_{\rm X}^{\rm hard}$.

7.5 Average CXB spectra excluding point sources

In this section, we return to the average CXB spectrum of the whole LSS, and examine its behavior by applying the source-maskings. We also created the CXB spectrum of the best statistics (total CXB spectrum) by summing up the SA57, LSS, Draco, NEP, QSF3, ZSYS, and BF spectra, after processed through the source-maskings at the threshold of 0.1. However, this total CXB spectrum is quite biased to the SA57 field which have comparable exposure with the whole LSS. Therefore, we only utilize it to examine the possible spectral features in the CXB spectra. We also remark that the integration time of the total CXB (1,437 ks) has already exceeded that of the night-earth data (1,202 ks), which we utilize to estimate RNXB (ref. §4.4.4). Therefore, the statistical error of each spectrum bin in the total CXB spectrum is dominated by RNXB, especially in higher energy bands.

In table 7.5, we summarize the fitting results for the average CXB spectra of the

Table 7.5: ($PL^{\rm hard}$+$PL^{\rm soft}$) fits to the 0.6–10 keV spectrum of the total CXB (SA57+LSS+Draco+NEP+QSF3+ZSYS+BF) and the whole LSS. All errors represent 90% confidence levels.

Name	Mask$^{\diamond}$	Exp.†	Area‡	$\chi^{2\sharp}$	$\Gamma^{\rm hard}$	$F_{\rm X}^{\rm hard\triangleleft}$	$\Gamma^{\rm soft}$	$F_{\rm X}^{\rm soft\star}$
ALL*	0.10	1,436,959	9.19	104.7	1.439 ± 0.017	5.85 ± 0.07	6.3 ± 0.6	1.34 ± 0.23
				105.5	1.432 ± 0.013	5.86 ± 0.07	6.0 fix	1.23 ± 0.10
				106.6	1.44 fix	5.82 ± 0.03	6.0 fix	1.19 ± 0.08
LSS*	None	515,392	7.22	105.7	1.486 ± 0.021	6.14 ± 0.09	6.4 ± 0.8	1.40 ± 0.14
				106.5	1.479 ± 0.021	6.14 ± 0.02	6.0 fix	1.27 ± 0.14
				122.4	1.44 fix	6.33 ± 0.04	6.0 fix	1.49 ± 0.11
	0.10	515,392	5.24	102.0	1.465 ± 0.027	5.66 ± 0.10	6.5 ± 1.1	1.19 ± 0.16
				102.5	1.458 ± 0.020	5.68 ± 0.09	6.0 fix	1.06 ± 0.16
				104.7	1.44 fix	5.75 ± 0.05	6.0 fix	1.15 ± 0.12
	0.06	515,392	3.90	101.8	1.481 ± 0.039	5.22 ± 0.11	5.7 ± 1.5	0.84 ± 0.33
				101.9	1.486 ± 0.023	5.22 ± 0.10	6.0 fix	0.89 ± 0.18
				112.7	1.44 fix	5.39 ± 0.05	6.0 fix	1.11 ± 0.14

$^{\diamond}$ Source-masking threshold on M^{FLAT}.

† Total exposure time (s).

‡ Integration area (deg^2) on the sky.

$^{\sharp}$ Degrees of free are 100, 101, and 102, respectively, coresponding to the fixed parameters.

$^{\triangleleft}$ Flux of $PL^{\rm hard}$ (10^{-8} erg s^{-1} cm^{-2} str^{-1}) in the 2–10 keV energy band.

* Flux of $PL^{\rm soft}$ (10^{-8} erg s^{-1} cm^{-2} str^{-1}) in the 0.5–2 keV energy band.

* Absorption columns are fixed to 2.0×10^{20} cm^{-2} for ALL and 1.1×10^{20} cm^{-2} for LSS.

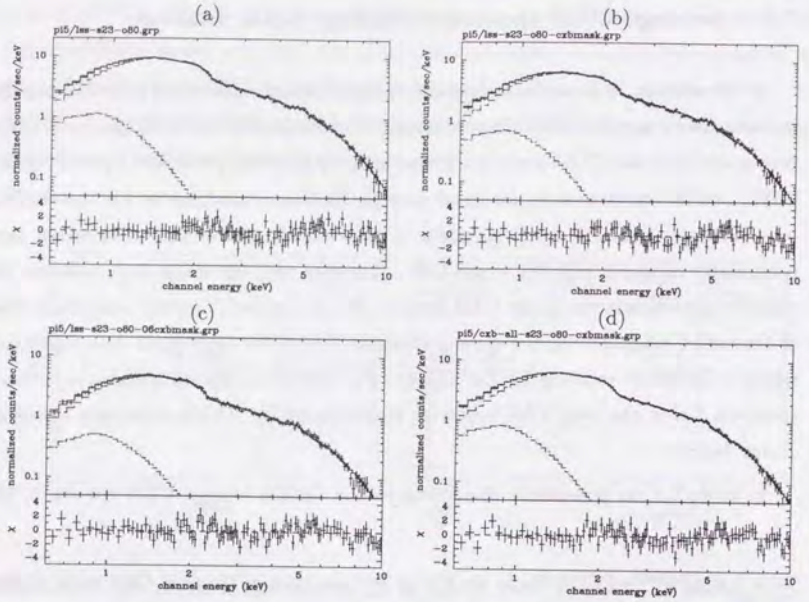

Figure 7.19: Average CXB spectra for (a) LSS with no source-masking, (b) LSS processed through source-masking at the threshold of 0.1, (c) LSS processed through source-masking at the threshold of 0.06, (d) ALL (SA57+LSS+Draco+NEP+QSF3+ZSYS+BF) processed through source-masking at the threshold of 0.10, fitted with the absorbed power-law model in the 0.6–10 keV energy band. The Galactic absorptions are fixed as given in table 7.5, and $\Gamma^{\rm soft}$ are left free. Upper panels show GIS2+3 spectrum (corosses) and the best fit model (solid line). Lower panels show residuals plotted in the unit of σ.

whole LSS at three levels of the source-maskings (no source-mask, threshold 1.0 and 0.06) under three fitting conditions (all free, $\Gamma^{soft} = 6.0$, and $\Gamma^{hard} = 1.44$), together with those of the total CXB spectrum. Each spectrum is shown in figure 7.5. All three models are acceptable for all three (LSS) plus one (ALL) spectra at the 90% confidence level. This indicates that the 0.7–10 keV spectral shape of the average CXB is little modified by the source-elimination brighter than $\sim 2 \times 10^{-13}$ erg s^{-1} cm^{-2} (2–10 keV). The resolved fractions of the CXB into discrete sources, i.e. decreasing fractions of $F_{\rm X}^{\rm hard}$, are 7.5% and 15% corresponding to the processed source-masking threshold of 0.10 and 0.06, respectively. In order to visualize the changes of $F_{\rm X}^{\rm hard}$, we plot the confidence contour of $\Gamma^{\rm hard}$ vs. $F_{\rm X}^{\rm hard}$ for each CXB spectrum on the same plane in figure 7.20. In chapter 8, we will discuss this fraction from the view of the log N-log S relation (ref. 2.3). The decreasing fractions of $F_{\rm X}^{\rm soft}$ are 23% and 24%, respectively. Although these fractions

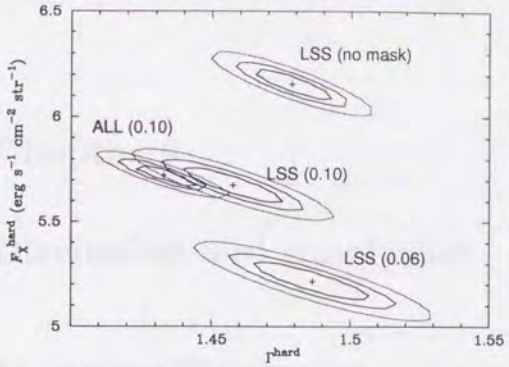

Figure 7.20: Confidence contour of $\Gamma^{\rm hard}$ vs. $F_{\rm X}^{\rm hard}$, for the spectra shown in figure 7.19. The Galactic absorptions are fixed as given in table 7.5, and $\Gamma^{\rm soft}$ are fixed to 6.0. Contours (from inner to outer) represent 68, 90 and 99% confidence levels, and crosses show the best fit position.

are larger than that of $F_{\rm X}^{\rm hard}$, this is due mainly to the bright soft sources in d-LSS (e.g. NGC 5098).

Even summing up all the CXB spectra in our sample fields, the $PL^{\rm hard}$+$PL^{\rm soft}$ model has been acceptable as given in table 7.5; i.e. any other component is not required to explain the CXB spectrum in the 0.7–10 keV energy band. This very flatness of the average CXB spectrum is a remarkable fact. In figre 7.19d, there appears a possible edge-like structure ~ 8 keV, which is due probably to a little over-subtraction of RNXB which contains the 8.04 keV instrumental Cu-K line. We note again that the statistical errors of the estimated RNXB spectrum are dominant in fitting the total CXB spectrum.

Chapter 8

Discussion and conclusion

8.1 Average CXB spectrum

8.1.1 Summary of the observation

In chapter 6, we have studied the average CXB spectrum in the LSS field including point sources. The background (= RNXB; residual non X-ray background) spectrum to be substracted, and the detector response to be convolved to the model were created as described in chapter 4. The 0.6–10 keV CXB spectrum in the LSS field has been successfully fitted with a model consisting of an absorbed ($N_{\rm H} = 1.1 \times 10^{20}$ cm^{-2}) hard power-law model ($PL^{\rm hard}$) of $\Gamma^{\rm hard} \sim 1.5$, plus a soft component expressed by either a steep power-law model ($PL^{\rm soft}$) of $\Gamma^{\rm soft} \sim 6$ or a low-temperature Raymond-Smith model of $kT \sim 0.3$ keV. The soft component is statistically significant only when the data below $\sim$ 1 keV is included. Thus, the spectrum is consistent with a single power law above $\sim$ 1.2 keV. In §6.4, we conducted detailed investigations on the systematic errors using the $PL^{\rm hard} + PL^{\rm soft}$ model, and determined the error regions of the model parameters as:

$$\begin{aligned} \Gamma^{\rm hard} &= 1.486 \ \pm 0.021 \ \pm 0.040 \\ F_{\rm X}^{\rm hard} &= 6.14 \ \pm 0.08 \ \pm 0.92 \quad (10^{-8} \ \text{erg s}^{-1}\ \text{cm}^{-2}\ \text{str}^{-1};\ \text{2–10 keV}) \\ F_{\rm X}^{\rm soft} &= 1.40 \ \pm 0.27 \ \pm 0.22 \quad (10^{-8} \ \text{erg s}^{-1}\ \text{cm}^{-2}\ \text{str}^{-1};\ \text{0.5–2 keV}), \end{aligned} \tag{8.1}$$

where the former error represents the 90% confidence level statistical erorr and the latter represents the systematic errors. The systematic error of $F_{\rm X}^{\rm hard}$ represents the absolute flux uncertainty ($\sim$ 15%), but the relative flux uncertainty is 3%.

In chapter 7, we have developed the method of eliminating point sources brighter than a fixed threshold intensity (source-masking). Utilizing the source-maskings, we created the average CXB spectra in LSS excluding point sources brighter than $\sim 2\times10^{-13}$ erg s^{-1} cm^{-2} (threshold = 0.10) or $\sim 1.2\times10^{-13}$ erg s^{-1} cm^{-2} (threshold = 0.06) in §7.5. We conducted the $PL^{\rm hard} + PL^{\rm soft}$ fit to these spectra with the detector responses corrected for the decrease in the integration region. We could not find any significant spectral changes on

the average CXB spectrum in LSS, although $F_X^{\rm hard}$ decreased by 9.2±1.5% and 14.8±1.6% corresponding to the source-masking threshold of 0.10 and 0.06, respectively. We also created the total CXB spectrum, which is the best-statistics CXB spectrum we can obtain, by summing up the spectra in our 10 sample fields after processed through the source-maskings at the threshold of 0.10. Even for this total CXB spectrum, the $PL^{\rm hard} + PL^{\rm soft}$ model was fully acceptable and we could not find any spectral features in the average CXB spectrum. Again, the spectrum above $\sim$ 1.2 keV was essentially consistent with a single power-law.

8.1.2 Comparison with previous observations

In the 3–10 keV energy band, the CXB spectrum has been expressed in a power-law model of $\Gamma = 1.4$ or a thermal bremsstrahlung model of $kT = 40$ keV, as reviewed in §2.1. On the other hand, ROSAT reported steeper ($\Gamma \sim 2.1$) slope in the 0.5–2 keV energy band, yet it may be quite isotropic. In the present thesis, we have obtained much better-quality 0.7–10 keV CXB spectrum in both statistics and energy resolution, owing to the ASCA XRT+GIS.

To make a comparison, we plot the unfolded 0.6–10 keV energy spectra of the average CXB in LSS including point sources, together with those obtained with HEAO-1 A2, Einstein, ROSAT, and ASCA SIS. Although our results show a little steeper photon index of $\Gamma^{\rm hard} \sim 1.49$, it is probably consistent with HEAO-1 A2 results of $\Gamma \sim 1.4$, considering our systematic errors (~ 0.04), the possible field-to-field variation (~ 0.06), and that the Crab photon index obtained with the XRT+GIS seems to be steeper by ~ 0.06 than the generally suggested values (§4.2.5). The absolute flux of the CXB is also consistent with HEAO-1 A2, whose error region of the power-law normalization is 8–11 keV cm^{-2} s^{-1} str^{-1} keV^{-1}.

Our results indicate that $PL^{\rm hard}$ is dominant down to $\sim$ 1.2 keV. Below $\sim$ 1.2 keV, the very steep component of $\Gamma \sim 6$ appears, although its level varies from field to field. Our unfolded spectra somewhat depend on the choice between the power-law or Raymond-Smith model as the soft-component, which is an artifact caused by the process of unfolding. We can constrain almost nothing below $\sim$ 0.7 keV with the ASCA XRT+GIS.

Naturally, comparion between the GIS and the ROSAT PSPC results are of significant interest and of great importance. In figure 8.1, our unfolded spectrum appears roughly consistent with the ROSAT PSPC result, in such a way that the ROSAT slope of $\Gamma \sim 2.1$ is well reproduced by the combination of $\Gamma^{\rm hard} \sim 1.4$ and $\Gamma^{\rm soft} \sim 6$ components. It is however very difficult and misleading to compare these unfolded spectra, because they are affected by the effects so called "obliging"; i.e. the unfolded spectrum tends to obey

the particular model used for the specral deconvolution. Accordingly we make comparion in space of the observed quantities. To do this, we fitted our entire LSS spectrum with a model consisting of two power-laws and a soft Raymond-Smith component. We fixed the second power-law slope to $\Gamma = 2.1$ and the *RS* temperature to 0.3 keV, both indicated by the ROSAT spectrum. We left the other model paramters all free. We have then found that our spectrum does not require the $\Gamma = 2.1$ component, and the 90% upper limit on its contribution at 1 keV is only 32% of the total flux. We varied the second power-law slope in the range 1.7–2.5, but the conclusion remained essentially unchanged. This indicates that the CXB spectrum obtained with the GIS is actually composed of the hard power-law of $\Gamma \sim 1.4$ and the very steep (probably Galactic) component. Perhaps the sharp spectral break produced by these two distinct components could not be resolved by the ROSAT PSPC, because of the insufficient spectral resolution ($\Delta E/E \simeq 0.45\,E^{-0.5}$). We do not think that this discrepancy is due to the difference in the observed fields between ASCA and ROSAT, since our spectra in most of the sample fields have been fitted well with the two component model.

In figure 8.1, our GIS results are slightly inconsistent with those obtained with the ASCA SIS by Gendreau et al. (1995); note that it is much less dangerous to compare these two in the unfolded form, because the two ASCA instruments have much higher energy resolution than the ROSAT PSPC. The discrepancy is found on the following two points. One is that the GIS slope appears to be steeper than the SIS one, which is fixed to 1.4, by $\sim$ 0.1; this may well be explained by the fact that the SIS results are based on the older version XRT ray-tracing program, which has already been confirmed to give a flatter photon index by $\Gamma \sim 0.1$, and that the SIS low-energy response is subject to a larger uncertainty than the GIS. The other discrepancy is the considerably higher level of the soft comonent indicated by the GIS spectrum, which appears to be significant even considering the mutual instrumetal calibration differences. Given that the soft component exhibit a signficant field-to-field variation, this may be attributed to the difference in the observed field; our sample field is LSS, whereas that of the ASCA SIS is the Lynx Field, Lockman Hole, QSF3, NEP, and Draco Field. To show typical field-to-field variation, in figure 8.2, we plotted the unfolded CXB spectrum from the XRT+GIS, for the LSS, NEP, and ZSYS fields, separately. The spectrum in the ZSYS field well agrees with the SIS spectrum below $\sim$ 2 keV.

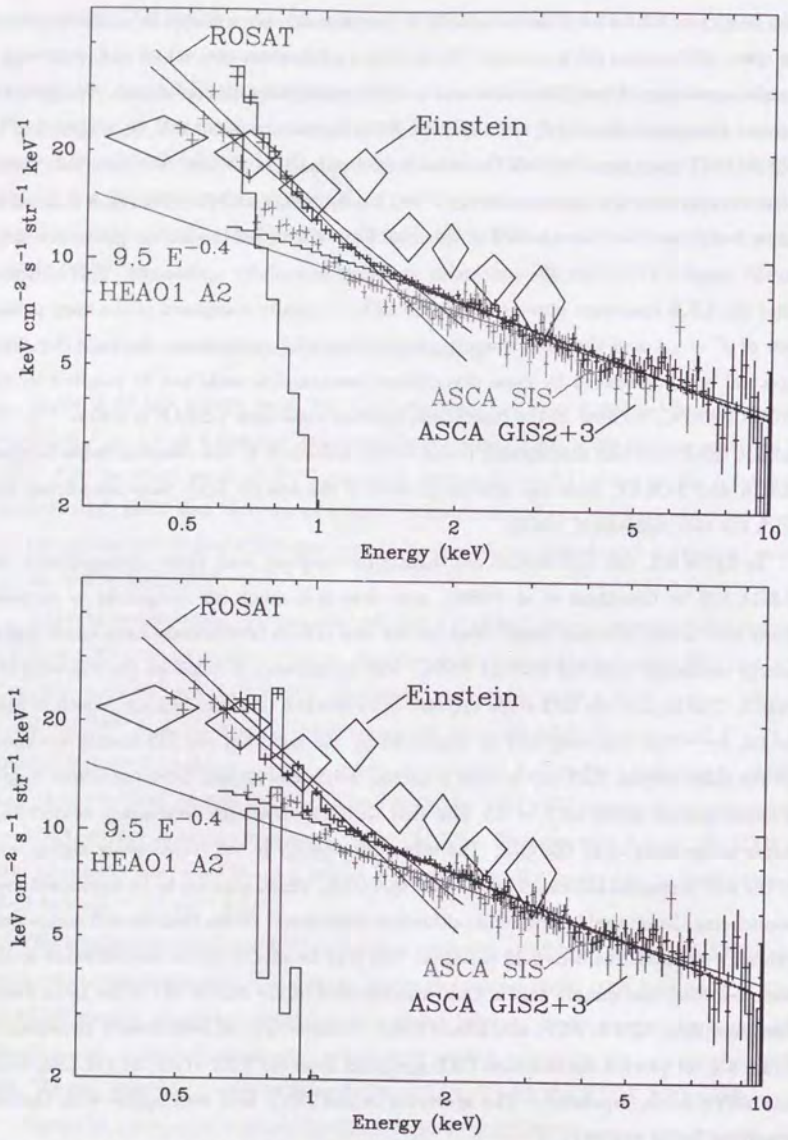

Figure 8.1: Unfolded 0.6–10 keV energy spectra of the average CXB in LSS including point sources. Thick lines and crosses in upper (lower) panel represent the best fit $PL^{\rm soft} + PL^{\rm hard}$ ($RS+PL^{\rm hard}$) model shown in figure 6.5a (figure 6.5b), respectively. Hard- and soft-components are also shown individually in thick lines. Results from ROSAT PSPC (Hasinger 1992), Einstein IPC (Wu et al. 1991), HEAO-1 A2 (Marshall et al. 1980), and ASCA SIS (Keith et al. 1995) are overlaied.

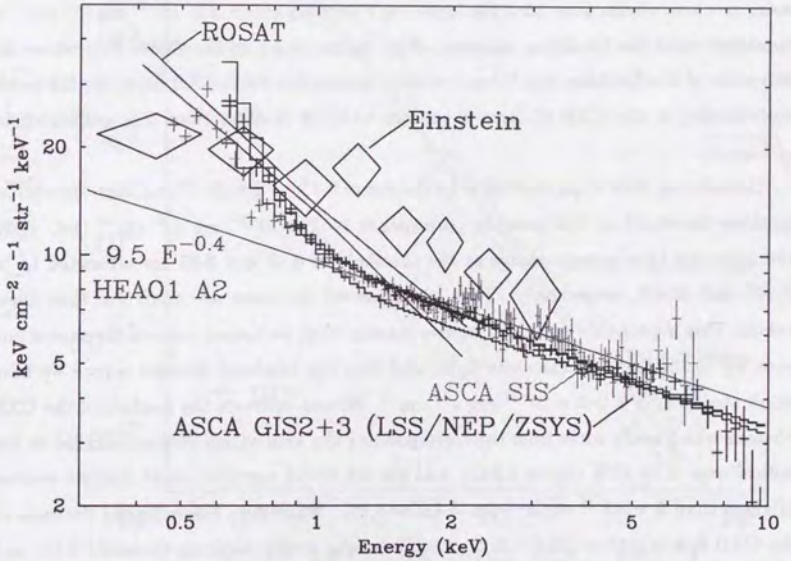

Figure 8.2: Same as upper panel of figure 8.1, except that three GIS spectra in LSS, NEP, and ZSYS after processed through the source-masking at the threshold of 0.10 are instead plotted, separately.

8.1.3 Effects of discrete sources

By applying the source-maskings, we have observed $9.2 \pm 1.5\%$ and $14.8 \pm 1.6\%$ decreases of $F_X^{\rm hard}$ in the LSS field, corresponding to the source-masking threshold of 0.10 and 0.06, respectively. We examine these values from the viewpoint of the $\log N$-$\log S$ relation. From the $\log N$-$\log S$ relation, we can estimate the decrease of the CXB flux when we removed the contributions of discrete sources brighter than a certain level. In figure 8.3, we show the $\log N$-$\log S$ relation in the 2–10 keV energy band measured with previous X-ray observations (HEAO-1 A2, Ginga, and ASCA). Although ROSAT reported the deviation from the Euclidian slope below $S \sim 10^{-14}$ erg s^{-1} cm^{-2} (ref. §2.3), most previous results show that the $\log N$-$\log S$ relation above $S \sim 10^{-13}$ erg s^{-1} cm^{-2} is consistent with the Euclidian universe. If we denote $S_{100\%}$ as the source flux where the extension of the Euclidian $\log N$-$\log S$ relation crosses the 100% CXB limit, the fractional contribution to the CXB of discrete sources which is brighter than S is calculated by $\sqrt{S_{100\%}/S}$.

Considering that $S_{100\%}$ derived from the figure 8.3 is $\sim 8 \times 10^{-15}$ and that our source-masking threshold of 0.10 roughly corresponds to 2×10^{-13} erg s^{-2} cm^{-2} (ref. §7.3), the decreases by source-maskings at the threshold of 0.10 and 0.06 are estimated to be 20.0% and 25.8%, respectively. Thus, the observed decreases are much less than these values. This is probably explained by two reasons; that we cannot remove the source flux entering to the f.o.v. as the stray light, and that the brightest discrete soruce we have eliminated in LSS is $2\text{–}3 \times 10^{-12}$ erg s^{-1} cm^{-2}. We can estimate the fraction of the CXB photons which really come from the corresponding sky area within 20 mm centered on the optical axis to be 65% (figure 4.14b), and the fractional contribution of discrete sources brighter than 3×10^{-12} erg s^{-1} cm^{-2} to be 5.2%. Therefore, the expected decrease of the CXB flux is $0.65 \times (20.0 - 5.2) = 9.6\%$ for the source-masking threshold 0.10, and $0.65 \times (25.8 - 5.2) = 13.4\%$ for the source-masking threshold 0.06. These values are consistent with the observed ones.

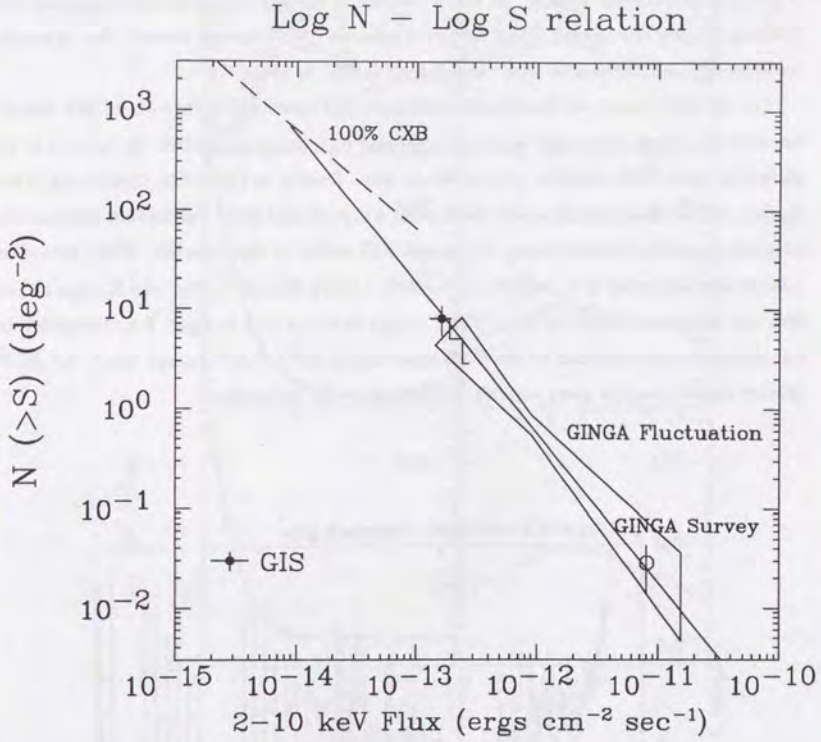

Figure 8.3: The $\log N$-$\log S$ relation in the 2–10 keV energy band. Solid line with a slope of -1.5 represents the extension of the HEAO-1 A2 result expressed in equation 2.5. Dashed line with a slope of -1.0 represents the 100% CXB limit, assuming the CXB intensity as 6.2×10^{-8} erg s^{-1} cm^{-2} str^{-2} (2–10 keV). The 90% confidence contour from Ginga fluctuation analysis (Hayashida 1990), the point from Ginga source survey (Kondo 1991), and the preliminary results from ASCA Large Sky Survey (Ueda, private communication) are overlaid. Photon index of 1.7 is assumed to calculate the flux. This figure is kindly provided by Y. Ueda.

8.1.4 Constraints on the AGN mixture models of the CXB

As reviewed in §2.3.3, it has been suggested that the flat spectrum of the CXB, i.e. $\Gamma \sim 1.4$ in the 2–10 keV energy band, could be explained by the superposition of absorbed sources at different redshifts. The main candidates of the absorbed sources are Seyfert 2 galaxies and similar objects. So far, a number of models are presented to explain the CXB by mixing the Seyfert 1 and Seyfert 2 galaxies (AGN mixure model). For example, we show the calculations by Matt and Fabian (1994) in figure 8.5.

On the other hand, we have determined the CXB spectrum in the $\sim$ 1–10 keV energy band to be almost featureless and well expressed by a single power-law. In figure 8.4, we show our total CXB spectrum plotted in the same fashion as figure 8.5. Comparing these figures, we can immediately reject the models A1, A10, and A16. Taking into account the iron line emissions (dashed lines), the model A17 would be also rejected. When absorbed spectra are subjected to a redshift of $z = 2$–3, a sharp feature by the iron K-edge or the iron line emission appears in the 1–3 keV energy band, as seen in figure 8.5. According to our accurate measurements of the CXB spectrum in the 1–3 keV energy band, the AGN mixure models require more carefull fine-tuning of the parameters.

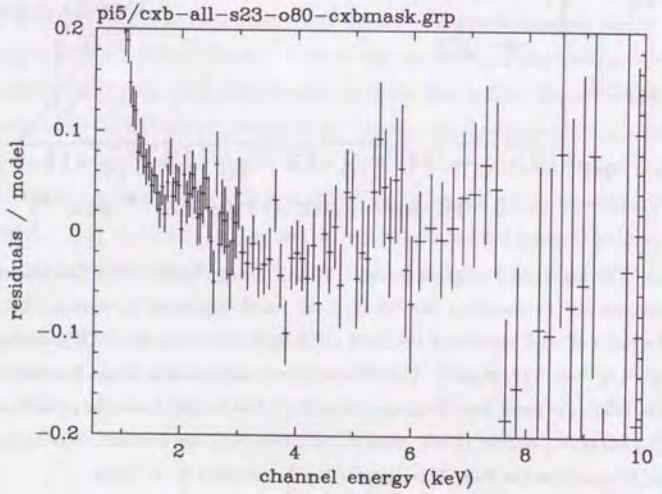

Figure 8.4: The fractional residuals, i.e. (Data − Model) / Model, of the total CXB spectrum shown in figure 7.19d to a power-law of $\Gamma = 1.4$. The data excess just below $\sim$ 2 keV is due partly to the energy resolution ($\sim$ 20% FWHM at 1 keV) of the GIS.

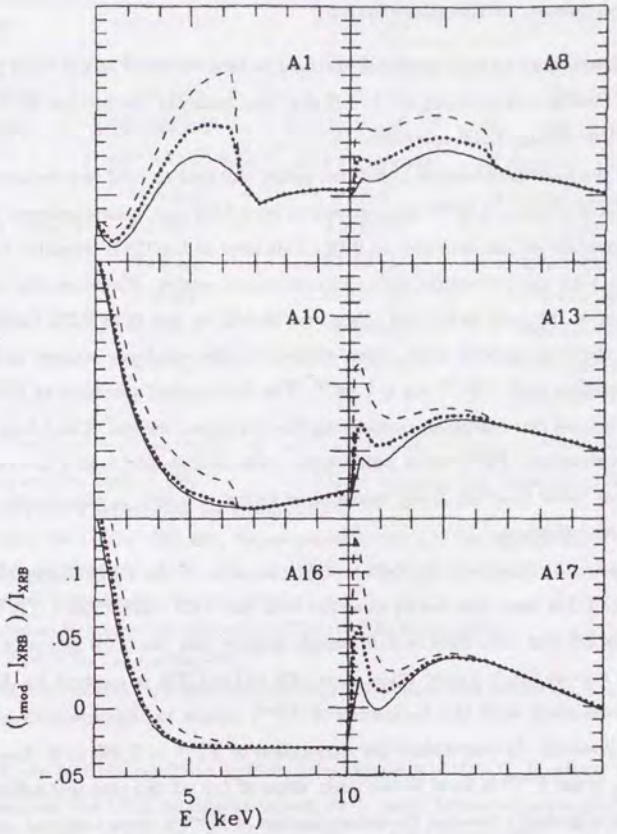

Figure 8.5: The fractional residuals of various Seyfert 1 and Seyfert 2 mixture 2–10 keV CXB spectra to a power-law of $\Gamma = 1.4$, adopted from Matt and Fabian (1994). The solid lines show the model without no line emission. The dotted lines include the iron line emission from the intervening matter, while the dashed lines show the further intrinsic line emission. The fraction of Seyfert 2 galaxies is ranging 0.6–0.8. Seyfert 1 (unabsorbed) and Seyfert 2 (absorbed) are assumed to have the same intrinsic spectrum and evolve in the same way, in terms of the unified model of the AGN (e.g. Antonucci & Miller 1985). The model A1 is the unevolved model, while the evolution of the volume emissivity as $(1+z)^{2.5}$, $(1+z)^{4.5}$ and $(1+z)^6$ are assumed for A8/A10, A13/A16, and A17, respectively. The difference between A8 (A13) and A10 (A16) is the lower-limit N_{H1} of the intrinsic absorption; $N_{H1} \sim 10^{23}$ cm^{-2} for A8, A13, and A17, while $N_{H1} = 10^{24}$ cm^{-2} for A13 and A16.

8.2 Field to field fluctuation of the CXB

8.2.1 Summary of the observation

In chapter 7, we have investigated the field-to-field variation of the CXB properties in 13 sample fields each covering the $\sim$ 1–2 deg^2 sky, utilizing the method as we have done to study the average CXB spectrum.

From the spectral fitting of individual fields, the field-to-field rms variation of the 2–10 keV CXB intensity ($F_X^{\rm hard}$) was derived to be $\pm$3.4% rms, after processed through the source-maskings at the threshold of 0.10. This level of the CXB intensity fluctuation is consistent with being constnat within the systematic errors. Therefore, the intrinsic rms fluctuation of the 2–10 keV CXB brightness should be less than 9.2% (90% confidence level) on the $\sim 1^\circ$ angular scale, when we remove discrete X-ray sources with 2–10 keV fluxes exceeding $\sim 2 \times 10^{-13}$ erg s^{-1} cm^{-2}. The field-to-field variation of $\Gamma^{\rm hard} \sim 0.05$ is likely to be real but marginal, considering the systematic errors. The 0.5–2 keV flux of the soft component ($F_X^{\rm soft}$) varies significantly from field to field, which is consistent with the general belief that the X-ray background below $\sim$ 2 keV is anisotropic, due to the Galactic contributions.

We have also examined the field-to-field variation of the CXB brightness by determining the CXB base level ($= \alpha$) observed with the XRT+GIS. This CXB base level α varies only 2% rms from field to field, which implies that the CXB intensity is isotropic by $\sim$ 2% rms at the 1–2 deg^2 scale, if $\sim$ 12% of the CXB is resolved by ASCA. This result is consistent with the fluctuation of $F_X^{\rm hard}$, within the uncertainties of $F_X^{\rm hard}$ and α determinations. In particular, the fluctuation of $F_X^{\rm hard} \sim 2.8\%$ gets close to that of $\alpha \sim 2.0\%$, when $\Gamma^{\rm hard}$ is fixed to the mean slope of 1.44 at the source-masking threshold of 0.06. It is probably because the determination of $F_X^{\rm hard}$ is more weighted on the region where exposure is deep, that the fluctuation of $F_X^{\rm hard}$ tends to be larger than that of α. This effect is explained by the larger Ω_e (effective beam size) for α (ref. appendix H).

8.2.2 Comparison with previous measurements

In table 8.1, we summarize previous measurements of the CXB isotropy in the 2–10 keV energy band, as well as our present work. Our distinctive features are much smaller S_c and Ω_e than those of Ginga LAC by about one order of magnitude, although our data sample ($= 10$) is much smaller than those of HEAO-1 A2 ($= 698$) or Ginga LAC ($= 151$). Here, S_c (erg s^{-1} cm^{-2}) represents the upper cut-off flux of the discrete sources in the detector f.o.v., and Ω_e (deg^2) represents the effective beam size (or effective solid angle) of the detector when observing the Euclidian sky (see appendix H for their definitions).

Table 8.1: Summary of the previous results and the present work (ASCA XRT+GIS)

Instrument	HEAO-1 A2†	Ginga LAC‡	ASCA XRT+GIS
Data	698 sample	151 sample	10 sample
Effective Area	530 cm^2	4,000 cm^2	200 cm^2
Energy Band	2.5–46 keV	2–10 keV	0.6–10 keV
f.o.v.	$3^\circ \times 3^\circ$ with 6° scan	$1^\circ \times 2^\circ$ pointing	$40'$ diameter $\sim 3'$ imaging
Ω_e [a]	15.8 deg^2	1.3 deg^2	0.14 deg^2 / 1 pointing
S_c [b] (erg s^{-1} cm^{-2})	8×10^{-11}	6×10^{-12}	2×10^{-13}
I_{CXB} [c]	13.3 c/s	15–16 c/s	0.25 c/s/GIS2+3
I_{BGD} [d]	3.4 c/s	50–100 c/s	0.12 c/s/GIS2+3
σ_{stat} [e]	0.18 c/s	0.11 c/s	0.003 c/s/GIS2+3
σ_{BGD} [f]	0.28 c/s	0.152 c/s	0.004 c/s/GIS2+3
σ_{CXB} [g]	0.16 c/s	0.9 c/s	$\lesssim$ 0.01 c/s/GIS2+3
σ_{CXB}/I_{CXB}	2.8%	$\sim$ 6%	$\lesssim$ 3.4%

† These values are from Shafer (1983). ‡ These values are from Hayashida (1990).

[a] Effective beam size of the detector. See appendix H.

[b] Upper cut-off of the 2–10 keV flux from discrete sources in the f.o.v. See appendix H.

[c] Average CXB counting rate.

[d] Typical intrinsic background (= RNXB) counting rate.

[e] Typical statistical 1σ error to the observed (= CXB+RNXB) counting rate.

[f] Typical 1σ error of the I_{BGD} estimation.

[g] Observed CXB fluctuation, i.e. excess variance of $P(D)$ distribution after subtracting σ_{stat} and σ_{BGD}.

In figure 8.6, we plot the positions of these measurements on the Ω_e-S_c plane. Therefore, we have observed the CXB on smaller scales, with much fainter objects. Such small S_c and Ω_e are mostly owing to the imaging capability of the XRT+GIS and the procedure of the source-masking. In addition, as given in table 8.1, the very low counting rate of the intrinsic background (= RNXB) makes our result reliable.

The value of $\Omega_e = 0.14$ deg^2 for the GIS applies only to one sensor and one pointing without source-masking. We roughly estimate the actual Ω_e for our CXB observations in table 8.2, by multiplying 0.41 to each integration area. This value of 0.41 is the ratio of $\Omega_e = 0.14$ deg^2 to the geometrical integration area of 0.34 deg^2 on the sky corresponding to the 20 mm radius of one GIS f.o.v. As described in appendix H, there is a relation of $(\sigma_{CXB}/I_{CXB}) \propto \Omega_e^{-0.5}\, S_c^{0.25}$, where (σ_{CXB}/I_{CXB}) is the fractional CXB fluctuation due to the statistical fluctuation of the discrete source number in the f.o.v. If we take $\Omega_e = 0.5$ deg^2 as a typical effective solid angle of our observations, we can predict the CXB fluctuation with the XRT+GIS utilizing the HEAO-1 A2 values, as

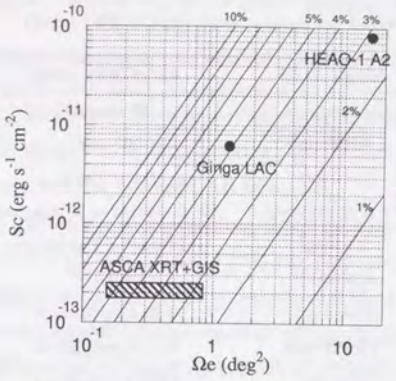

Figure 8.6: Positions of the HEAO-1 A2, Ginga LAC, and ASCA XRT+GIS on the Ω_e-S_c plane. Contours labeled 1%, 2%, ..., 10% represents the expected fractional CXB fluctuation, i.e., σ_{CXB}/I_{CXB}.

Table 8.2: Rough estimations of the effective beam size Ω_e (deg^2) for each CXB observation

ID	Name	No-Mask†	0.10†	0.06†
–	LSS	2.94	2.13	1.59
1	SA57	0.28	0.24	0.19
2	a-LSS	0.85	0.70	0.53
3	b-LSS	0.95	0.73	0.55
4	c-LSS	0.92	0.77	0.60
5	d-LSS	0.89	0.53	0.39
6	Draco	0.29	0.26	0.22
7	NEP	0.24	0.17	0.14
8	QSF3	0.18	0.14	0.11
9	ZSYS	0.68	0.47	0.36
10	BF	0.60	0.33	0.22
11	Jupiter	0.16	0.11	0.06
12	Arp 220	0.16	0.15	0.09
13	3C368	0.16	0.13	0.05

† Threshold level of the source-maskings on M^{FLAT}.

$2.8 \times (15.8/0.5)^{0.5} \times (8 \times 10^{-11}/2 \times 10^{-13})^{-0.25} = 3.5\%$, which is fully consistent with our result. This prediction assumes the Euclidian $\log N$-$\log S$ relation with the same normalization on the whole sky, i.e., discrete X-ray sources are distributing uniformly in the whole Euclidian universe. Therefore, this fact, that our CXB fluctuation is consistent with the extension of the HEAO-1 A2 result, implies not only the spatial isotropy of the $\log N$-$\log S$ relation but also that the Euclidian $\log N$-$\log S$ relation extends at least to our S_c flux of $\sim 2 \times 10^{-13}$ erg s^{-1} cm^{-2}. This supports the $\log N$-$\log S$ relation derived from the Ginga fluctuation analysis (Hayashida 1989) and the direct $\log N$-$\log S$ measurement by the ASCA Large Sky Survey (Ueda 1996), which are shown in figure 8.3.

We note here that the calculations conducted above fully takes into account the effects of stray-lights. As described in §H.2, contribution of the stray-lights to Ω_e is expected to be less than 10% of the total Ω_e. This is because the low transmission region in the

f.o.v. produces insignificant source-confusion noise, as expressed by equation (H.5). In other words, there must exist quite bright sources in such region in order to generate a detectable fluctuation, while such bright sources are rare. On the other hand, the stray-lights contributes to the absolute CXB flux as much as by 35%, as mentioned in §8.1.3. Therefore, the stray-lights generally work to reduce (σ_{CXB}/I_{CXB}), although we cannot remove discrete sources from the stray-lights, which works to increase (σ_{CXB}/I_{CXB}).

Acknowledgement

First of all, I would like to express my best gratitude to Prof. K. Makishima for his continuous guidance and hearty support for this thesis. He has also led me throughout these five years of my graduate course, and I have learned much from him. I am deeply grateful to Dr. T. Takahashi, Mr. Y. Ueda, and Mr. Y. Ogasaka, for their constructive discussions and cooperations. I also thank Prof. Y. Suto, Prof. H. Inoue, Prof. R. Mushotzky, and Dr. K. Gendreau for their valuable comments and suggestions.

The ASCA observatory was developed, launched, and operated successfully with great efforts by ASCA team members, including people at Institute of Space and Astronautical Science (ISAS), University of Tokyo, Tokyo Metropolitan University, Institute of Physical and Chemical Research (Riken), Nagoya University, Osaka University, Kyoto University, Iwate University, and Miyazaki University. I am indebted to the staff of the ASCA Guest Observers Facility. I owe a great deal to all the scientists and engineers who worked on the development and operation of the ASCA project.

I wish to thank all the members, past and present, of the cosmic X-ray astronomy group in the University of Tokyo, including Prof. T. Ohashi, Dr. M. Tashiro, Mr. Y. Fukazawa, Dr. T. Tsuru, Dr. M. Ishida, Dr. T. Sakao, Dr. T. Mihara, Dr. M. Inda Koide, Dr. Y. Kohmura, Dr. Y. Ikebe, Mr. S. Kamijo, Mr. H. Kaneda, Ms. K. Matsushita, Mr. T. Tamura, Ms. N. Iyomoto, Ms. E. Idesawa, Mr. T. Mizuno, and Mr. H. Obayashi. I especially thank Mr. M. Hirayama, Mr. T. Kotani, and Mr. R. Fujimoto among many people in other institutes.

I appreciate Dr. T. Kii, Dr. T. Tsuru, and Dr. N. Yamasaki who kindly agreed me to use their GO-phase data. I also appreciate the authors of XSPEC, DISPLAY45, ASCA_ANL, SimASCA, SimARF, jbldarf, XRT ray-tracing, mule, TEX, LATEX, tgif, etc.

References

[1] Antonucci, R.R.J & Miller, J.S. 1985, *Astrophys. J.*, **297**, 621.

[2] Awaki, H. *et al.* 1990, *Nature*, **346**, 544.

[3] Awaki, H. *et al.* 1991, *Publ. Astron. Soc. Japan*, **43**, 195.

[4] Awaki, H. *et al.* 1993, *Adv. Space Res.*, **13**, 221.

[5] Awaki, H. *et al.* 1994, Publ. Astron. Soc. Japan, **46**, L65.

[6] Bahcall, N.A. 1988, *Ann. Rev. Astron. Astrophys.*, **26**, 631.

[7] Bahcall, N.A. & West, M.J. 1992, *Astrophys. J.*, **392**, 419.

[8] Bolt, E. 1987, *Phys. Rep.*, **146**, 215.

[9] Boyle, B.J. *et al.* 1993, *Mon. Not. Royal Astron. Soc.*, **260**, 49.

[10] Brandbardi-Raymont, G. *et al*, 1994, *Mon. Not. R. Astron. Soc.*, **270**, 947

[11] Burke, B.E. *et al.* 1991, *IEEE Trans.* **ED-38**, 1069

[12] Burrows, D.N., & Mendenhall, J.A. 1991, *Nature*, **351**, 629.

[13] Chen, L.W. & Fabian, A.C. in preparation

[14] Condon, J. J. 1974, *Astrophys. J.*, **188**, 279

[15] Cowsik, R., & Kobetich, E.J. 1972, *Astrophys. J.*, **177**, 585.

[16] Cristiani *et al.* 1984, *Astro. Astrophys.*, **135**, 122.

[17] Dotani,T. 1995 in ASCA News No.3

[18] Ebeling, H. *et al.* 1995, in *proceedings on Röntgenstrahlung from Universe* , at Würzburg, eds. J. Trümper and U. Zimmermann, in press.

[19] Fabbiano, G. 1989, *Ann. Rev. Astron. Astrophys.*, **27**, 87.

[20] Fabbiano, G. *et al.* 1989, *Astrophys. J.*, **347**, 127.

[21] Fabian, A.C. & Balcons, X. 1992, *Ann. Rev. Astron. Astrophys.*, **30**, 429.

[22] Fabian, A.C. *et al.* 1990, *Mon. Not. Royal Astron. Soc*, **242**, 14.

[23] Fabianno, G. and Trinchieri, G. 1985, *Astrophys. J.*, **296**, 430.

[24] Fanti *et al.* 1977, *Astro. Astrophys.*, **61**, 487.

[25] Field, G.B., & Perrenod, S.C. 1977, *Astrophys. J.*, **215**, 717.

[26] Fukazawa, Y. *et al.* 1994, *Publ. Astron. Soc. Japan*, **46**, L141.

[27] Gendreau, K.C. *et al.* 1995, *Publ. Astron. Soc. Japan*, **47**, L5.

[28] Giacconi, R.H. *et al.* 1962, *Phys. Rev. Lett.*, **9**, 439.

[29] Giacconi, R.H. *et al.* 1979, *Astrophys. J. letters*, **234**, L1.

[30] Gioia, I.M. *et al.* 1984, *Astrophys. J.*, **283**, 495.

[31] Gioia, I.M. *et al.* 1990, *Astrophys. J. Suppl.*, **72**, 567.

[32] Goerigk, W. *et al.* 1983, *Astro. Astrophys.*, **120**, 63.

[33] Griffiths, R.E. and Padovani, P. 1990, *Astrophys. J.*, **360**, 483.

[34] Hamilton, T.T., & Helfand, D.J. 1987, *Astrophys. J.*, **318**, 93.

[35] Hasinger, G. 1992, in *The X-Ray Background*, eds. X. Barcons and A.C. Fabian (Cambridge University Press: Cambridge), p229.

[36] Hasinger, G. *et al.* 1991, *Astro. Astrophys.*, **246**, L2.

[37] Hasinger, G. *et al.* 1993, *Astro. Astrophys.*, **275**, 1.

[38] Hasinger, G. *et al.*, 1993, *Astron. Astrophys.*, **275**, 1

[39] Hayashida, K. 1989, *Ph. D dissertation of Univ. of Tokyo, ISAS RN* 466.

[40] Heiles, H. & Cleary, M.N. 1979, *AJPAS*, **47**, 1.

[41] Heisker, J. *et al.* 1989, *Astrophys. J.*, **347**, 52.

[42] Hewitt, A. & Burbidge, G. 1989, *Astrophys. J. Suppl.*, **69**, 1.

[43] Hoyle, F. 1963, *Astrophys. J.*, **137**, 993.

[44] Inoue, H. *et al.* 1979, *Astrophys. J.Letters*, **227**, L85.

[45] Iwan, D. *et al.* 1982, *Astrophys. J.*, **260**, 111.

[46] Jahoda, K. *et al.* 1991, *Astrophys. J.*, **378**, L37.

[47] Kii, T. *et al.* 1995 in *IRAS galaxies observed with ASCA*

[48] Kondo, H. 1991, *Ph. D dissertation of Univ. of Tokyo, ISAS RN* 494.

[49] Koo, D. C. 1986, *Astrophys. J.*, **311**, 651

[50] Koo, D. C. and Kron, R. G. 1988, *Astrophys. J.*, **325**, 92

[51] Koyama, K. 1989, *Publ. Astron. Soc. Japan*, **41**, 665.

[52] Koyama, K. *et al.* 1984, *Publ. Astron. Soc. Japan*, **36**, 659.

[53] Koyama, K. *et al.* 1986, *Publ. Astron. Soc. Japan*, **38**, 121.

[54] Koyana, K. *et al.* 1986, *Publ. Astron. Soc. Japan*, **38**, 121.

[55] Lahav, O. *et al.* 1993, *Nature*, **364**, 693.

[56] Lockman, F. J., Jahoda, K., McCammon, D. 1986, *Astrophys. J.*, **302**, 432

[57] Majewski, S. R. *et al.*, 1994, *Publ. Astron. Soc. Pscific*, **106**, 1258

[58] Makishima, K. *et al.* 1996, *Publ. Astron. Soc. Japan*, submitted

[59] Makishima, K. *et al* 1994, *Puble. Astron. Soc. Japan*, **46**, L77.

[60] Marshall, F. *et al.* 1984, *Astrophys. J.*, **283**, 50.

[61] Marshall, F. *et al.* 1980, *Astrophys. J.*, **235**, 4.

[62] Marshall, F.J. and Clark, G.W. 1984, *Astrophys. J.*, **287**, 633.

[63] Mather, J.C. *et al.* 1990, *Astrophys. J. letters*, **354**, L41.

[64] Mather, J.C. *et al.* 1994, *Astrophys. J.*, **420**, 439.

[65] Mathis, D. F. *et al.*, 1994, *Bull. American Astron. Soc.*, **185**

[66] Matt, G. and Fabian, A.C., 1994, *Mon. Not. Royal Astron. Soc.*, **267**, 187.

[67] McCammon, D. 1983, *Astrophys. J.*, **269**, 107.

[68] McCammon, D. and Sanders, W.T. 1990, *Ann. Rev. Astron. Astrophys.*, **28**, 657.

[69] McKee *et al.* 1980, *Astrophys. J.*, **242**, 843.

[70] Miyaji, T. 1995, *private commun.*

[71] Mushotzky, R.F. 1983, *Adv. Space Res.*, **3**, 10.

[72] Mushotzky, R.F. *et al.* 1978, *Astrophys. J.*, **225**, 21.

[73] Mushotzky, R.F., Done, C. and Pounds, K.A. 1993, *Annu. Rev. Astron. Astrophys.* , **31**, 717.

[74] Neuschaefer, L. W. and Windhorst, R. A. 1995, *Astrophys. J. Supple.*, **96**, 371

[75] Ogasaka, Y. 1996, Ph.D.Thesis, Gakusyuin University

[76] Ohashi, T. *et al.* 1996, *Publ. Astron. Soc. Japan*, submitted

[77] Piccinotti, G. *et al* 1982, *Astrophys. J.*, **253**, 485.

[78] Primini, F.A. *et al.* 1991, *Astrophys. J.*, **374**, 440.

[79] Protheroe, R.J. *et al.* 1980, *Mon. Notices Roy. Astron. Soc.*, **192**, 445.

[80] Roche, N. *et al.* 1995, *Mon. Not. Royal Astron. Soc.*, **273**, L15.

[81] Rothschild, R. *et al.* 1983, *AstroPhys. J.*, **269**, 423.

[82] Sandars, D.B. *et al.* 1988, *Astrophys. J*, **325**, 74.

[83] Sarazin, C.L. 1986, *Rev. Modern Phys.*, **58**, 1.

[84] Schwartz, D.A. and Gursky, H. 1974, in *X-ray Astronomy*, eds. R. Giacconi and H. Gursky (Dordrecht: Reidel).

[85] Schwartz, D.A. 1979 in *X-ray Astronomy.* Oxford: Pergamon. pp.453

[86] Serlemitsos, P. J. 1981, *NASA Tech. Mem.*, **83848**, 441

[87] Serlemitsos, P. J. 1988, *Appl. Opt.*, **27**, 1447

[88] Serlemitsos, P.J. *et al.* 1995, *Publ. Astron. Soc. Japan*, **47**, 105.

[89] Shafer, R.A. 1983, *Ph. D dissertation of Univ. of Maryland, NASA TM* 85029.

[90] Shafer, R.A., & Fabian, A.C. 1983 in *Early Evolution of the Universe and its Present Structure*, ed. G.O. Abell, G.Chincarini, pp.333-34. Dordrecht: Reidel

[91] Shanks, T. *et al.* 1991, *Nature*, **353**, 315.

[92] Smoot, G.F. *et al.* 1977, *Phys. Rev. Letters*, **39**, 898.

[93] Stocke, J.T. *et al.* 1991, *Astrophys. J. Suppl.*, **76**, 813.

[94] Suto, Y. *et al.* 1996, *Astrophys. J.Letters*, in press

[95] Suginohara, T. 1992, Ph.D.Thesis, University of Tokyo

[96] Tanaka, Y. and Bleeker, J.A.M. 1977, *Space Sci. Rev.*, **20**, 815.

[97] Tanaka, Y. *et al.* 1984, *Publ. Astron. Soc. Japan*, **36**, 641.

[98] Tanaka, Y. *et al.* 1994, *Publ. Astron. Soc. Japan*, **46**, L37.

[99] Tsusaka, Y. *et al*, 1995, *Appl. Opt.*, **34**, 4848

[100] Turner, T.J., & Pound, K.A. 1989, *Mon. Not. Royal Astron. Soc*, **240**, 833.

[101] Tusaka, Y. *et al.* 1995, *App.Otp*

[102] Ueda, Y. 1996, Ph.D.Thesis, University of Tokyo

[103] Warwick, R.S. *et al.* 1980, *Mon. Not. Royal Astron. Soc*, **190**, 243.

[104] Willams, O.R. *et al.* 1992, *Astrophys. J.*, **389**, 157.

[105] Windhorst, R. A., Kron, R. G., Koo, D. C. 1984, *Astron. Astrophys.*, **58**, 39

[106] Wood, *et al.* 1984, *Astrophys. J. Suppl.*, **56**, 507.

[107] Worral, D.M. *et al.* 1982, *Astrophys. J.*, **255**, 111.

[108] Wu X. *et al.* 1991, *Astrophys. J.*, **379**, 564.

[109] Yamasaki, N *et al.* 1995 in *meeting of Astronomical Society of Japan*

[110] Yamashita, A 1995 Master Thesis, University of Tokyo

[111] Yamauchi, S. and Koyama, K. 1993, *Astrophys. J.*, **404**, 620.

[112] Zeldovich, Ya. and Sunyaev, R.A. 1969, *Astrophys. Space Sci.*,**4**, 301.

Appendix A

Log of the observed fields

In table A.3, A.1, and A.2, we show pointing lists of the CXB observations utilized in the present thesis. The observation period, exposure time, Euler angles, and Galactic longitude / latitude of each pointing are given.

Table A.1: Pointing list of the LSS observations in GO-1 and GO-2

No.	Date		Exposure	Euler Angles			Gal.	
	yy/mm/dd	START – END	(sec)	ϕ	θ	ψ	l	b
lss101	93/12/26	10:22 – 17:49	4,770	197.653	59.667	330.298	69.5	84.5
lss102	93/12/26	17:50 – 22:00	4,839	197.458	59.952	330.391	68.0	84.8
lss103	93/12/26	22:00 – 01:50	7,449	197.274	60.244	330.486	66.1	85.1
lss104	93/12/27	01:50 – 10:00	11,159	197.083	60.533	330.578	64.1	85.3
lss105	94/01/04	10:32 – 15:49	3,914	197.316	59.500	330.468	72.7	84.6
lss106	94/01/04	15:50 – 20:22	6,724	197.124	59.791	330.560	71.3	84.9
lss107	94/01/04	20:22 – 02:41	9,165	196.935	60.080	330.653	69.6	85.2
lss108	94/01/05	02:41 – 13:20	5,752	196.751	60.375	330.744	67.7	85.5
lss109	94/01/05	13:21 – 17:42	6,356	197.579	59.439	330.330	71.8	84.4
lss110	94/01/05	17:42 – 23:30	9,119	197.386	59.728	330.432	70.4	84.7
lss111	94/01/05	23:30 – 10:42	8,829	197.200	60.017	330.520	68.7	85.0
lss112	94/01/06	10:43 – 16:00	5,671	197.010	60.309	330.620	66.9	85.3
lss113	94/01/06	16:01 – 20:50	8,149	197.053	59.563	330.598	73.7	84.8
lss114	94/01/06	20:50 – 04:26	10,690	196.862	59.851	330.692	72.3	85.1
lss115	94/01/07	04:26 – 15:29	6,104	196.676	60.147	330.781	70.6	85.4
lss116	94/01/07	15:30 – 19:30	6,305	196.487	60.434	330.871	68.7	85.7
lss201	94/06/16	16:36 – 04:12	7,193	198.548	59.395	150.196	70.7	84.2
lss202	94/06/17	04:12 – 07:42	3,787	198.741	59.101	150.100	72.1	83.9
lss203	94/06/17	07:42 – 10:59	5,032	198.930	58.812	150.001	73.3	83.6
lss204	94/06/17	10:59 – 15:40	3,735	199.114	58.528	149.905	74.4	83.3
lss205	94/06/17	15:40 – 04:10	9,198	199.325	58.239	149.798	75.3	82.9
lss206	94/06/18	04:11 – 07:42	4,324	198.987	58.072	149.976	77.9	83.1
lss207	94/06/18	07:43 – 12:07	2,481	198.793	58.364	150.074	77.0	83.4
lss208	94/06/18	12:07 – 17:10	8,894	198.594	58.649	150.176	76.1	83.7
lss209	94/06/18	17:10 – 04:10	6,415	198.401	58.941	150.273	75.0	84.0
lss210	94/06/19	04:10 – 08:31	5,708	198.210	59.229	150.372	73.8	84.3
lss211	94/06/27	23:12 – 04:04	4,662	198.471	59.163	150.238	72.9	84.1
lss212	94/06/28	04:05 – 08:39	5,312	198.667	58.877	150.135	74.1	83.8
lss213	94/06/28	08:39 – 13:37	7,598	198.863	58.586	150.036	75.2	83.5
lss214	94/06/28	13:37 – 00:48	6,204	199.060	58.299	149.930	76.2	83.2
lss215	94/06/29	00:49 – 05:35	4,932	199.259	58.010	149.832	77.1	82.8
lss216	94/06/29	05:36 – 10:49	6,384	198.721	58.131	150.114	78.8	83.3
lss217	94/06/29	10:51 – 20:25	8,062	198.521	58.424	150.220	78.0	83.6
lss218	94/06/29	20:26 – 02:28	1,482	198.322	58.709	150.324	77.1	83.9
lss219	94/06/30	02:28 – 07:38	5,654	198.863	58.589	150.037	75.2	83.5
lss220	94/06/30	07:38 – 13:20	6,614	197.946	59.290	150.505	74.7	84.5

Table A.2: Pointing list of the LSS observations in GO-3

No.	Date		Exposure	Euler Angles			Gal.	
	yy/mm/dd	START – END	(sec)	ϕ	θ	ψ	l	b
lss301	94/12/25	21:35 – 06:00	7,318	198.212	57.823	330.016	79.8	82.9
lss302	94/12/26	06:01 – 13:25	5,745	198.412	57.541	329.912	80.4	82.6
lss303	95/01/06	08:16 – 14:30	8,271	198.604	57.257	329.815	81.1	82.3
lss304	95/01/07	20:55 – 05:01	9,297	198.804	56.959	329.706	81.7	82.0
lss305	95/01/08	05:02 – 11:10	7,204	199.008	56.673	329.598	82.3	81.6
lss306	95/01/09	10:54 – 12:50	2,864	199.212	56.383	329.491	82.8	81.3
lss307	95/01/09	12:51 – 20:50	6,903	199.278	56.612	329.452	81.5	81.4
lss308	95/01/09	20:51 – 03:20	7,353	199.080	56.906	329.563	80.8	81.8
lss309	95/01/10	03:21 – 08:00	4,733	198.877	57.189	329.665	80.2	82.1
lss310	95/01/10	08:01 – 15:51	10,242	198.677	57.476	329.771	79.6	82.4
lss311	95/01/10	15:52 – 22:20	5,991	198.752	57.708	329.731	78.0	82.5
lss312	95/01/10	22:21 – 04:41	7,796	198.948	57.417	329.623	78.7	82.2
lss313	95/01/11	04:42 – 11:00	9,351	198.481	57.763	329.868	78.9	82.7
lss314	95/01/11	11:02 – 17:21	6,292	199.149	57.128	329.517	79.4	81.9
lss315	95/01/11	17:22 – 23:50	6,268	199.353	56.840	329.408	80.1	81.5
lss316	95/01/11	23:51 – 06:11	8,522	199.553	56.554	329.300	80.7	81.2
lss317	95/01/12	06:12 – 12:40	7,369	198.820	57.934	329.690	76.4	82.6
lss318	95/01/12	12:41 – 19:00	6,040	199.021	57.644	329.585	77.2	82.3
lss319	95/01/12	19:02 – 01:20	7,695	199.224	57.358	329.477	77.9	82.0
lss320	95/01/13	01:20 – 07:50	8,217	199.422	57.068	329.367	78.6	81.7
lss321	95/06/18	16:23 – 02:25	9,119	198.137	58.999	150.414	75.9	84.2
lss322	95/06/19	02:26 – 08:40	7,025	200.118	56.117	149.350	83.2	81.0
lss323	95/06/19	08:40 – 15:11	5,031	200.190	56.346	149.338	81.9	81.1
lss324	95/06/19	15:12 – 23:05	8,769	200.534	56.518	149.145	79.9	81.0
lss325	95/06/19	23:05 – 05:01	7,791	200.328	56.805	149.260	79.2	81.4
lss326	95/07/01	05:03 – 10:30	4,285	200.467	56.290	149.181	81.2	80.9
lss327	95/07/01	10:30 – 17:11	9,490	200.808	56.462	148.996	79.1	80.8
lss328	95/07/02	05:41 – 12:51	7,108	200.196	57.318	149.329	77.1	81.8
lss329	95/07/01	23:21 – 05:40	6,222	200.402	57.032	149.215	77.8	81.5
lss330	95/07/01	17:11 – 23:20	8,683	200.605	56.750	149.106	78.5	81.2
lss331	95/07/05	22:13 – 03:50	4,509	198.234	60.198	150.357	65.1	84.8
lss332	95/07/06	03:50 – 10:09	6,073	198.426	59.913	150.262	66.9	84.5
lss333	95/07/06	10:10 – 16:30	10,526	198.616	59.620	150.165	68.5	84.3
lss334	95/07/06	16:31 – 22:59	9,067	198.811	59.333	150.066	70.0	84.0
lss335	95/07/06	23:00 – 05:20	4,293	199.008	59.046	149.963	71.2	83.7
lss336	95/07/07	05:21 – 11:40	8,216	199.197	58.727	154.868	72.5	83.3
lss337	95/07/07	11:41 – 16:30	7,345	199.396	58.467	149.758	73.6	83.0
lss338	95/07/07	16:30 – 23:00	9,717	199.597	58.180	149.653	74.6	82.7
lss339	95/07/07	23:00 – 05:19	3,444	199.795	57.894	149.548	75.5	82.4
lss340	95/07/08	05:20 – 11:01	6,542	199.994	57.607	149.442	76.3	82.1

Table A.3: Pointing list of the observations

Name	Date		Exposure	Euler Angles			Gal.	
	yy/mm/dd	START – END	(sec)	ϕ	θ	ψ	l	b
SA57	93/12/21	10:25 – 06:50	60,759	196.872	60.660	339.983	64.4	85.5
	93/12/24	13:40 – 10:20	46,211	196.739	60.624	340.035	65.6	85.6
	93/12/28	13:20 – 10:30	95,025	197.012	60.712	339.899	63.1	85.5
	94/01/16	05:12 – 03:25	44,129	196.825	60.782	339.996	63.3	85.6
	94/01/18	03:26 – 01:00	33,820	196.923	60.553	339.949	65.3	85.4
	95/06/02	16:09 – 12:00	181,399	197.586	60.699	138.582	63.8	85.5
Draco	93/06/04	14:13 – 09:10	21,475	256.939	19.289	109.068	102.2	34.2
Field	93/06/05	09:10 – 19:01	10,715	257.587	19.196	108.476	102.3	33.9
	93/06/05	19:02 – 15:35	24,812	258.229	19.096	107.878	102.3	33.7
NEP	93/06/09	23:39 – 10:51	10,691	270.205	23.712	79.027	96.4	29.8
	93/07/20	20:08 – 05:45	16,120	270.588	23.596	117.658	96.4	29.8
	93/10/21	20:58 – 08:10	14,732	270.381	23.196	209.708	96.4	29.8
	94/03/28	08:03 – 20:50	15,235	269.426	23.603	8.028	96.4	29.8
	93/07/02	04:25 – 15:36	13,850	270.025	23.665	100.391	96.4	30.0
	93/08/16	13:44 – 00:35	16,849	270.289	23.500	139.619	96.4	30.0
	93/09/30	05:05 – 17:42	15,301	270.178	23.282	185.975	96.4	30.0
	93/11/16	10:31 – 22:00	15,656	269.593	23.155	240.536	96.4	30.0
QSF3	93/07/11	12:17 – 13:50	24,133	55.283	134.381	39.660	250.8	−52.0
	93/09/15	15:00 – 01:55	11,819	55.045	134.174	343.463	250.8	−52.0
	93/09/10	22:21 – 11:45	12,810	55.041	134.163	341.008	250.8	−52.0
	93/09/21	06:35 – 16:20	11,395	55.046	134.139	335.801	250.8	−52.0
z-system	94/08/09	05:48 – 02:20	19,028	39.629	112.886	11.419	208.6	−65.1
	94/08/10	02:20 – 07:20	24,984	39.843	113.253	11.402	209.6	−65.0
	94/08/11	07:21 – 03:55	19,733	39.550	113.854	11.149	210.8	−65.5
	95/07/28	02:01 – 22:40	23,029	40.400	113.543	16.901	210.5	−64.6
	95/07/27	04:44 – 02:00	23,119	39.609	112.481	16.711	207.6	−65.1
Braccesi	95/05/26	19:42 – 08:33	19,079	196.512	54.510	134.792	105.3	81.1
Field	95/05/28	08:35 – 15:25	26,182	194.631	54.504	124.307	115.0	81.4
	95/12/22	13:51 – 18:20	34,292	195.192	54.201	331.569	108.7	81.0
	95/12/21	09:05 – 13:50	35,185	194.572	54.497	331.848	111.4	81.4
Jupiter	93/06/06	15:44 – 18:50	20,389	185.203	90.575	156.169	286.2	61.2
Arp 220	93/07/26	13:39 – 15:10	23,039	233.934	66.525	154.961	36.5	53.1
3C368	93/09/12	16:38 – 18:10	19,934	271.456	78.944	174.006	37.6	15.3

Appendix B

Contour-map images of the observed fields

We show the counting rate contour-map images $M^{CCF}(SKYX, SKYY)$ in the 0.7–7 keV energy band and the exposure time gray scale map $M^{EXP}(SKYX, SKYY)$ of the CXB observations in figure B.1–B.10. We smoothed the GIS2 and GIS3 images of each pointing independently with the XRT+GIS PSF, and summed them up on the sky. RNXB are not subtracted. See §5.3.2, for detailed handling of observed images.

Contour levels are $(5, 10, ..., 95, 100) \times 10^{-6}$ c s^{-1} pixel^{-1}. Coordinates superposed on the images are J2000. IPC sources and QSOs catalogued in Veron-Cetty and Veron (1993) are also plotted by filled circles and triangles, respectively.

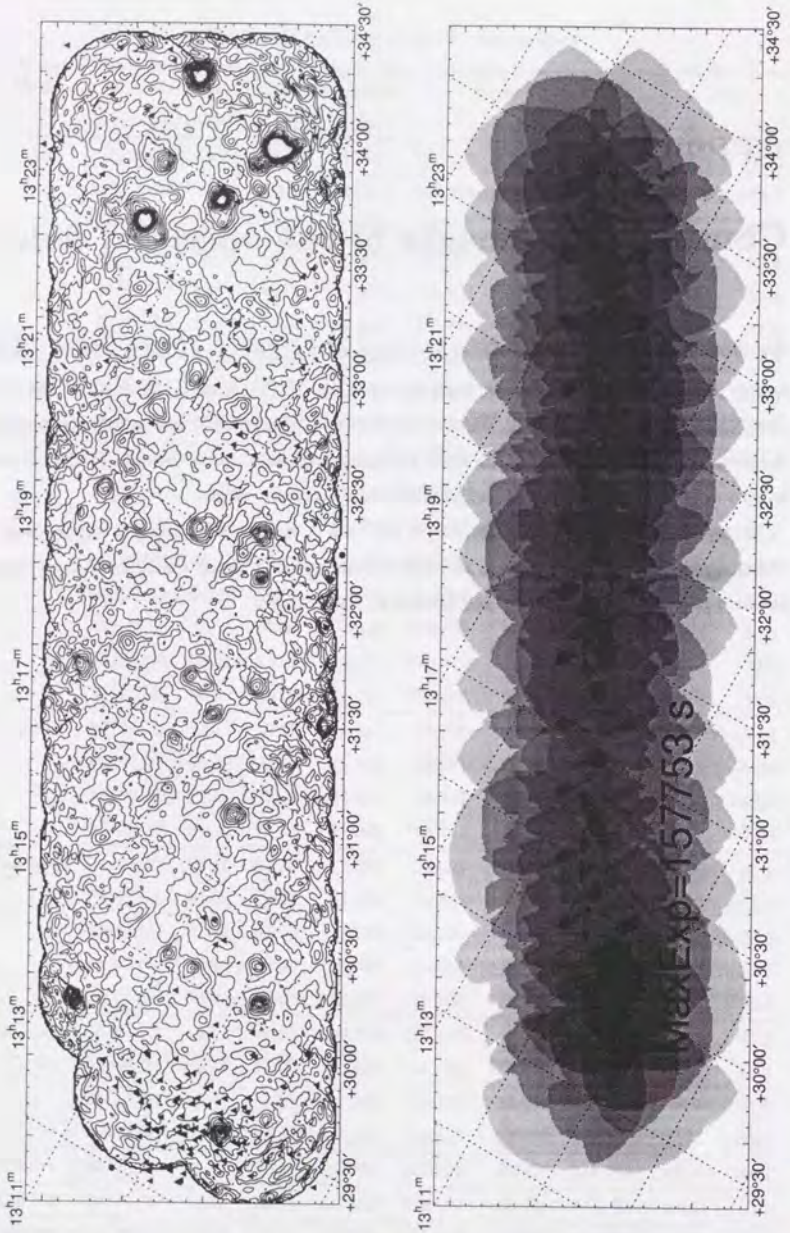

Figure B.1: LSS

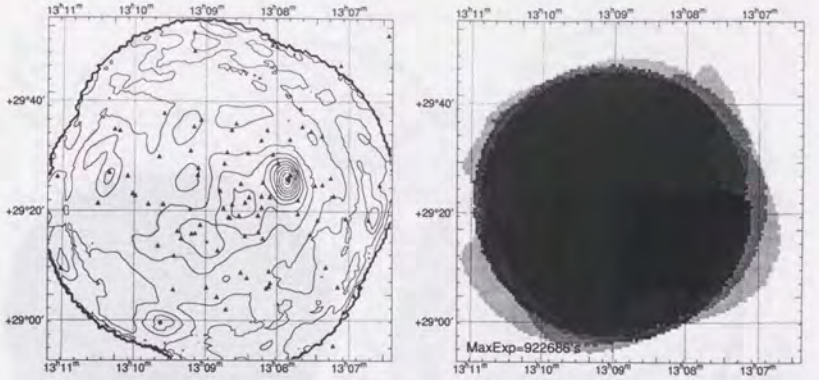

Figure B.2: SA57

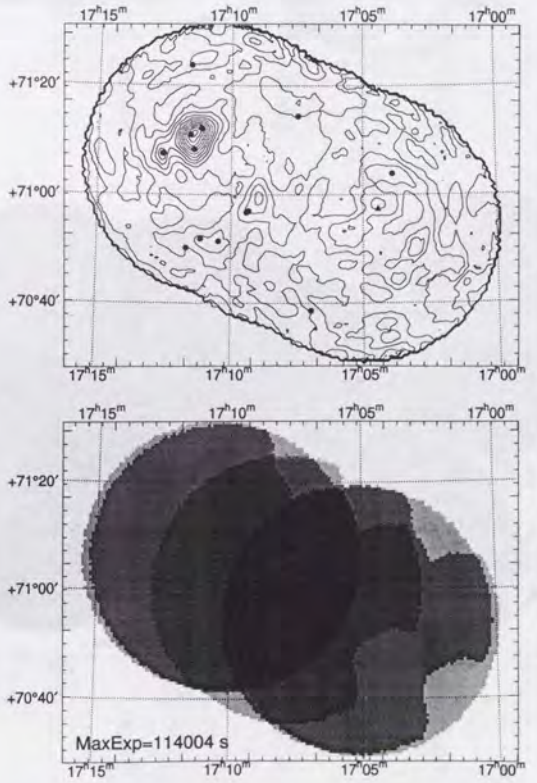

Figure B.3: Draco Field

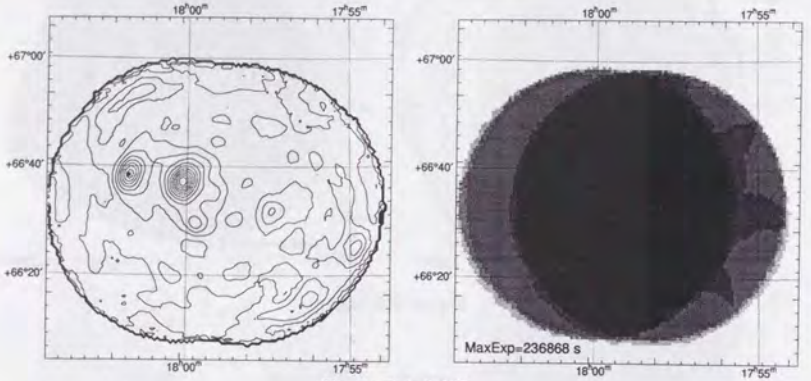

Figure B.4: NEP

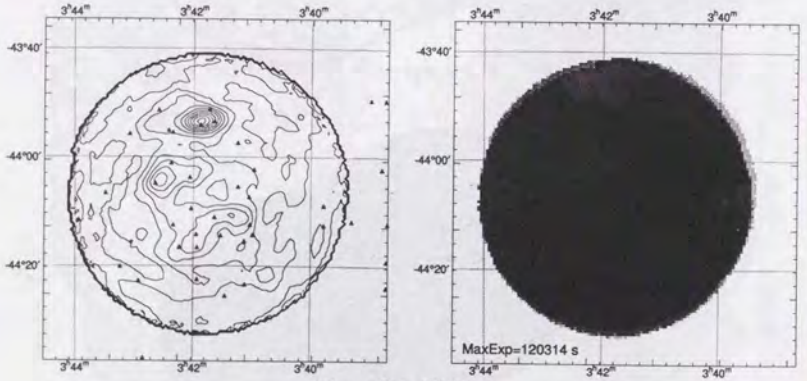

Figure B.5: QSF3

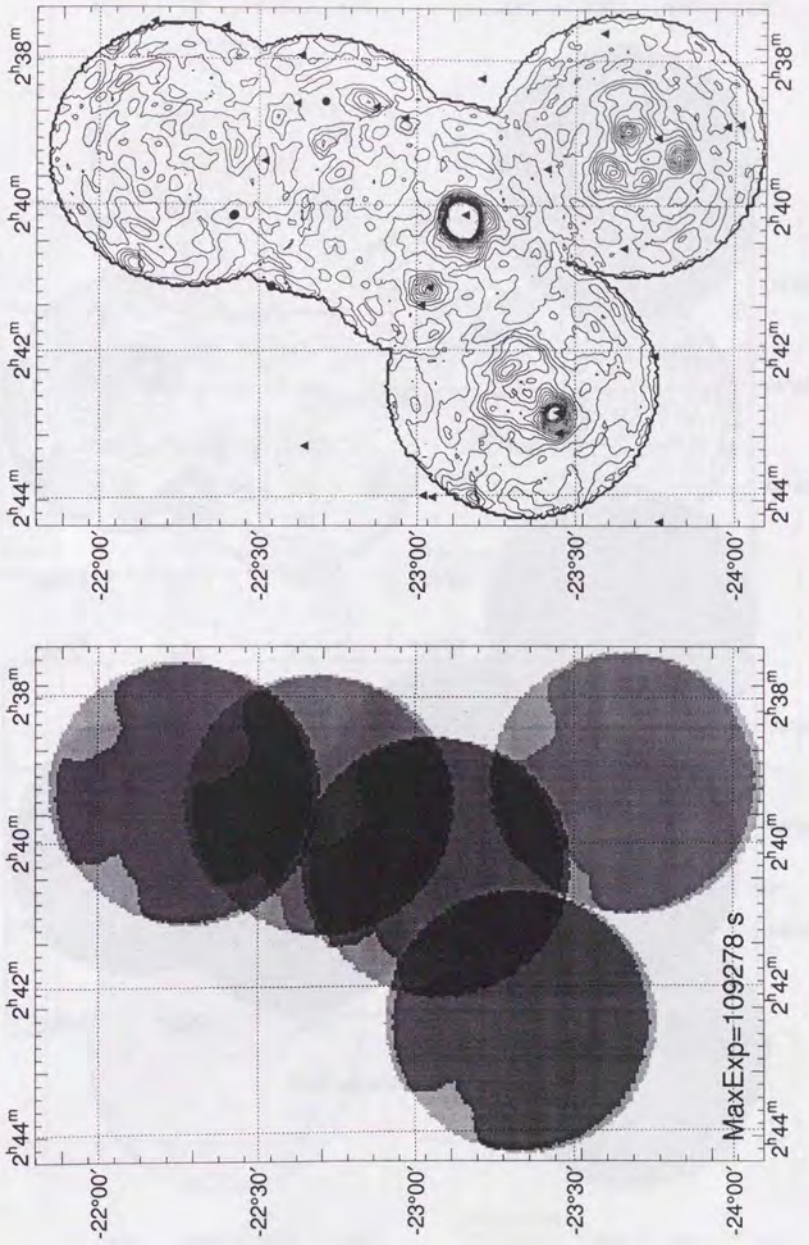

Figure B.6: z-system

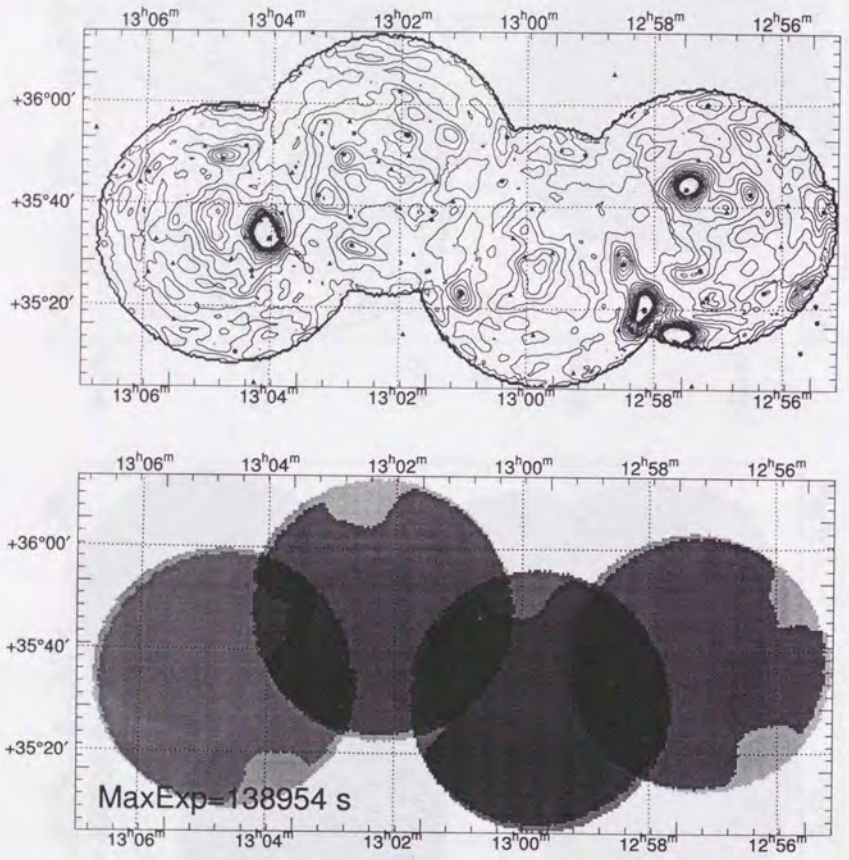

Figure B.7: Braccesi Field

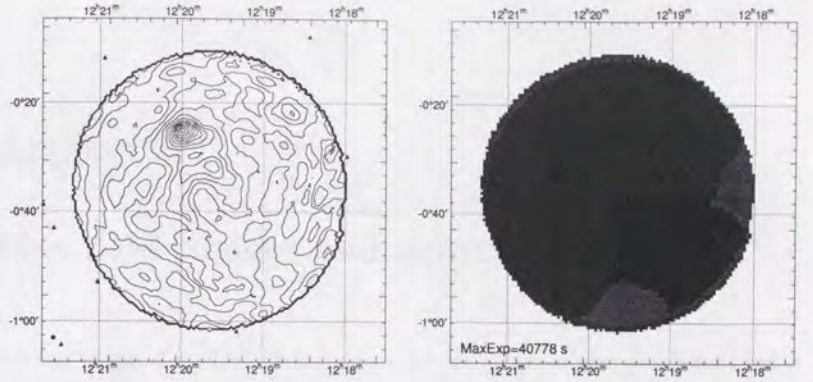

Figure B.8: Jupitar

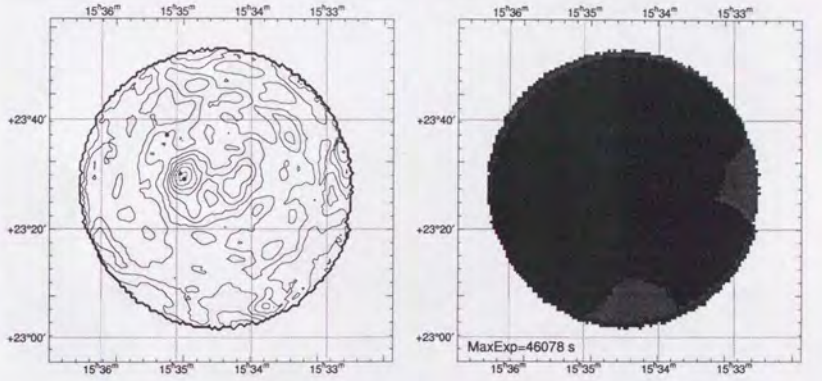

Figure B.9: Arp 220

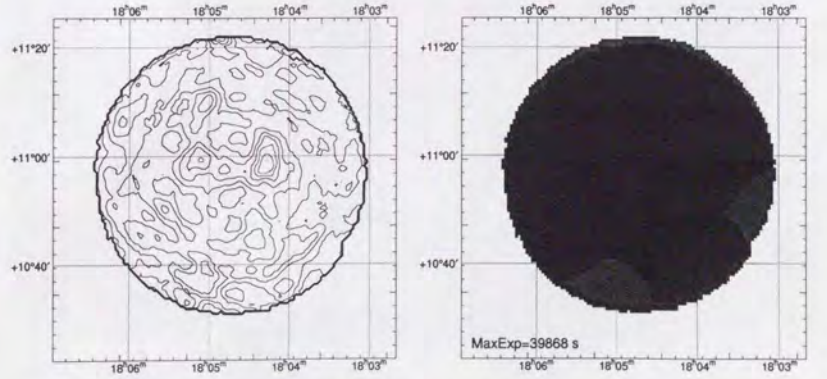

Figure B.10: 3C368

Appendix C

Flat field images and source-masks

Flat field images of the CXB observations, which are created by the method described in §7.2. The white pixel and black pixel represent −0.1 and 0.4, respectively. Source-masks at the threshold of 0.1 are also accompanied with.

Figure C.1: LSS

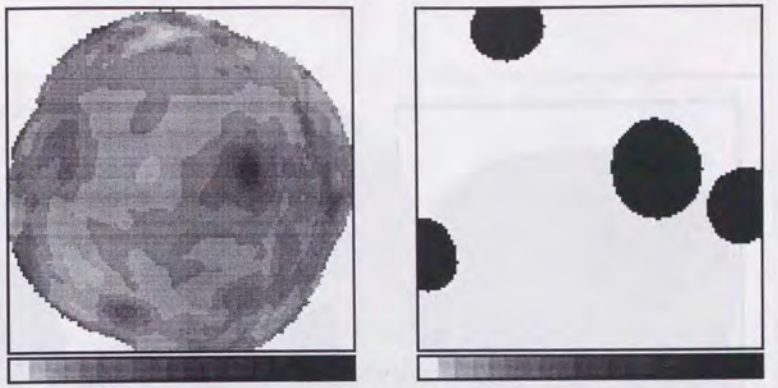

Figure C.2: SA57

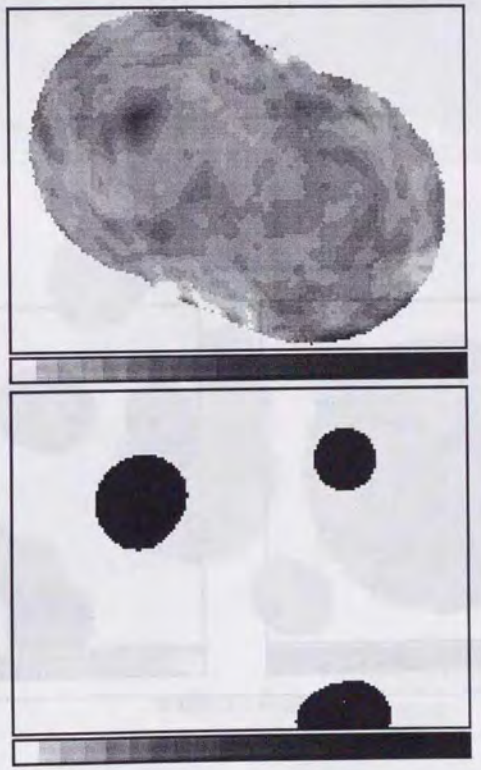

Figure C.3: Draco Field

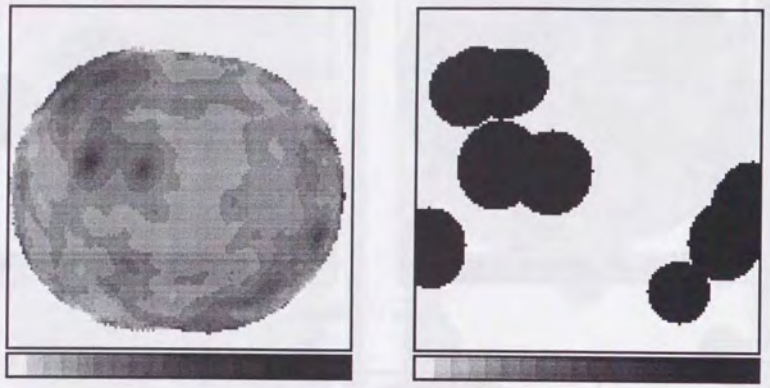

Figure C.4: NEP

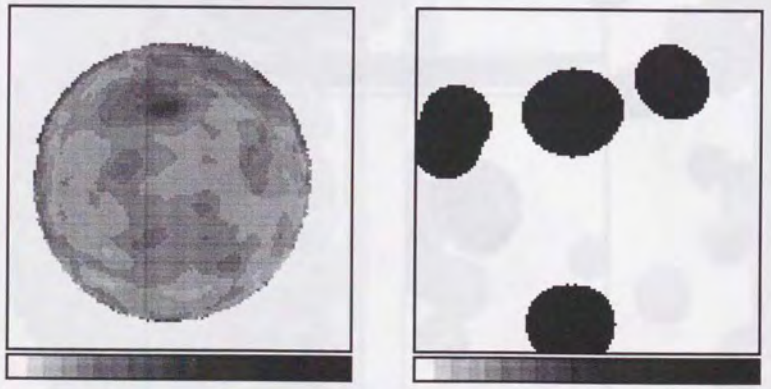

Figure C.5: QSF3

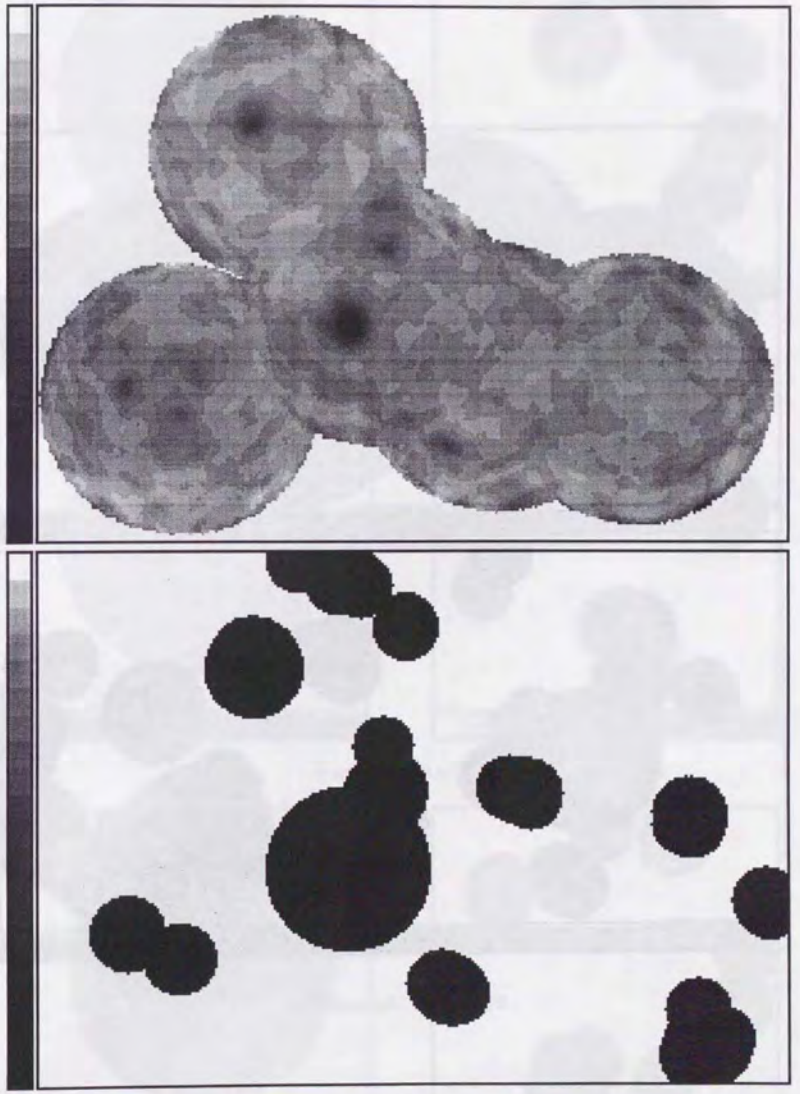

Figure C.6: z-system

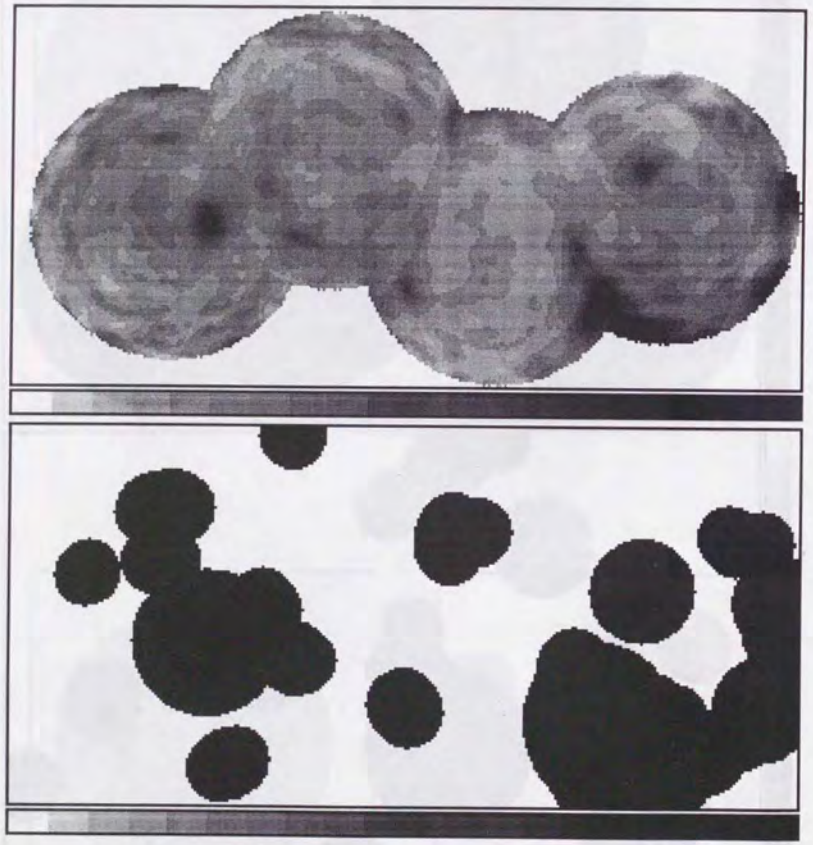

Figure C.7: Braccesi Field

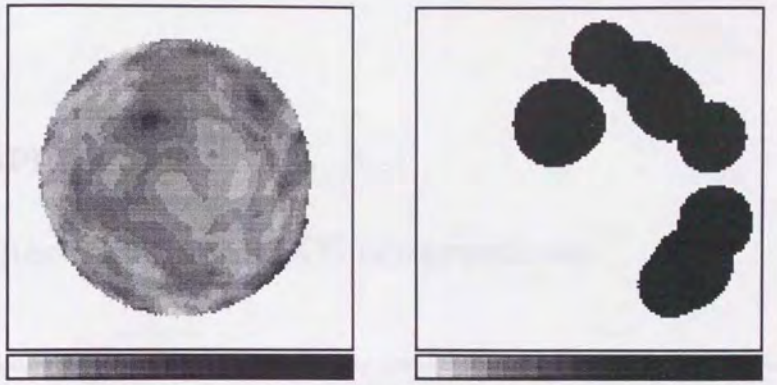

Figure C.8: Jupiter

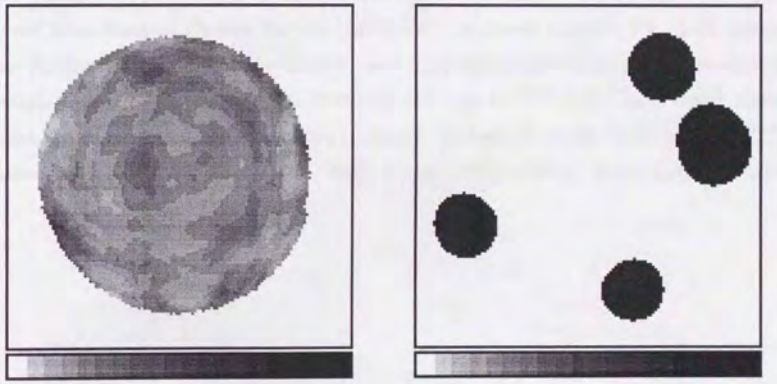

Figure C.9: Arp220

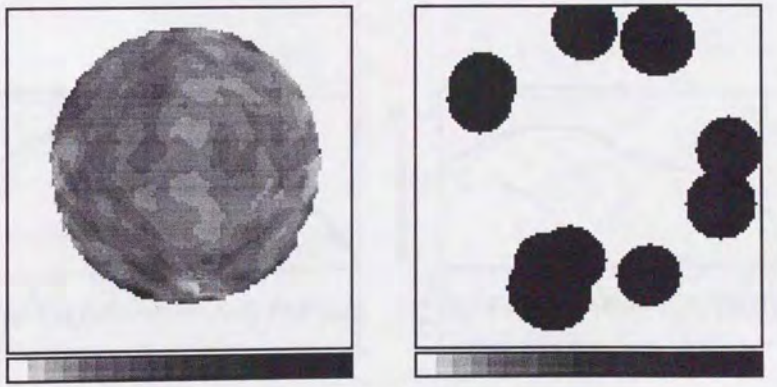

Figure C.10: 3C368

Appendix D

Spectra of the CXB observations

We show the spectra of the CXB observations fitted in the 0.6–10 keV energy band with an absorbed power-law ($PL^{\rm hard}$) plus a steep power-law model ($PL^{\rm soft}$), in figure D.1–D.13. Photon indices of $PL^{\rm soft}$ are fixed to 6.0. Absorption columns are also fixed to the values derived from Einstein On-line Service (*EINLINE*), as shown in table 7.1. Left figures show the spectra including point sources, and right figures shows the spectra processed through the source-maskings at the threshold of 0.1 on M^{FLAT} (ref. §7.2). Upper panel of each figure shows GIS2+3 spectrum (crosses), the best fit model (solid line), $PL^{\rm hard}$ (dashed line), and $PL^{\rm soft}$ (dot-dashed line). Lower panels show residuals plotted in unit of σ.

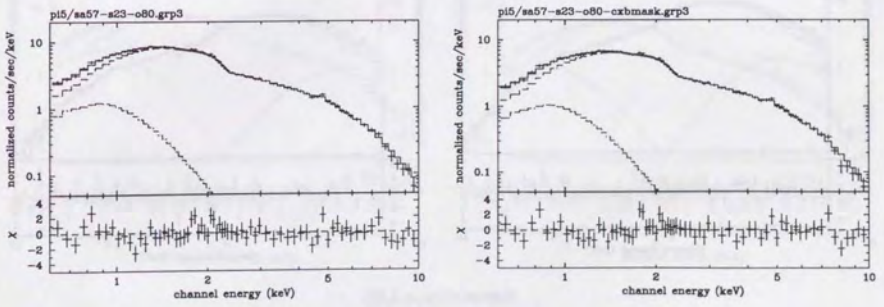

Figure D.1: SA57

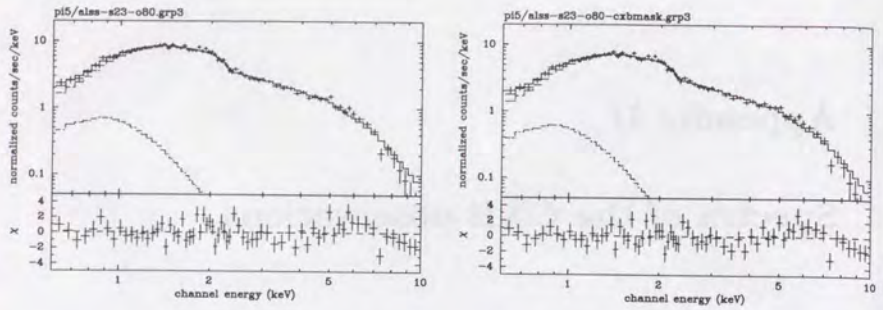

Figure D.2: a-LSS

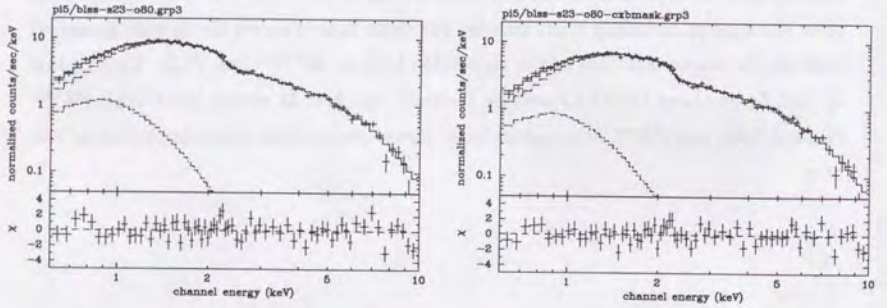

Figure D.3: b-LSS

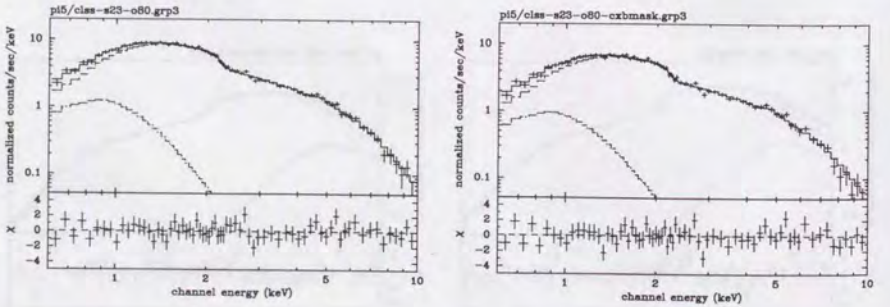

Figure D.4: c-LSS

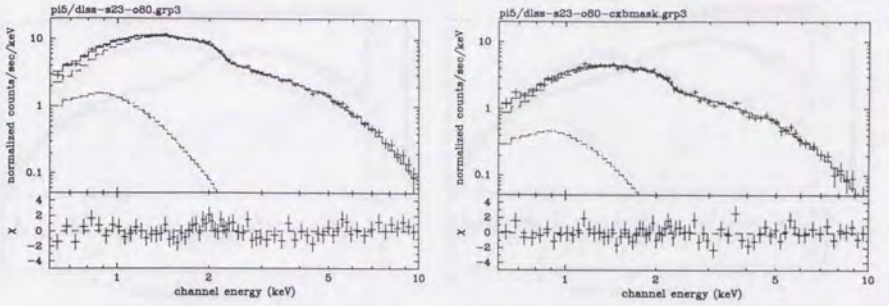

Figure D.5: d-LSS

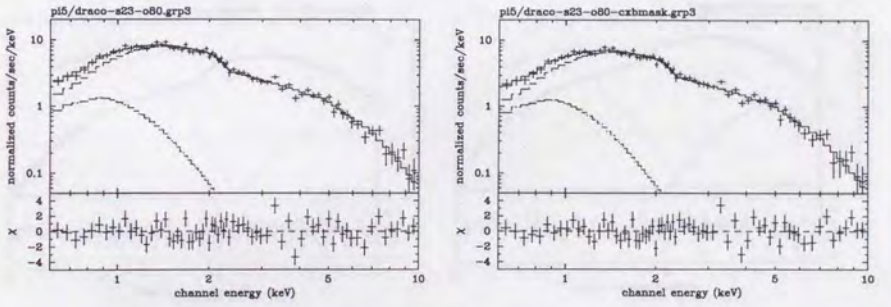

Figure D.6: Draco Field

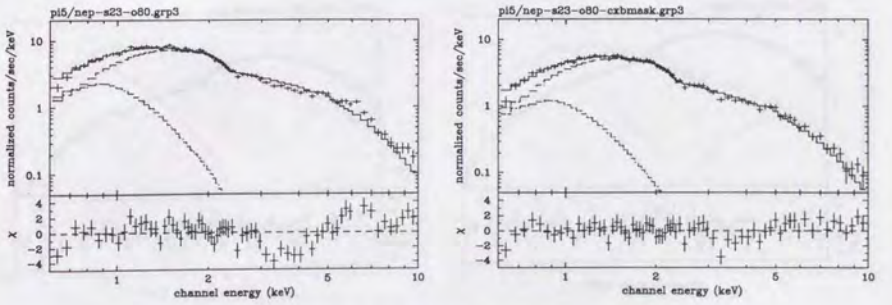

Figure D.7: NEP

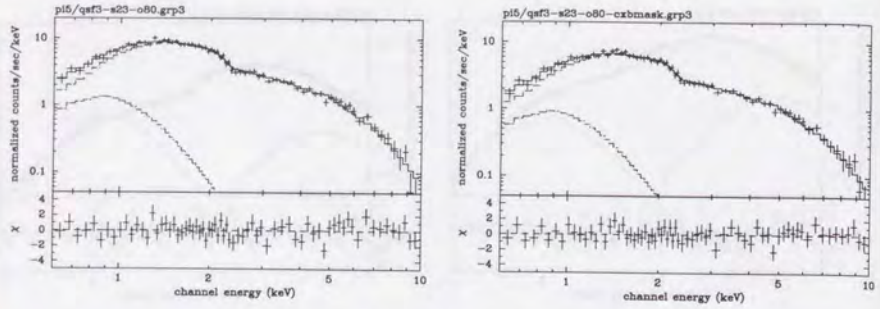

Figure D.8: QSF3

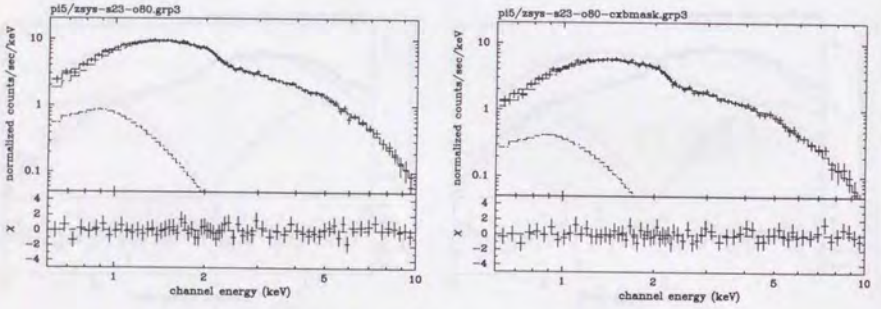

Figure D.9: z-system

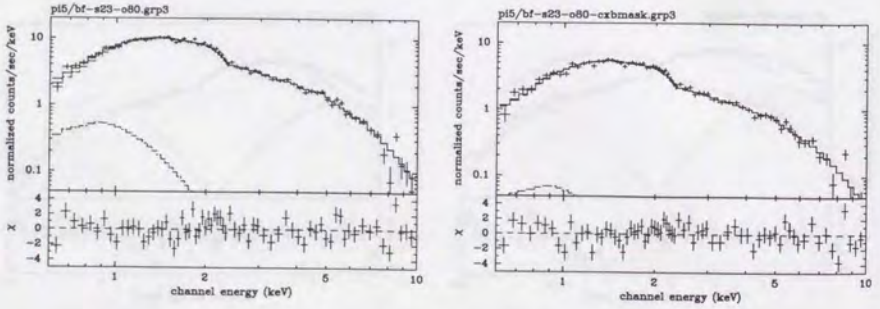

Figure D.10: Braccesi Field

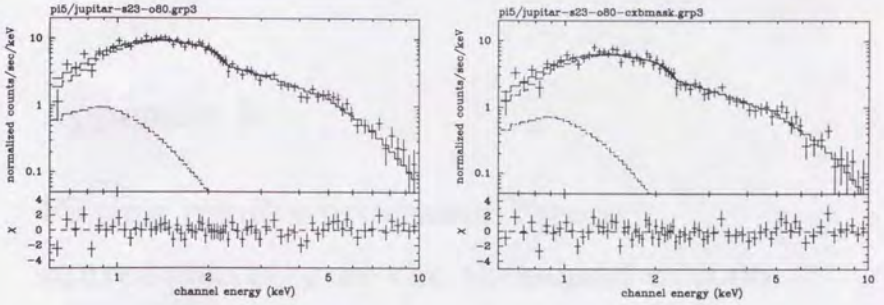

Figure D.11: Jupiter

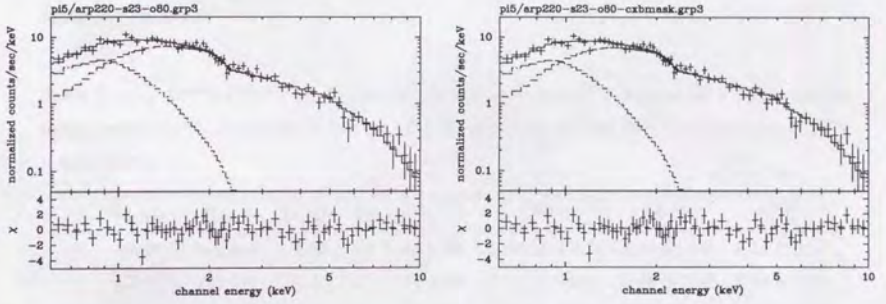

Figure D.12: Arp 220

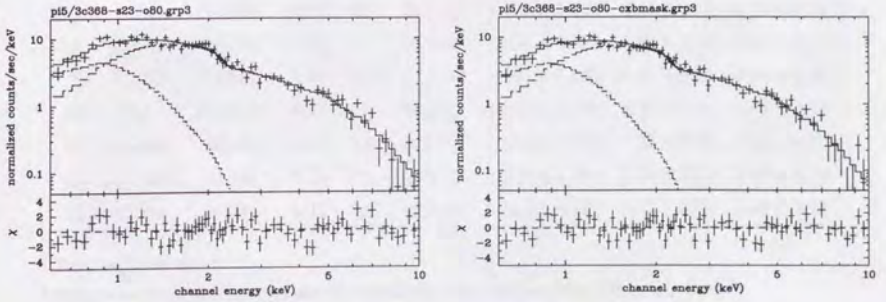

Figure D.13: 3C368

Appendix E

Fitting results processed through source-masking at the threshold of 0.06

In table E.1, we show the fitting results of each field when point sources are masked at the threshold of 0.06 on M^{FLAT}. The source-mask used for the fitting are shown in figure E.1–E.10.

Table E.1: ($PL^{\rm hard}$+$PL^{\rm soft}$) fits to the 0.6–10 keV spectrum of each field with point sources being masked at the threshold of 0.06 on M^{FLAT}. All errors are the 90% confidence level. $\Gamma^{\rm soft}$ is fixed to 6.0.

ID	Name	Exp.†	Area‡	$N_{\rm H}^{\sharp}$	χ^2/d.o.f	$\Gamma^{\rm hard}$	$F_{\rm X}^{\rm hard\triangleleft}$	$F_{\rm X}^{\rm soft\star}$
1	SA57	461,343	0.48	1.0	64.4/67	1.382 ± 0.020	5.69 ± 0.09	1.21 ± 0.15
2	a-LSS	119,221	1.31	1.1	87.4/67	1.471 ± 0.041	5.28 ± 0.18	0.59 ± 0.31
3	b-LSS	130,206	1.36	1.1	77.9/67	1.481 ± 0.041	5.37 ± 0.18	1.03 ± 0.33
4	c-LSS	138,641	1.47	1.1	68.7/67	1.498 ± 0.043	4.94 ± 0.18	1.07 ± 0.32
5	d-LSS	127,324	0.95	1.1	65.4/67	1.509 ± 0.054	5.21 ± 0.23	0.78 ± 0.42
6	Draco	57,002	0.55	4.1	77.4/67	1.489 ± 0.055	5.20 ± 0.24	1.60 ± 0.42
7	NEP	118,434	0.35	4.2	70.5/67	1.406 ± 0.043	5.41 ± 0.19	1.70 ± 0.31
8	QSF3	60,157	0.26	1.7	53.5/67	1.398 ± 0.055	6.20 ± 0.28	0.99 ± 0.46
9	ZSYS	109,893	0.89	2.3	35.2/67	1.501 ± 0.050	5.28 ± 0.22	0.68 ± 0.38
10	BF	114,738	0.55	1.2	88.2/67	1.548 ± 0.045	5.31 ± 0.22	0.02 ± 0.22
11	Jupiter	20,389	0.16	2.1	63.0/67	1.616 ± 0.117	4.55 ± 0.43	0.43 ± 0.66
12	Arp 220	23,039	0.22	4.2	49.4/67	1.410 ± 0.106	4.79 ± 0.41	3.97 ± 0.78
13	3C368	19,934	0.11	9.8	82.3/67	1.494 ± 0.141	5.07 ± 0.56	4.09 ± 1.11

† Total exposure time (s).

‡ Integration area (deg^2) on the sky after applying the source maskings (threshold 0.06).

♯ Absorption for $PL^{\rm hard}$ (10^{20} cm^{-2}) from Einstein On-line Service (*EINLINE*). Fixed while fitting.

◁ Flux of $PL^{\rm hard}$ (10^{-8} erg s^{-1} cm^{-2} str^{-1}) in the 2–10 keV energy band.

⋆ Flux of $PL^{\rm soft}$ (10^{-8} erg s^{-1} cm^{-2} str^{-1}) in the 0.5–2 keV energy band.

Figure E.1: LSS

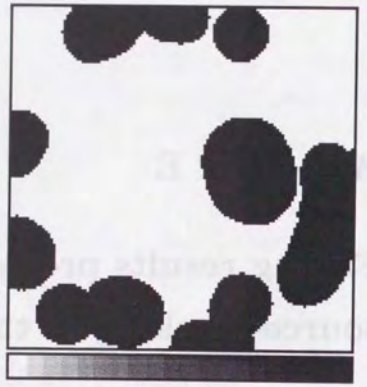

Figure E.2: SA57

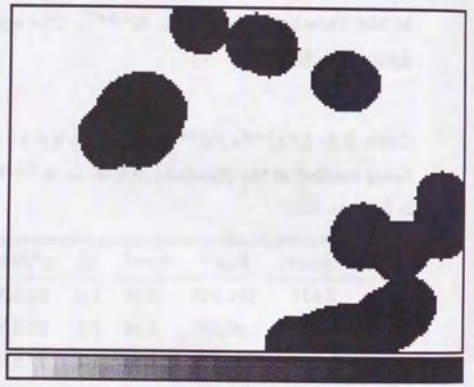

Figure E.3: Draco Field

Figure E.4: NEP

Figure E.5: QSF3

Figure E.6: z-system

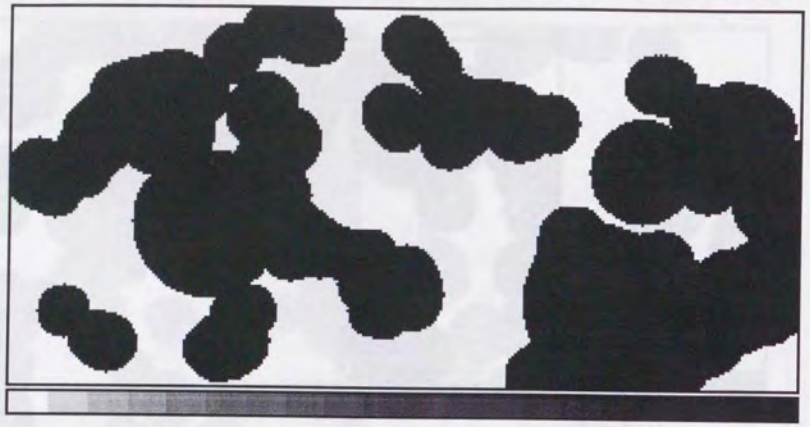

Figure E.7: Braccesi Field

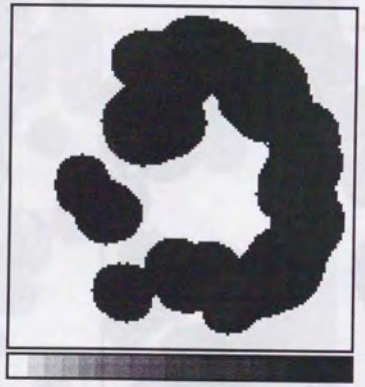

Figure E.8: Jupiter

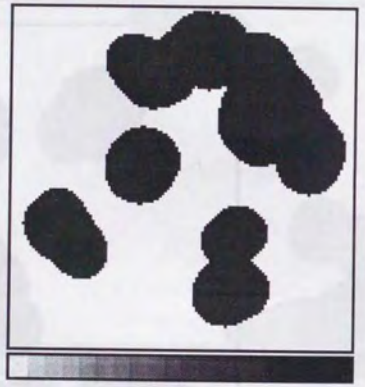

Figure E.9: Arp 220

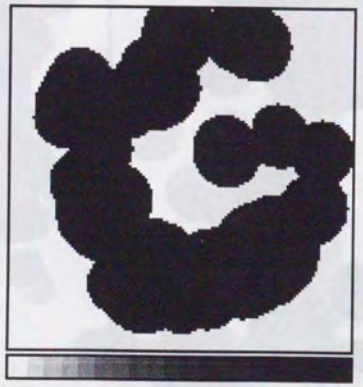

Figure E.10: 3C368

Appendix F

Hardness-map images of the observed fields

We show the hardness-map gray-scale images $M^{H/S}(SKYX, SKYY)$ in figure F.1–F.10. Black and white pixels correspond to 0.5 and 2.0, respectively. This $M^{H/S}$ has been created by calculating

$$M^{H/S}(SKYX, SKYY) = \frac{M^{FLAT}_{2-7\,\mathrm{keV}}(SKYX, SKYY) + 0.5}{M^{FLAT}_{0.7-2\,\mathrm{keV}}(SKYX, SKYY) + 0.5}, \tag{F.1}$$

where $M^{FLAT}_{2-7\,keV}$ and $M^{FLAT}_{0.7-2\,keV}$ represent the flat-field images in the 2–7 keV and 0.7–2 keV energy bands, respectively, as described in §7.2.1. The offset terms of 0.5 are chosen rather optionally to avoid dividing 0.0 by 0.0. Therefore, pixel values of $M^{H/S}$ are not necessarily proportional to the real hardness, we can see at least whether bright sources are flatter (harder) or steeper (softer) than the average CXB.

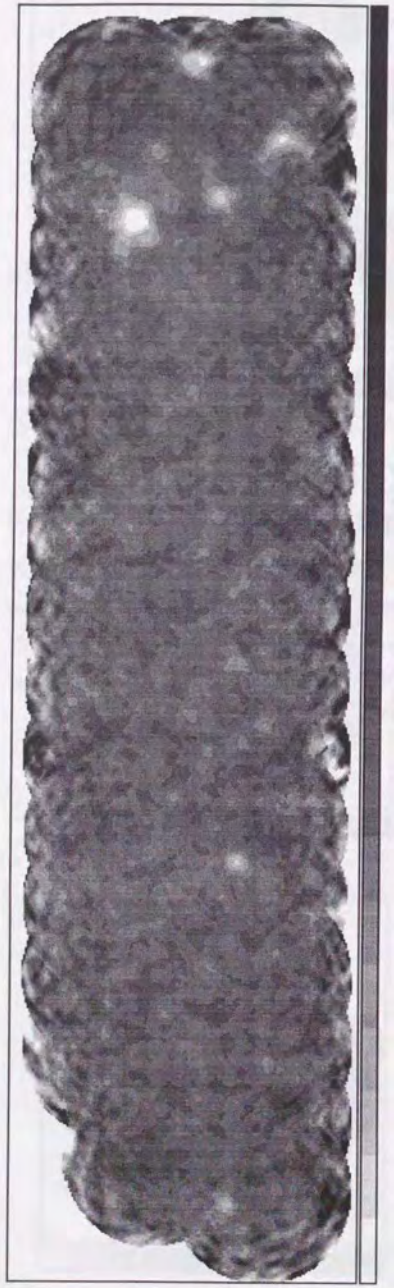

Figure F.1: LSS

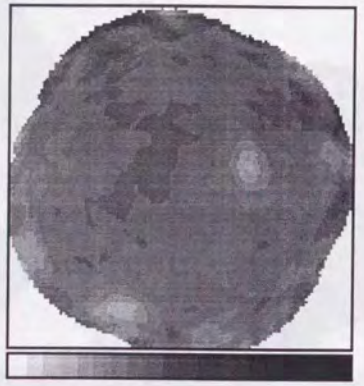

Figure F.2: SA57

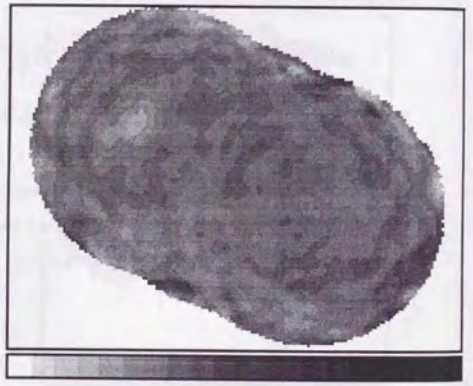

Figure F.3: Draco Field

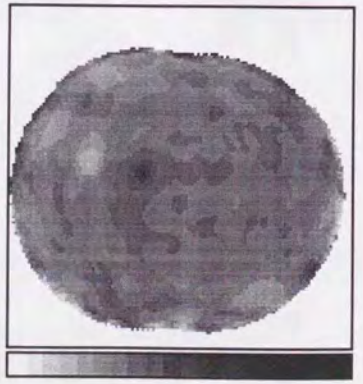

Figure F.4: NEP

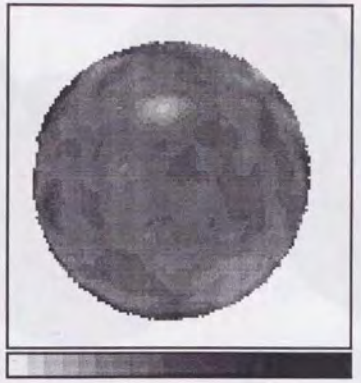

Figure F.5: QSF3

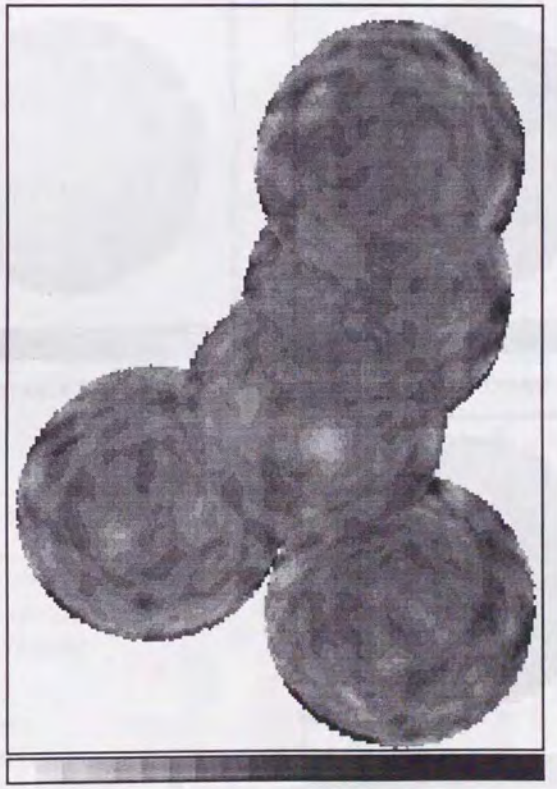

Figure F.6: z-system

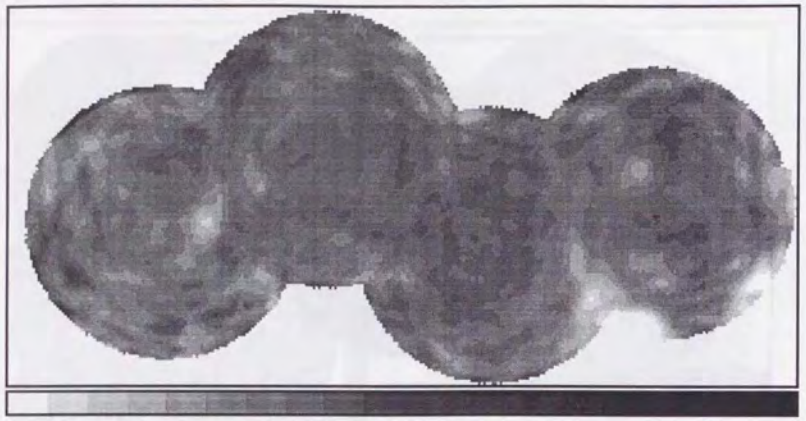

Figure F.7: Braccesi Field

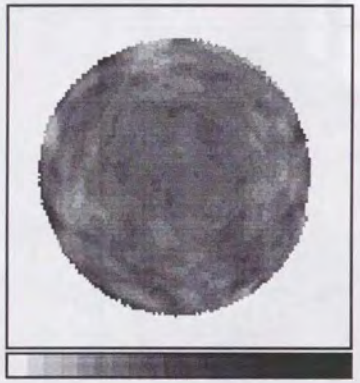

Figure F.8: Jupiter

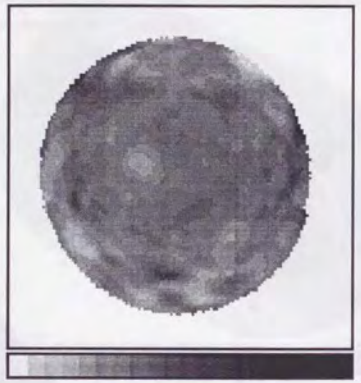

Figure F.9: Arp 220

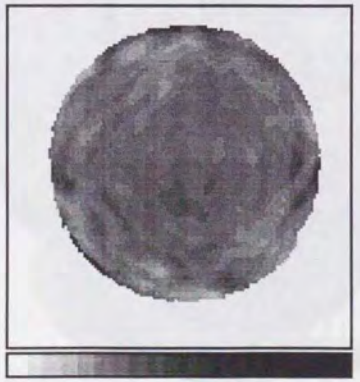

Figure F.10: 3C368

Appendix G

All-sky maps of the X-ray observations

We show all-sky maps of the previous X-ray observations in figure G.2–G.5, as well as the hydrogen column map in figure G.1. All maps are shown in the Galactic coordinate centered on the $l = 0°$, and increasing to the left. Table G.1 is the summary of the X-ray images.

Table G.1: Summary of the X-ray images in this chapter

Instrument	Energy Band	Resolution	Figure
HEAO-1 A2	2–60 keV	$3° \times 3°$	G.2
ROSAT PSPC	1/4 keV	2°	G.3a
	3/4 keV	2°	G.3b
	1.5 keV	2°	G.3c
Wisconsin survey	C-band ($\sim$ 0.16–0.284 keV)	7°	G.5a
(proportional counter)	M-band ($\sim$ 0.49–$\sim$ 1.09 keV)	7°	G.5a

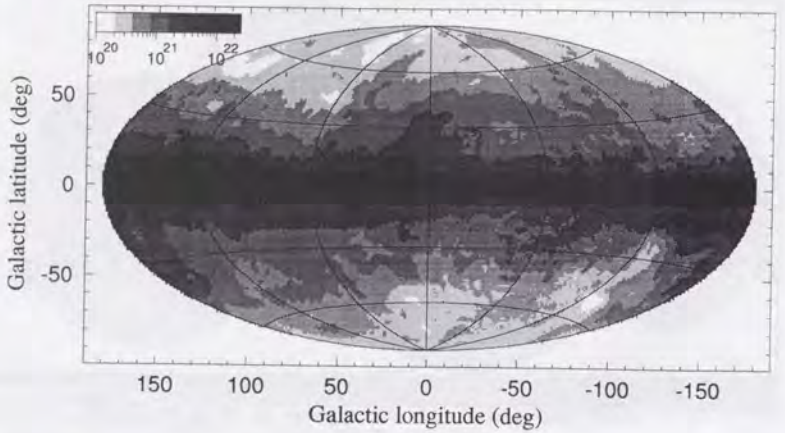

Figure G.1: Map of the total number of hydrogen atoms in different directions on the sky, adopted from the NRAO Radio CD-ROM. Seven different 21 cm HI surveys are combined, and averaged over 1 square degree intervals. Most of the arcs and circular structures outline huge regions created by supernova explosions (Dickey, and Lockman 1990).

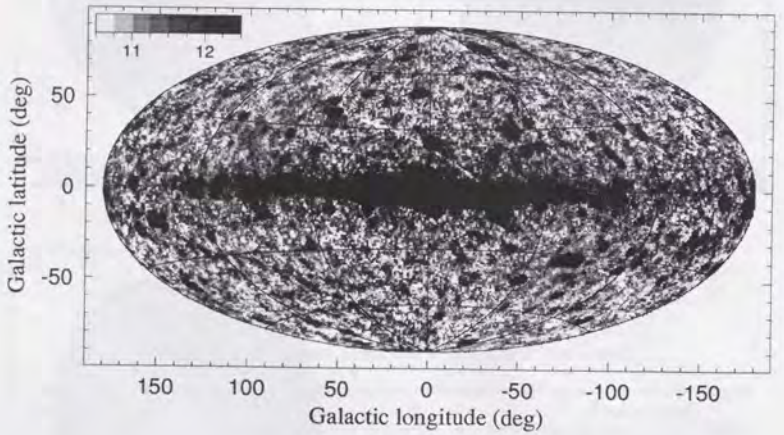

Figure G.2: The X-ray sky from HEAO-1 A2 in Galactic coordinates at 3° resolution, adopted from the WWW service of NASA/GSFC at *http://heasarc.gsfc.nasa.gov*. Bright sources and diffuse emission from the Galaxy dominate at low Galactic latitudes. Besides it, X-ray sky is dominated by the CXB, and fluctuations in the CXB are seen in at high Galactic latitude (Allen, Jahoda, and Whitlock in article Vol. 5 of Legacy, journal of the HEASARC).

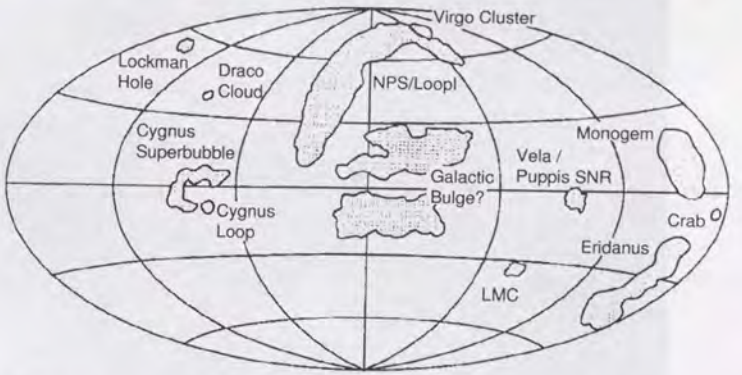

Figure G.4: Brief descriptions of the main features seen in figure G.3, adopted from the same paper.

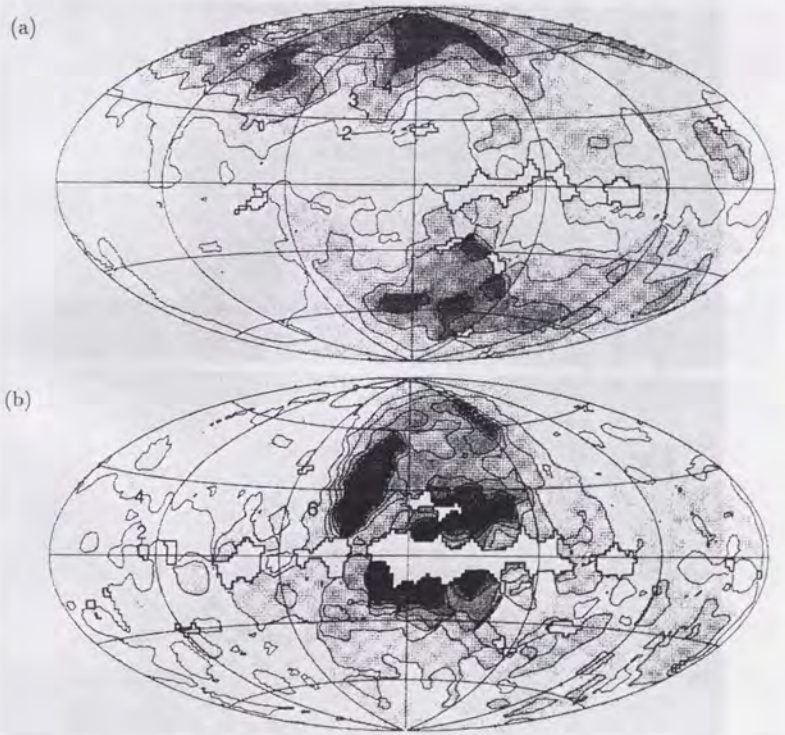

Figure G.5: (a) C-band (~ 160–284 eV) and (b) M-band (~ 490–~ 1090 eV) maps from the Wisconsin sky survey (McCammon et al. 1983), adopted from the review by McCammon & Sanders (1990).

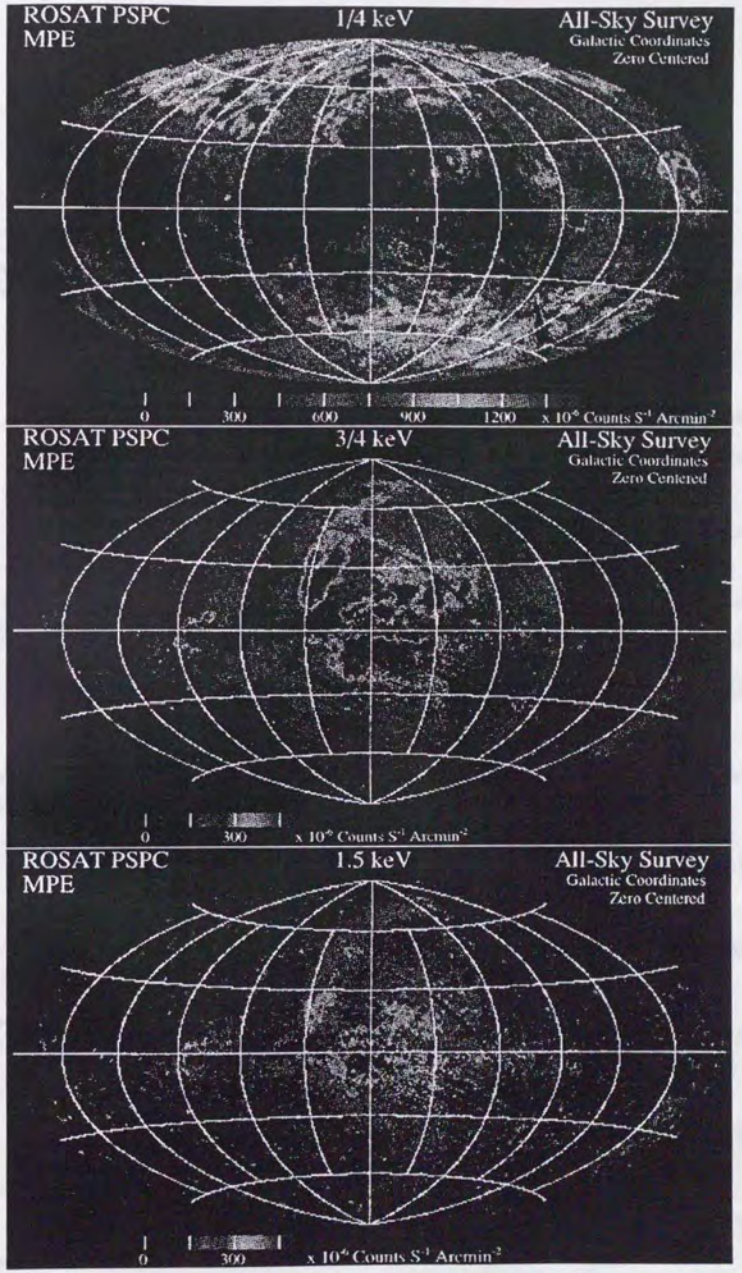

Figure G.3: ROSAT PSPC all sky survey X-ray intensity Galactic coordinates map in (a) 0.25 keV, (b) 0.75 keV, and (c) 1.50 keV energy band, adopted from Snowden et al. (1995).

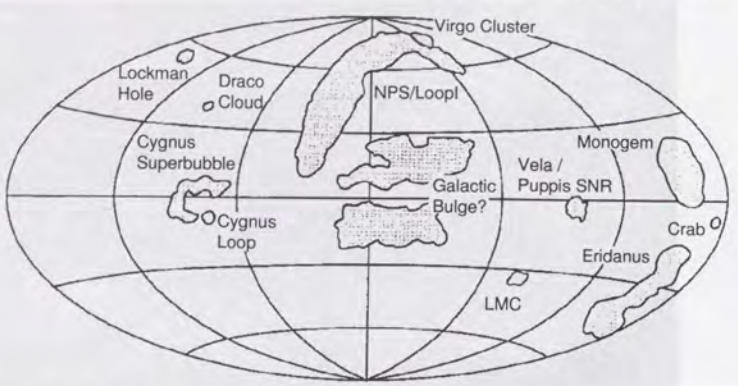

Figure G.4: Brief descriptions of the main features seen in figure G.3, adopted from the same paper.

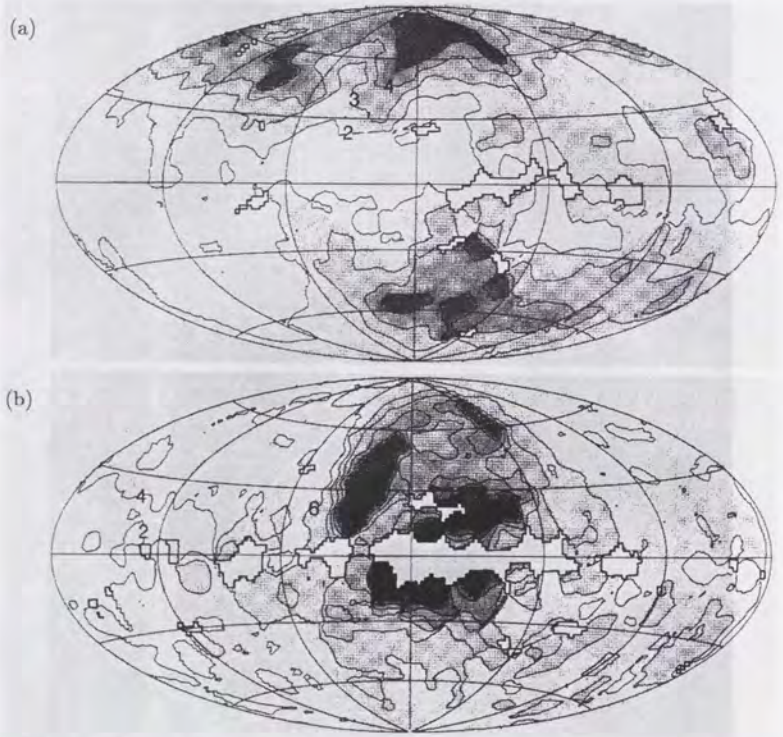

Figure G.5: (a) C-band (~ 160–284 eV) and (b) M-band (~ 490–~ 1090 eV) maps from the Wisconsin sky survey (McCammon et al. 1983), adopted from the review by McCammon & Sanders (1990).

Appendix H

CXB fluctuation due to unresolved sources

H.1 Formulation of the CXB fluctuation

As describeded in §2.2, the CXB intensity observed with an instument with a finite f.o.v. fluctuates from field to field, since the number of discrete sources in the f.o.v. statistically fluctuates. Condon (1974) estimated this fluctuation level, and we below introduce her results briefly.

Let $n(S)$ denote the differential source number density with the flux S (erg cm^{-2} s^{-1}). This $n(S)$ represents the $\log N$-$\log S$ relation described in §2.2 and usually expressed by

$$n(S) = k\, S^{-\gamma} \quad (\gamma = 2.5 \ \text{ for the Euclidian universe}). \tag{H.1}$$

We next define the transmission function $f(\theta, \phi)$ for the detector, which relates the observed counting rate x (c s^{-1} cm^{-2}) for the detector to the flux S from the source locating at $\Omega = (\theta, \phi)$ on the sky as:

$$x = A\, f(\Omega)\, S, \tag{H.2}$$

where A is a constant which normalizes $f(\theta, \phi)$ to be 1.0 at the peak, i.e., $f(0, 0) = 1$. Then, the expectation $d\overline{n}(x)$ of the source number with the counting rate in the range $x \sim x + dx$ can be estimated as

$$d\overline{n}(x)\, d\Omega = n(S)\, dS\, d\Omega = n\left(\frac{x}{A\, f(\Omega)}\right) \frac{dx}{A\, f(\Omega)}\, d\Omega, \tag{H.3}$$

since $dx = A\, f(\Omega)\, d\Omega$. Assuming equation (H.1), we derive

$$d\overline{n}(x) = k\, A^{\gamma-1}\, x^{-\gamma}\, \Omega_e\, dx, \tag{H.4}$$

where

$$\Omega_e \equiv \int [\, f(\Omega)\,]^{\gamma-1} d\Omega. \tag{H.5}$$

This Ω_e is called "effective beam size" and represents the response of the detector to the source confusion.

Utilizing equation (H.4), we can calculate the expectation $\overline{D}$ of the observed counting rate D (c s^{-1} cm^{-2}) as:

$$\overline{D} = \int_{D_0}^{\infty} x\, d\overline{n} = k\, A^{\gamma-1}\, \Omega_e \int_{D_0}^{\infty} x^{-\gamma+1} dx = \frac{k\, A^{\gamma-1}\, \Omega_e}{2-\gamma}\, D_0^{2-\gamma}, \tag{H.6}$$

where D_0 is a lower cut-off of x, which is introduced to avoid the divergence of the integral. Physically, this means that the log N-log S relation should flatten below some flux. Since dn should be subject to the Poisson distribution, i.e., $\delta(dn)^2 = d\overline{n}$, we can also calculate the standard deviation σ_D of the observed conting rate D as:

$$\sigma_D^2 = \int_0^{D_c} \frac{[\, x\, \delta(dn)\,]^2}{dx}\, dx = \int_0^{D_c} x^2\, d\overline{n} = \frac{kA^{\gamma-1}\Omega_e}{3-\gamma}\, D_c^{3-\gamma}, \tag{H.7}$$

where D_c is an upper cut-off of x, i.e. we discard the data brighter than D_c regarding not a blank sky. Therefore, the fraction of the CXB fluctuation is

$$\sigma_D/\overline{D} = \frac{(k\, A^{\gamma-1}\, \Omega_e\, D_c^{3-\gamma})^{1/2}\, (2-\gamma)}{(3-\gamma)^{1/2}\, k\, A^{\gamma-1}\, \Omega_e\, D_0^{2-\gamma}} = \frac{2-\gamma}{\sqrt{(3-\gamma)\, k\, \Omega_e}} \left(\frac{D_c}{A}\right)^{(3-\gamma)/2} \left(\frac{D_0}{A}\right)^{\gamma-2}. \tag{H.8}$$

for the Euclidian universe, i.e., $\gamma = 2.5$, this becomes

$$\sigma_D/\overline{D} \propto \Omega_e^{-0.5}\, S_c^{0.25} \quad (S_c \equiv D_c/A). \tag{H.9}$$

H.2 Effective beam size for the XRT+GIS

Taking into account both vignetting and stray-light effects, we calculate Ω_e for the XRT+GIS when we use inside 20 mm from the optical axis as the data integration region.

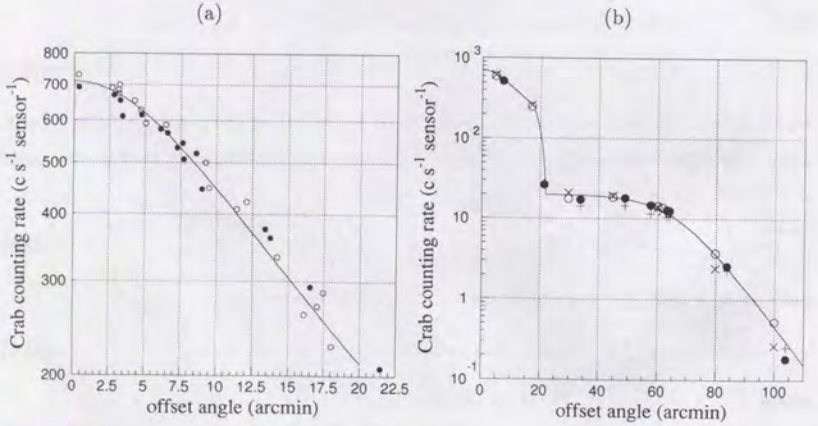

Figure H.1: (a) The observed Crab counting rate in the 0.7–10 keV energy band plotted against the offset angle from the XRT optical axis. Filled circles represent GIS2 and open circles GIS3. (b) Same as upper panel of figure 4.17a. Solid line represents equation (H.10).

Figure H.1 shows the dependence of the Crab counting rate on the offset angle θ from the XRT optical axis. As seen in the figure, we approximate the counting rate as:

$$f(\theta) = \begin{cases} \dfrac{710}{1+(x/13)^2} & \cdots\ (\theta < 18') \\ -51.6\,(\theta - 22) + 20 & \cdots\ (18' \le \theta < 22') \\ \dfrac{20}{1+0.5\,\exp[(\theta-60)/9]} & \cdots\ (22' \le \theta) \end{cases}. \tag{H.10}$$

If we ignore the azimuth angle dependence, we can calculate Ω_e as:

$$\Omega_e = 2\pi \int_0^{\infty} [\, f(\theta)/f(0)\,]^{\gamma-1} \sin\theta\, d\theta. \tag{H.11}$$

In figure H.2, we show

$$\Omega_e(\theta_c) = 2\pi \int_0^{\theta_c} [\, f(\theta)/f(0)\,]^{1.5} \sin\theta\, d\theta. \tag{H.12}$$

Therefore, Ω_e for the XRT+GIS is 0.142 deg^2. Contribution of the stray light to Ω_e is ~ 0.01 deg^2 and almost negligible.

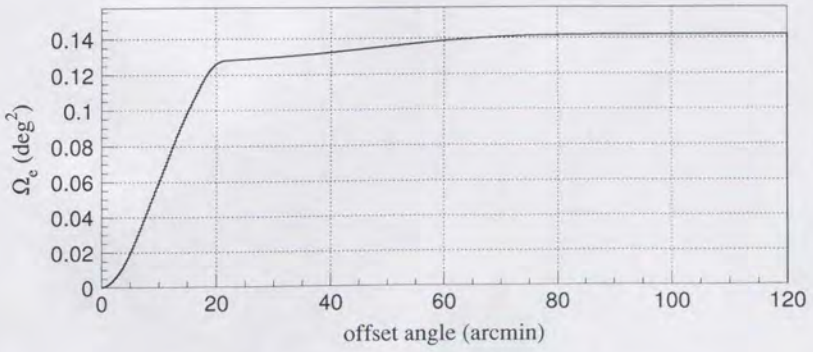

Figure H.2: Calculation of Ω_e for the XRT+GIS.

of the Cosmic X-ray Background from ASCA Observations